Analysis of the Cloud Observations by Radar and Lidar

岩崎，杉紀

博士論文

Analysis of the Cloud Observations
by
Radar and Lidar

（レーダ、ライダによる雲の観測・解析）

Suginori Iwasaki

The Graduate School of Science and Technology,
Kobe University, Nada, Kobe 657-8501, Japan

Contents

Chapter 1

General introduction

This thesis is dedicated to understand the micro-physical properties of the cloud particles by using active sensors, such as lidar, 95GHz cloud radar and 13.8GHz precipitation radar. Such knowledges are important to increase the potential of General Circulation Models (GCM) and leads to accelerate the reliability for the forecast of future climate changes. That is, it is widely recognized that the vertical distribution of the cloud particles and their interaction with aerosols remain as key problems. This is because it is impossible to derive such kind of micro-physics by using passive sensors on satellite, where these sensors measure integrated values. Only active sensors can provide such informations. This is the fundamental advantages of active sensors.

Lidar (light detection and ranging) is one of the most suitable active sensors to observe cloud and aerosol particles. It measures the distance between scatters and a lidar system, and backscattered power by scatters. Our lidar system can also measure cross-polarization. It is well known that the ice cloud particles, that often exist at the altitude of around 10km, are non-spherical. However, it is very difficult to calculate scattering signals, *e.g.*, backscattering coefficient, for such irregularly shaped particles obtained by the lidar observation (see chapter **2**). In this thesis, we develop a new scattering method that is possible to retrieve the backscattering coefficient from the lidar observation.

The conventional centimeter wavelengths radars (radio detecting and ranging) do not have sensitivity to detect cloud particles. Because those wavelengths are much longer than cloud particles, generally less than 100 μm, the radar echo from these particles are less than the detection limit. This is the main reason why we need millimeter wavelengths radars. From the technical point of view, since their frequency is very high, *i.e.*, 95GHz, W-band, it is very difficult to develop cloud radars. Therefore only few countries, such as U.S., U.K., Germany and Japan have cloud radars. In Japan, only Communications Research Laboratory (CRL) succeeded in development of the cloud radar called SPIDER (Special Polarimetric Ice Detection and Explication Radar) in 1998 [1]. SPIDER can mea-

3

sure co- and cross-polarized backscattered radiance by log detector and Doppler velocity by IQ detector. Moreover, it is designed to be able to perform an air-borne observation. Consequently, it becomes possible to instantly observe clouds at large area (~ 100 km).

Received power by radar and lidar depends on the several micro-physical properties of scatters, *i.e.*, size, number concentration, shape and alignment of cloud particles. However, there have been only few synergy experiments by using these instruments [2-5].

This thesis consists of six chapters, where the following papers are cited,

- S. Iwasaki, and H. Okamoto, Anomalous backscattering enhancement by non-spherical ice crystals for lidar observation., Appl. Opt, 2000., submitted.

- S. Iwasaki, and H. Okamoto, Analysis of lidar backscattering enhancement for pristine hexagonal ice crystals., In Singh, Itabe, Sugimoto (Eds) SPIE2000: Remote Sensing of the Atmosphere, Environment, and Space., 2000., in press.

- S. Iwasaki, and H. Okamoto, Analysis of lidar returns from rectangles and hexagonal ice crystals., In Smith and Timofeyev (Eds.) IRS2000: Current Problems in Atmospheric Radiation, Deepak Publishing, 2000., in press.

In chapter **2**, we examine the lidar backscattering by large non-spherical ice crystals on the basis of ray optics [6]. Our numerical computations show when large ice particles have flat surfaces and distance Z between the particles and a receiver is less than $1km$, an anomalous backscattering enhancement can be expected compared with spherical case, in the lidar observations.

In chapter **3**, we analyze lidar backscattering enhancement for pristine hexagonal ice crystals by using Fraunhofer diffraction based on Kirchhoff's diffraction theory [7]. Those numerical computations show that received power at the altitude Z in the lidar equation is proportional to $Z^{-\alpha}$, where α is a function of Z, size and shape of particles and is not necessary to be 2, which is the slope of sphere. Our calculations suggest that hexagonal ice crystals, whose mode radiuses are more than several tens micrometers and those are perfectly oriented in horizontal plane, have anomalous backscattering enhancement compared with a sphere at even high altitude. This might explain the phenomena reported by Platt *et. al.* (1978) [8].

The chapter **4** is the extension of chapter **3**, where we calculate wide range of sizes of particles. We show that the received power for the hexagonal plates perfectly oriented in horizontal plane produces $10^4 \sim 10^9$ times larger signals compared with that for spheres with same size distribution at the altitude 10 km. And that for the hexagonal columns perfectly oriented in horizontal plane produces $5 \times 10^2 \sim 3 \times 10^4$ times larger signals compared with that for spheres at $Z = 10$ km.

In chapter **5**, we report synergy cloud observations by lidar, SPIDER and 13.8GHz precipitation radar, which is called CAMPR (CRL Airborne Multiparameter Precipitation Radar) [9]. Lidar and SPIDER are used to study micro-physics of cloud particles of cirrus. SPIDER and CAMPR are used to observe the cloud with melting layer [10, 11]. Melting layers have very strong radar echo for CAMPR, that has been known as bright band, while, those are weak for SPIDER. This should be the reflection of complex nature of cloud micro-physics, *e.g.* the dielectric constants for mixture of ice and water size of melting layer particles, etc. Thus these combination seems to be a powerful tool for the study of cloud with precipitation.

In chapter **6**, we report cloud observations by SPIDER onboard air craft above the Japan sea on February 28th, 2000. The main aim of this study is to design future space borne cloud radar, *e.g.* EarthCare Mission. We derive the sea surface reflectance. Our experiments show that sea surface can be used as a target to calibrate the space-borne cloud radar.

Next year, we are going to join Asian Atmospheric Particulate Environmental Change Experiment (APEX), and have ship-borne observations by using "Mirai vessel".

For space borne mission projects, Pathfinder Instruments for Cloud and Aerosol Space-borne Observations (PICASSO, lidar) [12] and CloudSat (95GHz cloud radar) in United States have been already approved. And EarthCare Mission (ECM, lidar and 95GHz cloud radar) in Europe and Japan, ATMOS-B1 (lidar and 95GHz cloud radar) in Japan are proposed [13]. We hope the studies in this thesis contribute for these future experiments.

Acknowledgement:

Bibliography

[1] H. Horie, T. Iguchi, H. Hanado, H. Kuroiwa, H. Okamoto, and H. Kumagai, "Development of a 95-GHz Airborne Cloud Profiling Radar (SPIDER)", IEICE Trans. Commun., 2000, in press.

[2] J. M. Intrieri, G. L. Stephens, W. L. Eberhard and T. Uttal, "A Method for Determining Cirrus Cloud Particle Sizes Using Lidar and Radar Backscatter Technique," J. Appl. Meteor., **32**, 1074-1082 (1993).

[3] Lammeren, A.C.A.P., D. Donovan, and H. Bloemink, "SENSOR SYNERGY ALGORITHM: DEVELOPMENT AND VALIDATION", proceedings of the first international workshop on space borne cloud profiling radar 2000, 219-226 (2000).

[4] Okamoto, H. , M.Yasui, H.Horie, H.Kuroiwa, H.Kumagai, and S.Iwasaki, "OBSERVATION OF CLOUDS BY 95GHZ RADAR AND LIDAR SYSTEMS:RADIUS VERSUS FALL VELOCITY", Smith and Timofeyev (Eds.) IRS2000: Current Problems in Atmospheric Radiation, Deepak Publishing, 2000., submitted.

[5] Okamoto, H., S. Iwasaki, M. Yasui, H. Horie, H. Kuroiwa, and H. Kumagai, "95-GHz cloud radar and lidar systems:preliminary results of cloud micro-physics", In Wilheit, Masuko, and Wakabayashi (Eds) SPIE2000: Remote Sensing of the Atmosphere, Environment, and Space., 2000., submitted.

[6] Y. Takano and K. N. Liou, "Solar Radiative Transfer in Cirrus Clouds. Part I: Single-Scattering and Optical Properties of Hexagonal Ice Crystals," J. Atmos. Sci., **46**, 3-19 (1989).

[7] M. Born and E. Wolf, *Principles of Optics,* (PERGAMON PRESS, Oxford, 1975).

[8] Platt, C. M., "Lidar backscatter from horizontal ice crystal plates," J. Appl. Meteorol. **17**, 482-488 (1978).

[9] Kumagai, H., K. Nakamura, H. Hanado, K. Okamoto, N. Hosaka, N. Miyano, T. Kozu, N. Takahashi, T. Iguchi, and H. Miyauchi, "CRL Airborne Multiparameter

Precipitation Radar (CAMPR): System Description and Preliminary Results", IE-ICE Trans. Commun., **E79-B**, 770-778 (1996).

[10] Stephanes, G. L., *Remote Sensing of the Lower Atmosphere*, (New York, Oxford., 1994).

[11] Russchenberg, H. W. J, and L. P. Ligthart, "Backscattering by and Propagation Through the Melting Layer of Precipitation: A New Polarimetric Model", IEEE trans., **34**, 3-14 (1996).

[12] D. M. Winker, "THE PICASSO-CENA MISSION," in proceedings of the first international workshop on space borne cloud profiling radar 2000, 235-242 (2000).

[13] ATMOS-B1 Team/ESTO (Earth Science and Technology Organization), *3D-CLARE, Three Dimensional Cloud - Aerosol - Radiation Budget Experiment (proposal of ATMOS-B1 Mission)*, (Earth Science & Technology Organization, Japan, 2000).

Chapter 2

Anomalous backscattering enhancement by non-spherical ice crystals for lidar observation

Abstract

We examine the lidar backscattering by large non-spherical ice crystals on the basis of ray optics and diffraction theory. Our numerical computations show when large ice particles have flat surfaces and distance Z between the particles and a receiver is less than $1km$, an anomalous backscattering enhancement can be expected compared with spherical case, in the lidar observations. We first establish the criterion for this enhancement. Then modifications for the lidar equation are proposed in terms of dependence Z. Contrary to the spherical particles with their dependence of Z^{-2}, such dependences vary with particle's shape and orientations; Z^0 for hexagonal plate randomly oriented in horizontal plane, Z^{-1} for hexagonal column randomly oriented in horizontal plane.

2.1 Introduction

In order to forecast the future climate change, it is widely recognized that the role of clouds and their interaction with aerosols are one of the key problems to be understood. Such knowledges will be used to assess and to increase the potential of General Circulation Models (GCM). Especially vertical distribution of the clouds should be measured with certain accuracy for the surface radiative forcing by clouds. Lidar, as well as cloud radar ($95GHz$) [1, 2], is one of the promising tools [3, 4]. For last twenty years, there have been intensive ground based measurements by use of lidar and some progresses have been

8

made in the analysis. Fernald *et. al.* (1972) [5] developed analytical method for the inversion problem in lidar observations. Klett (1981) [6] modified their method to avoid instabilities in the inversion problems. Platt *et. al.* (1978) [7, 8] pointed out that some cirrus clouds produce a strong zenith-enhanced backscatter (ZEB). This phenomenon have been discussed by many authors (*e.g.*, Mishchenko *et. al.*, 1997 are references there in). Sassen (1991) [9] also showed the observational evidence of the alignment of the particle in relation to the horizontal plane by using the dual polarization lidar technique. Mishchenko *et. al.* (1997) considered disks and spheroids with size parameter up to 50 as ice crystals and calculated lidar backscattering from these particles by using T-matrix method. They showed "ZEB peak can be produced only by horizontally oriented disks but not by horizontally oriented spheroids or particles in random orientation". Up to now, several space borne lidar mission projects, PICASSO [11] in United States, ERM[12, 13] in Europe and ATMOS-B1[14] in Japan. To demonstrate the feasibility of space borne lidar, NASA had the experiment for the lidar on the Space Shuttle mission, which is called LITE [15].

In this paper, to analyze lidar signals by clouds, the scattering theory is developed to estimate backscattering by large non-spherical ice crystals with flat surfaces. In visible wavelength, ray-tracing method [16, 17] is widely used for the scattering by cloud particles. Since up to now there is no exact method in this domain for lidar backscattering, we consider ray-tracing method based on geometrical optics (GO) [16, 17] and Kirchhoff's diffraction theory (KD) [18, 19]. Note that in the usual GO, diffraction term is normally included only in the forward scattering but not in the side and backward directions. Because of this ignorance, the applicability of GO is limited. In this paper, we define "diffraction" as "the scattered light that can not be calculated by ray optics", that is, diffraction is diffused light induced by its characteristic of wave optics. Mishchenko *et. al.* (1997) actually discussed about pattern described by KD for the qualitative understanding of the computed results for spheroids and circular disks. Although we also discuss about KD, our main aim of this paper is to test the applicability of GO. Therefore we would like to distinguish between their approach and ours.

In section **2.2**, for the backscattering by a rectangular target, we analyze the diffraction pattern by a rectangular target where KD can be applicable. When the main lobe of the backscattered lidar signals is within a solid angle of the receiver viewed from the particle ($\delta\Omega_p$), we numerically prove that the backscattered power estimated by GO is in good agreement with that by KD. However when the main lobe is out of the $\delta\Omega_p$, GO is not applicable. In the former case, anomalous backscattering enhancement can occur. We propose the criterion for this enhancement as a function of wavelength, Z, the particle size, half width of the receiver R_t, shape and orientation. In section **2.3**, backscattering by

9

hexagonal ice crystal with various aspect ratios are estimated by GO, when the criterion is fulfilled. And we derive the modification to the usual lidar equation in order to take into account the anomalous backscattering enhancement.

2.2 Mechanism of backscattering enhancement

The geometry of the lidar observation is described in Fig.2.1 and the symbols used in this paper are defined in Table 2.1. In this section, we estimate the backscattering diffraction by the hexagonal column and hexagonal plate randomly oriented in horizontal plane (here after 2D-column and 2D-plate) by Kirchhoff's diffraction theory (KD)[18, 19]. Then we establish the criterion where backscattering enhancement can be expected.

2.2.1 Comparison between GO and KD for rectangular surface

For simplicity we start with rectangular particles as the non-spherical particles. And we also assume the shape of a receiver is rectangle (see Fig. 2.2). To calculate diffraction patterns by the rectangular particles, we use KD. The backscattering irradiance can be written as Eq. 2.1 in Fraunhofer approximation [18].

$$
\begin{aligned}
I_s(X, Y, \Psi) &= \frac{S^2}{\lambda^2} \frac{R_{fre}I_0}{Z^2} \left(\frac{\sin \Phi_X}{\Phi_X}\right)^2 \left(\frac{\sin \Phi_Y}{\Phi_Y}\right)^2 \\
\Phi_X &= kl(\phi_X - 2\sin \Psi)/2 \\
&= kl(X/Z - 2\sin \Psi)/2 \\
\Phi_Y &= ka\phi_Y/2 \\
&= kaY/2Z
\end{aligned}
\tag{2.1}
$$

where S denotes area of the scatter, R_{fre} is the reflectance of the rectangle calculated by Fresnel formula [21]. I_0 is incident intensity. λ and k are wavelength and wave number of interest. l and a ($l \geq a$) are the side lengths of the rectangle (see Fig. 2.2). The angle between the normal vector of the rectangle and the incident beam Ψ and angles meaning of ϕ_X and ϕ_Y are described in Fig. 2.2. The main lobe is defined as the irradiance stood out around $\Phi_X = 0$ and $\Phi_Y = 0$ (see Fig. 2.3). The scale of the main lobe on the receiver is described in Fig. 2.2 by introducing the characteristic lengths $R_{d,l}$ and $R_{d,a}$. By substituting $\Phi_X = \Phi_Y = \pi$ into Eq.2.1, $R_{d,l}$ and $R_{d,a}$ are obtained as

$$
\begin{aligned}
R_{d,l} &= \frac{Z\lambda}{l} \\
R_{d,a} &= \frac{Z\lambda}{a}.
\end{aligned}
\tag{2.2}
$$

When $\Psi = 0$, corresponding the situation where the incident beam is perpendicular to the surface of rectangular particles, integration of I_s in Eq. 2.1 is the total scattered power estimated by KD which agrees with that estimation by GO.

$$\int_{-\infty}^{\infty} dX \int_{-\infty}^{\infty} dY I_s(X, Y, 0) = SR_{fre}I_0. \tag{2.3}$$

Numerical integration of I_s also shows that the power of the main lobe becomes 81% of the total (see Fig. 2.4).

Fig. 2.5 shows the diffraction pattern by a rectangular target with orientational averaging where major axis of the rectangle is parallel to the Y axis and minor axis is rotated randomly ($0 < \Psi < \pi$) and these minimum irradiance are determined by $R_{d,l}$ (see Eq. 2.2). The shape of the pattern can be understood from the superposition of the pattern by rectangular. The received power calculated by GO is

$$P_{s,GO} = \frac{1}{2\pi} \frac{R_t}{Z} R_{fre}I_0 S \tag{2.4}$$

where R_t is a half width of the receiver (see Appendix 2.5.1). When R_t is equal to $R_{d,l}$, numerical integration of I_s described in Fig. 2.5 shows received power calculated by KD becomes 90% of $P_{s,GO}$.

Therefore, we can propose the criterion for the applicability of GO to be

$$R_t > R_{d,l}. \tag{2.5}$$

Although we derived about this criterion for the particles without any rotations on X-Y plane, the criterion can also be applied for the particle but randomly oriented in horizontal plane; *i.e.* the major axis of the particle is rotated around Z axis and the minor axis is rotated around the major axis. This is because the applicability of GO (in Eq. 2.5) does not depend on the angle between X axis and the major axis of the target. Please note the received power in Eq. 2.3 and Eq. 2.4 have different Z dependence, contrary to the usual lidar equation [22, 23] dependency, which has Z^{-2} (in Eq. 2.6).

$$P_r(Z) = CZ^{-2}\{\sigma_{bk,g} + \sigma_{bk,p}\}e^{-2(\tau_g + \tau_p)} \tag{2.6}$$

where C is the constant of the lidar system. σ_{bk} is the backscattering coefficient and τ is the optical depth. The suffixes g and p mean gas and particle. This difference of Z-dependence suggests, when the condition in Eq. 2.5 is fulfilled, a backscattering enhancement induced by the different Z-dependence (BEZ) of the received power can be expected and quantitative comparison between spherical and non-spherical particles gives in section **2.3**. Please note the phenomenon of backscattering enhancement discussed here is different from the zenith-enhanced backscattering (ZEB) previously discussed in many authors (Mishchenko *et. al.*, 1997).

11

2.2.2 Criterion for the application of GO

Particle's orientation might depend on its shape. Ono (1969)[24] showed the particle is aligned as its longest axis is parallel to the horizontal plane. For example, when hexagonal column with aspect ratio $asp(\equiv l/2a) = 3$ is considered, symmetrical axis is parallel to the horizontal plane (2D-column) (see Fig. 2.6(a)). For hexagonal plate with $asp = 1/3$, symmetrical axis is perpendicular to the horizontal plane (2D-plate) (see Fig. 2.6(b)).

When the 2D-plate is considered, we assume the backscattered irradiance I_s for 2D-plate is the same as that for the square which has the same geometrical cross section of 2D-plate. That is, I_s for the square is obtained by using Eq. 2.1 with $l = a = R_{sq}$, where R_{sq} is the side length of the square. Similar to the discussion for a rectangular particles, when the criterion in Eq. 2.7 is fulfilled, GO can be applied and the BEZ is expected.

$$
\begin{aligned}
R_t &> R_c \\
R_c &= \frac{Z\lambda asp^{1/3}}{(\frac{4}{3}\pi^4)^{1/12}r_{eq}}.
\end{aligned}
\tag{2.7}
$$

where R_c is the critical radius given by Eq. 2.7. For the particles with volume equivalent radius $r_{eq} = 100\mu m$, $Z = 100m$, $asp = 1/6$, $R_c = 0.2m$ and $R_t > 0.2m$, BEZ can be expected. In Fig. 2.7 (a), we describe the region where backscattering enhancement can be observed, in terms of Z, volume equivalent radius r_{eq} and asp.

The backscattered irradiance by 2D-column might be six times larger than that by the rectangle where geometrical cross section of the rectangle is the same as that of one of rectangles on hexagonal columns. Thus the applicability of GO is the same as that for the rectangular target randomly oriented in horizontal plane as discussed in subsection **2.2.1**.

$$
\begin{aligned}
R_t &> R_c \\
R_c &= \frac{Z\lambda}{2(\frac{4\pi}{9\sqrt{3}})^{1/3}asp^{2/3}r_{eq}}.
\end{aligned}
\tag{2.8}
$$

For the particles with $r_{eq} = 100\mu m$, $Z = 100m$, $asp = 3$ and $R_c = 0.2m$ and $R_t > 0.2m$, BEZ can be expected (in Fig. 2.7 (b)).

For 3D-column and 3D-plate, we assume the criterion is as same as that of 2D-column.

2.3 Analysis of the lidar backscattering by pristine hexagonal crystals

In this section, we restrict on analysis to the case where the criterion Eq. 2.7 or Eq. 2.8 is fulfilled. For the arbitrary shaped particle, it is not possible to solve KD. Since GO

is in good agreement with KD (in section **2.2**), we rely on GO. We assume that there is no multiple scattering. In order to estimate the lidar backscattering signals by pristine hexagonal ice crystals, we first need to reformulate the lidar equation. We start to the general formulation of the lidar equation (in Eq. 2.9).

$$P_r(Z) = I_0 \int_{V_z} dv \int_{size} dr \frac{dn(r)}{dr} \int_{\delta\Omega(\theta=180-\delta\theta_p)}^{\delta\Omega(\theta=180)} d\Omega \frac{dC_{sca}(180)}{d\Omega} e^{-2(\tau_g+\tau_p)}$$

$$\delta\Omega(180) = \pi\delta\theta^2 \qquad\qquad (2.9)$$

where V_z denotes scattering volume illuminated by laser. $dn(r)/dr$ is size distribution. θ is a scattering angle.

2.3.1 Case for spherical particle

In the Mie scattering, $dC_{sca}(180)/d\Omega$ is constant [21]. Therefore, Eq. (2.9) becomes

$$P_r = I_0 V_z \pi (\frac{R_t}{Z})^2 \int_{size} dr \frac{dn(r)}{dr} \frac{dC_{sca}(180)}{d\Omega} e^{-2(\tau_g+\tau_p)} \qquad\qquad (2.10)$$

This corresponds the usual lidar equation and proportional to Z^{-2}.

2.3.2 Case for 2D-column

In the case of hexagonal column randomly oriented in horizontal plane (2D-column), $\delta C_{sca}(180)/\delta\Omega$ is not converged (Fig. 2.8). To overcome this problem, we rewrite the lidar equation Eq. 2.9 by introducing $d\theta$ instead of using $d\Omega$.

$$P_r = I_0 \int_{V_z} dv \int_{size} dr \frac{dn(r)}{dr} \int_{180-\delta\theta_p}^{180} d\theta \frac{dC_{sca}(180)}{d\theta} e^{-2(\tau_g+\tau_p)} \qquad\qquad (2.11)$$

In Fig.2.9, each line corresponds to the results for different random seeds used in the computations (optical constant [20] is $1.31+i2.54^{-9}$, wavelength of interest is 0.532 μm). It is found that $\delta C_{sca}(\theta)/\delta\theta$ is constant for the backscattering direction. Therefore, Eq. (2.11) becomes

$$P_r = I_0 V_z \frac{R_t}{Z} \int_{size} dr \frac{dn(r)}{dr} C_{sca} \frac{\delta C_{sca}(180)/\delta\theta}{C_{sca}} e^{-2(\tau_g+\tau_p)} \qquad\qquad (2.12)$$

In this case, the lidar equation becomes proportional to Z^{-1}.

When we neglect the absorption of ice crystals, $\delta C_{sca}(180)/\delta\theta/C_{sca}$ is independent on crystal size and C_{sca} is $2G$, where G is the geometrical cross section. This is because δC_{sca} and C_{sca} depend on reflectance R and transmittance T and R and T does not depend on size. Thus, Eq. (2.12) becomes

$$P_r = 2I_0 V_z \frac{\delta C_{sca}(180)/\delta\theta}{C_{sca}} \frac{R_t}{Z} \int_{size} dr \frac{dn(r)}{dr} G(r) e^{-2(\tau_g+\tau_p)} \qquad\qquad (2.13)$$

13

Since cylindrical column might be approximated by infinite polygonal column and Z dependency of cylindrical column [21] is Z^{-1}, we can naturally understand Z^{-1} dependence of the 2D-column appeared in Eq. 2.12.

2.3.3 Case for 2D-plate

In GO, backscattered power of the hexagonal plate randomly oriented in horizontal plane (2D-plate) can be approximated by that of a slab with finite thickness and infinite width. We call this method Finite Slab Approximation (FSA). For this geometry, it is not necessary to use ray-tracing method to estimate backscattering.

The reflectance R_{fsa} is

$$R_{fsa} = \frac{\int_{\delta\Omega(\theta=180-\delta\theta_p)}^{\delta\Omega(\theta=180)} d\Omega \frac{dC_{sca}(180)}{d\Omega}|_{\theta=180} I_0}{GI_0}$$

$$= \frac{2R_{fre,\perp}}{1 + R_{fre,\perp}} \tag{2.14}$$

where $R_{fre,\perp}$ is the reflectance for the vertical incident light [21] estimated by Fresnel formulas.

Therefore, Eq. (2.9) becomes

$$P_r \cong I_0 V_z R_{fsa} \int_{size} dr \frac{dn(r)}{dr} G(r) e^{-2(\tau_g + \tau_p)}. \tag{2.15}$$

Similar to the rectangular particle, backscattered power for 2D-plate does not depend on Z.

2.3.4 Case for 3D-column and 3D-plate

Hexagonal column and plate randomly oriented in space (3D-column and 3D-plate) are considered in this subsection. We also start from Eq. (2.11). $\delta C_{sca}(180)/\delta\theta$ turns out to be constant by using GO (see Figs. 2.10(a) and (b)). Its size, wavelength of interest and optical constant are the same as those values used in subsection **2.3.2**. Each line corresponds to the results for the different random seeds in the computations. The lidar equation becomes

$$P_r = I_0 V_z \frac{R_t}{Z} \int_{size} dr \frac{dn(r)}{dr} C_{sca} \frac{\delta C_{sca}(180)/\delta\theta}{C_{sca}} e^{-2(\tau_g + \tau_p)} \tag{2.16}$$

For the non-absorption targets, Eq.2.16 further reduce to

$$P_r = 2I_0 V_z \frac{\delta C_{sca}(180)/\delta\theta}{C_{sca}} \frac{R_t}{Z} \int_{size} dr \frac{dn(r)}{dr} G(r) e^{-2(\tau_g + \tau_p)} \tag{2.17}$$

14

2.3.5 Discussion

In Fig. 2.11, we compute $P_r(Z)$ for different particle shapes and orientations based on the newly derived lidar equations. For the same volume of ice crystal in considered, 2D-plate can produce the largest signals when main lobe is within $\delta\Omega_p$ and thus GO is applicable.

When the 2D-column with $r_{eq} = 100\mu m$ and $asp = 3$ is at $Z = 100m$, GO can be valid and $P_r(Z)$ is about 50 times larger than that for the sphere with same volume (see Fig. 2.11(a)). For 2D-plate, it is about 1000 times larger than that for the sphere (see Fig. 2.11(b)).

2.4 Summary

We analyze backscattering by non-spherical particles which have flat surfaces with various shape and orientations by using Kirchhoff's diffraction theory (KD) and ray-tracing method based on geometrical optics (GO).

First, we compare KD and GO and find when the main lobe of the backscattered signal is within the solid angle of the receiver viewed from the particle ($\delta\Omega_p$), GO is in good agreement with KD. For a rectangle, Z dependence of the received backscattered power turns to be different i.e. Z^0 or Z^{-1} from that for spherical; i.e. Z^{-2}. We establish the applicability of GO as a function of λ, Z, r_{eq}, R_t, shape and orientation.

We consider the following scattering targets, hexagonal column and plate randomly oriented in horizontal plane (2D-column and 2D-plate) and hexagonal column and plate randomly oriented in space (3D-column and 3D-plate). For the 2D-plate, we apply Finite Slab Approximation and for others we apply GO. It is found that Z dependence of the lidar equations is Z^0 for 2D-plate and Z^{-1} for 2D-column, 3D-column and 3D-plate. Note the dependence of the widely used lidar equation is Z^{-2}, corresponding to the case of the sphere. Thus it is expected to observe the backscattering enhancement induced by the different Z-dependence from Z^{-2} (BEZ) when the criterion for the applicability of GO is fulfilled. This modification of lidar equation might be relevant for airborne-type as well as for ground-based observation for cold cloud located in low altitude, where the distance between the scatter and receiver $< 100m$.

When the main lobe of the backscattering signal is out of $\delta\Omega_p$, diffraction term is not negligible and GO can not be applied. The lidar equation for the above case is currently investigated by using KD and will be reported in future paper.

For $Z = 1000m$, only very large particle can produce BEZ, i.e., $r_{eq} > 1mm$. However, the shapes of size distributions is broad, larger particles can contribute to the total backscattering. Thus, Z dependence might also be different from Z^{-2} even if the mean

radius is smaller than $1mm$. Thus in such situation this modification becomes important. For the effect of size distribution, we will describe in a next paper.

These results are not only important for the scattering by the pristine hexagonal ice crystals, but also for the particles with flat surfaces except for the highly irregular shaped particles [25], such as Koch fractals [17].

2.5 Appendix

2.5.1 Received power for a rectangular target randomly oriented in horizontal plane

The configuration of the particle, incident and scattered light is sketched in Fig. 2.12. In GO, scattered irradiance by a rectangular target is

$$I_s = R_{fre} I_0 \delta_{\theta, 2\Psi}. \tag{2.18}$$

where I_0 is incident intensity, R_{fre} is reflectance of the rectangular particle, $\delta_{\theta, 2\Psi}$ is Kronecker's delta and Ψ is the angle between the normal vector of the rectangle and the incident beam. Therefore, received power derived by a rectangular target randomly oriented in horizontal plane becomes

$$P_{s,GO} = I_s S \frac{2\Psi_m}{2\pi} = \frac{1}{2\pi} \frac{R_t}{Z} R_{fre} I_0 S. \tag{2.19}$$

where Ψ_m is $R_t/2Z$ when $\Psi_m << 1$.

Table 2.1: The definition of symbols

I_0	incident intensity
$I_s(X, Y, \Psi)$	backscattering irradiance at (X,Y)
$P_r(Z)$	received power
Ψ	rotation angle around Y axis
$R_{d,a}$, $R_{d,l}$	the scale of the main lobe obtained by KD (see Fig. 2.2).
R_{fre}	reflectance of Fresnel formula
$R_{fre,\perp}$	reflectance of Fresnel formula for the vertical incident light
R_t	a half width of the receiver (telescope)
S	area of the scatter ($a \times l$)
Z	altitude of the scatter
asp	$l/2a$ (see Fig. 2.6)
a, l	side lengths of the rectangle
$\delta\Omega$	solid angle
$\delta\Omega_p$	solid angle of the receiver viewed from the scattered particle
$dn(r)/dr$	size distribution
k	wave number
λ	wavelength
r_{eq}	volume equivalent radius
σ_{bk}	backscattering coefficient
τ	optical depth
θ	scattering angle

Table 2.2: Criteria for the applicability of geometrical optics (GO) for the particles with different shapes. R_t is a half width of the receiver and r_{eq} is the volume equivalent radius. Z and λ are altitude of the scatter and wavelength of interest.

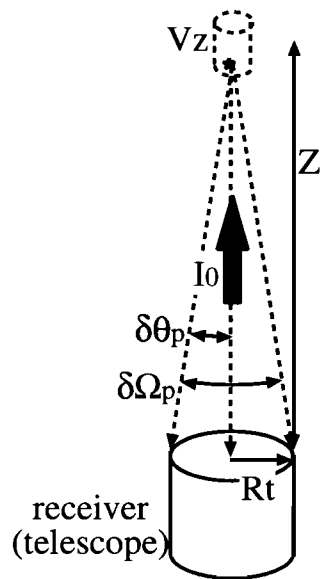|	criterion for applicability of GO
2D-column	$R_t > \dfrac{Z\lambda}{2(4\pi/9/\sqrt{3})^{1/3}asp^{2/3}r_{eq}}$
2D-plate	$R_t > \dfrac{Z\lambda asp^{1/3}}{(4\pi^4/3)^{1/12}r_{eq}}$
3D-column	$R_t > \dfrac{Z\lambda}{2(4\pi/9/\sqrt{3})^{1/3}asp^{2/3}r_{eq}}$
3D-plate	$R_t > \dfrac{Z\lambda}{2(4\pi/9/\sqrt{3})^{1/3}asp^{2/3}r_{eq}}$

Figure 2.1: The geometry of the lidar observation. I_0 is the incident light and V_Z denotes the scattering volume illuminated by laser. Particles are located at the altitude Z. $\delta\Omega_p$ is a solid angle of the receiver viewed from the particle. $\delta\theta_p$ is defined as $\tan^{-1} R_t/Z$.
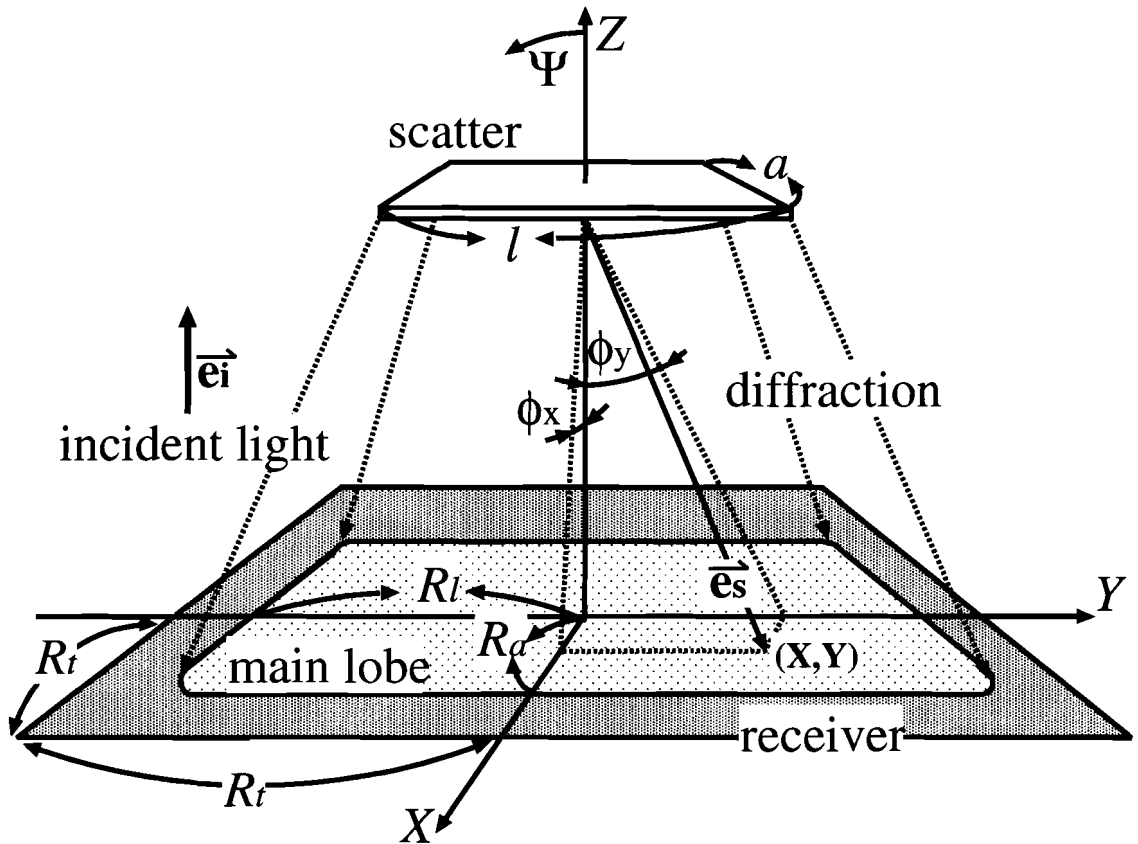
Figure 2.2: Geometrical configuration between the incident and scattered electro-magnetic fields and scattered target. Length of the target are specified by a along X axis and l along Y axis ($l \geq a$), respectively. $\vec{e_i}$ and $\vec{e_s}$ denote the incident and scattered directions. Ψ is an angle between the normal vector on the surface and the incident beam. In this figure, main lobe (dotted area) is within receiver (shadowed area) and Ψ is 0.
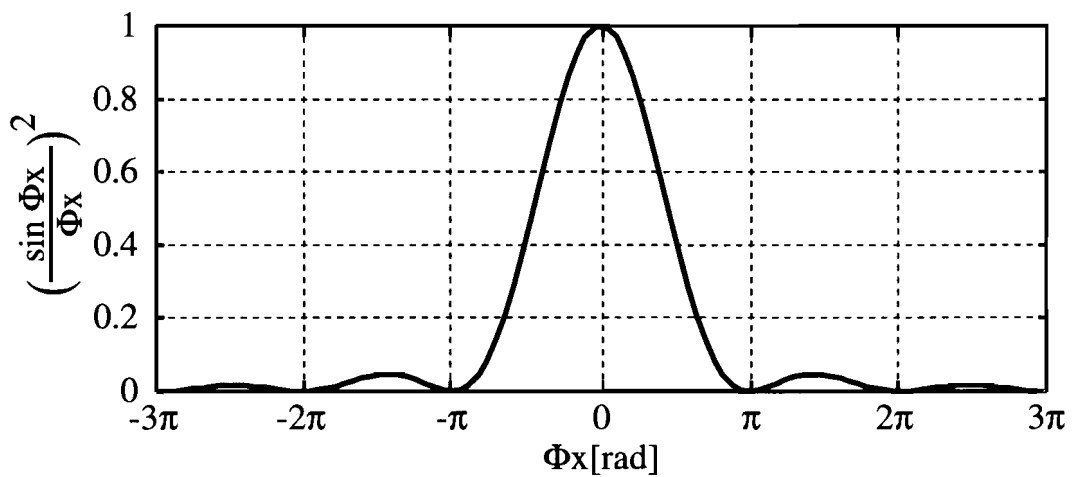
Figure 2.3: The backward diffraction pattern by the rectangular target normalized at maximum. We define "the main lobe" as "the scattered light for $-\pi < \Phi_X < \pi$ (dashed curve)", where Φ_X is given in the text.
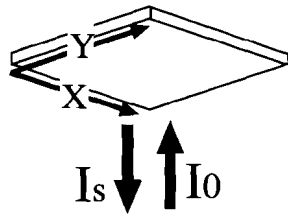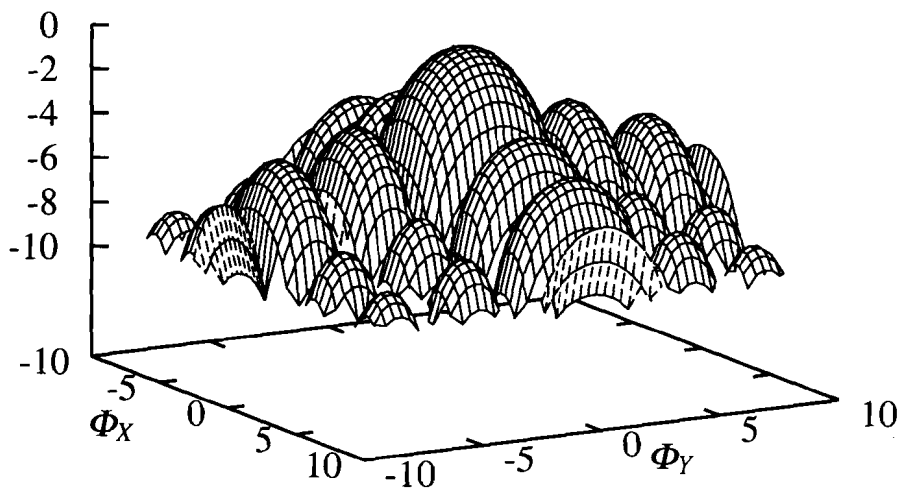
Figure 2.4: The diffraction pattern for the rectangular shaped target with a fixed orientation normalized at the maximum. Φ_X and Φ_Y are given in the text. The main lobe is stood out around $\Phi_X = 0$ and $\Phi_Y = 0$.
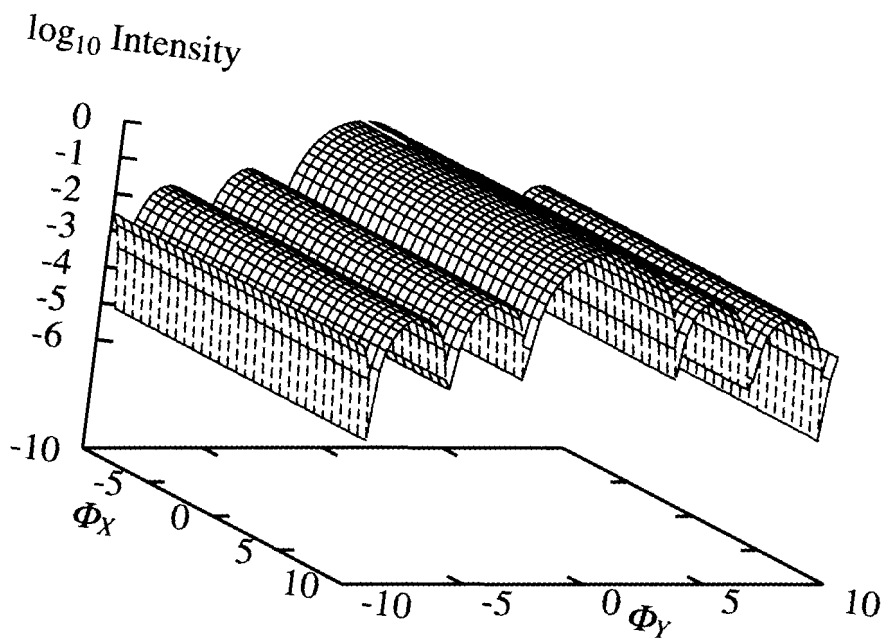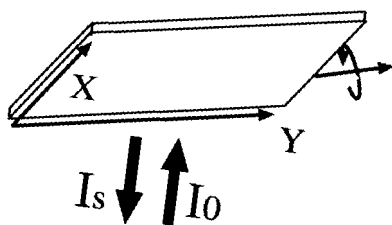
Figure 2.5: The same as Fig. 4 but for the rectangular target with orientational averaging where major axis of the rectangle is parallel to the Y axis and minor axis is rotated randomly.
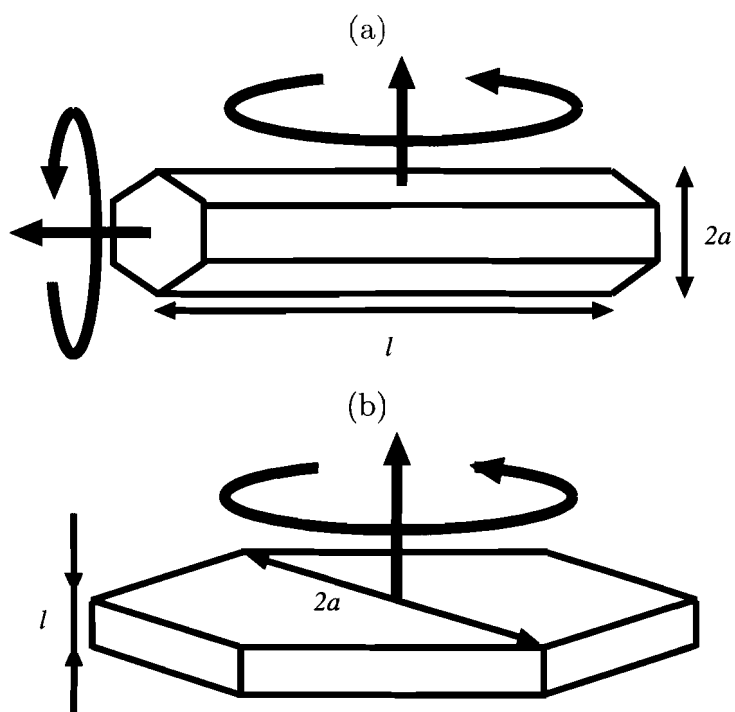
Figure 2.6: Alignment of a hexagonal crystal. (a) symmetrical axis is parallel to the horizontal plane (2D-column) and (b) symmetrical axis is perpendicular to the horizontal plane (2D-plate).
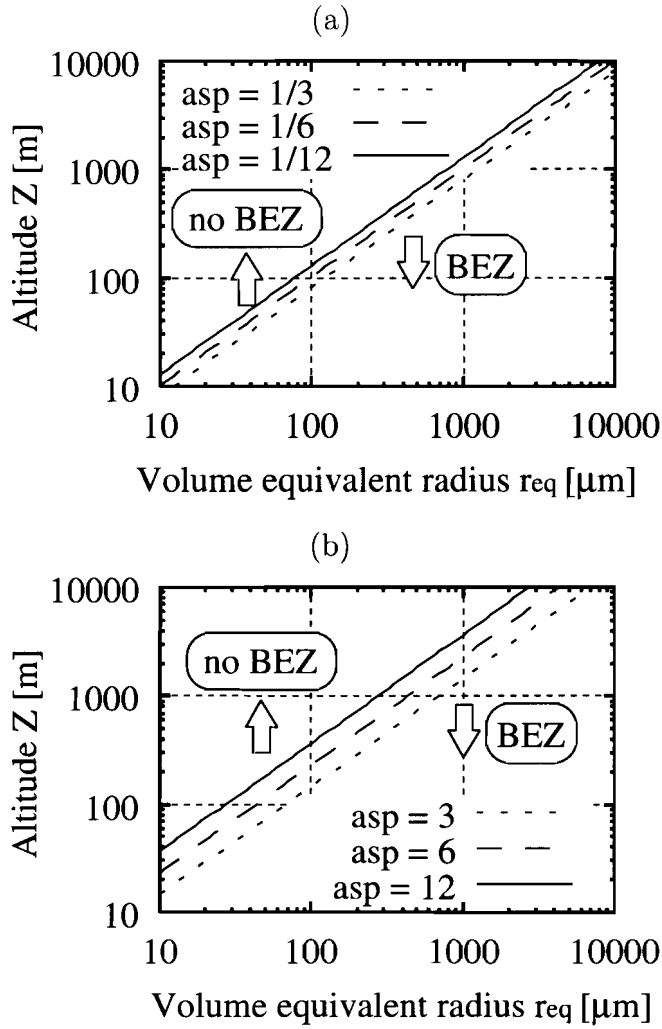
Figure 2.7: The criterion that backscattering enhancement is occurred. Under these lines, Z^{-2} dependence on the lidar equation is violated and backscattering enhancement occurs. $R_t = 0.2m$. (a) hexagonal plate randomly oriented in horizontal plane (2D-plate). (b) hexagonal column randomly oriented in horizontal plane (2D-column). asp describes aspect ratio.
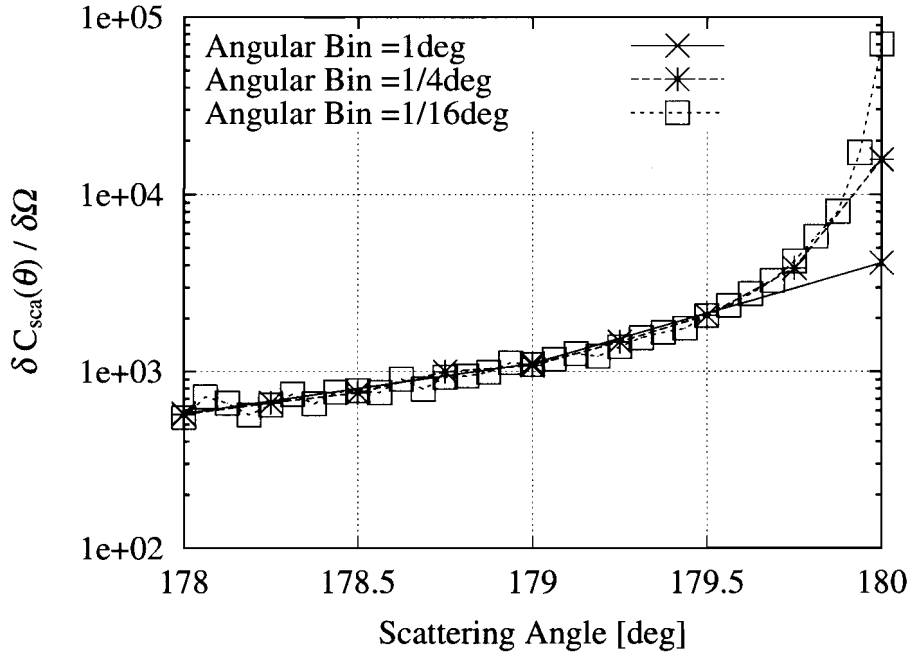
Figure 2.8: The relation between differential cross section $\delta C_{sca}(\theta)/\delta\Omega$ for 2D-column and scattering angle θ. Each line corresponds to the different angular bin $\delta\theta$. When the angular bin is smaller, $\delta C_{sca}(180)/\delta\Omega$ becomes larger.
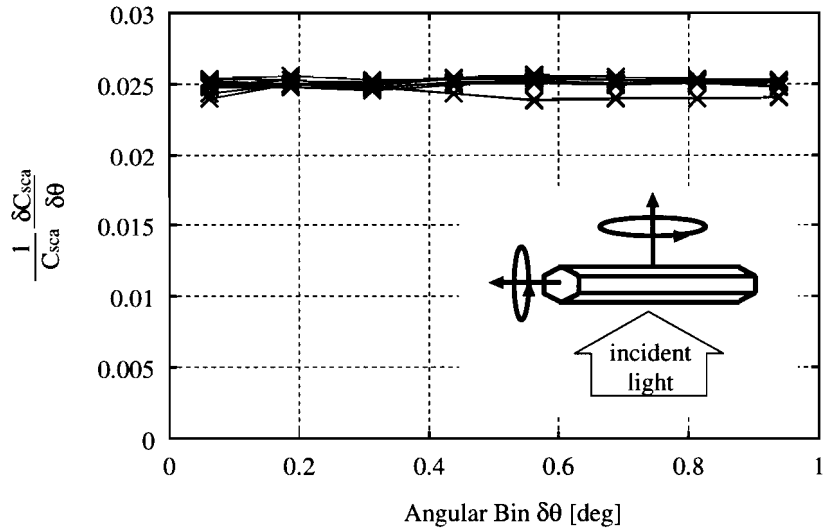
Figure 2.9: The relation between $\delta C_{sca}(180)/\delta\theta$ for 2D-column ($l = 86\mu m, a = 14\mu m$) and $\delta\theta$ calculated by the ray-tracing method. Each line corresponds the results of different random seeds in the computation.
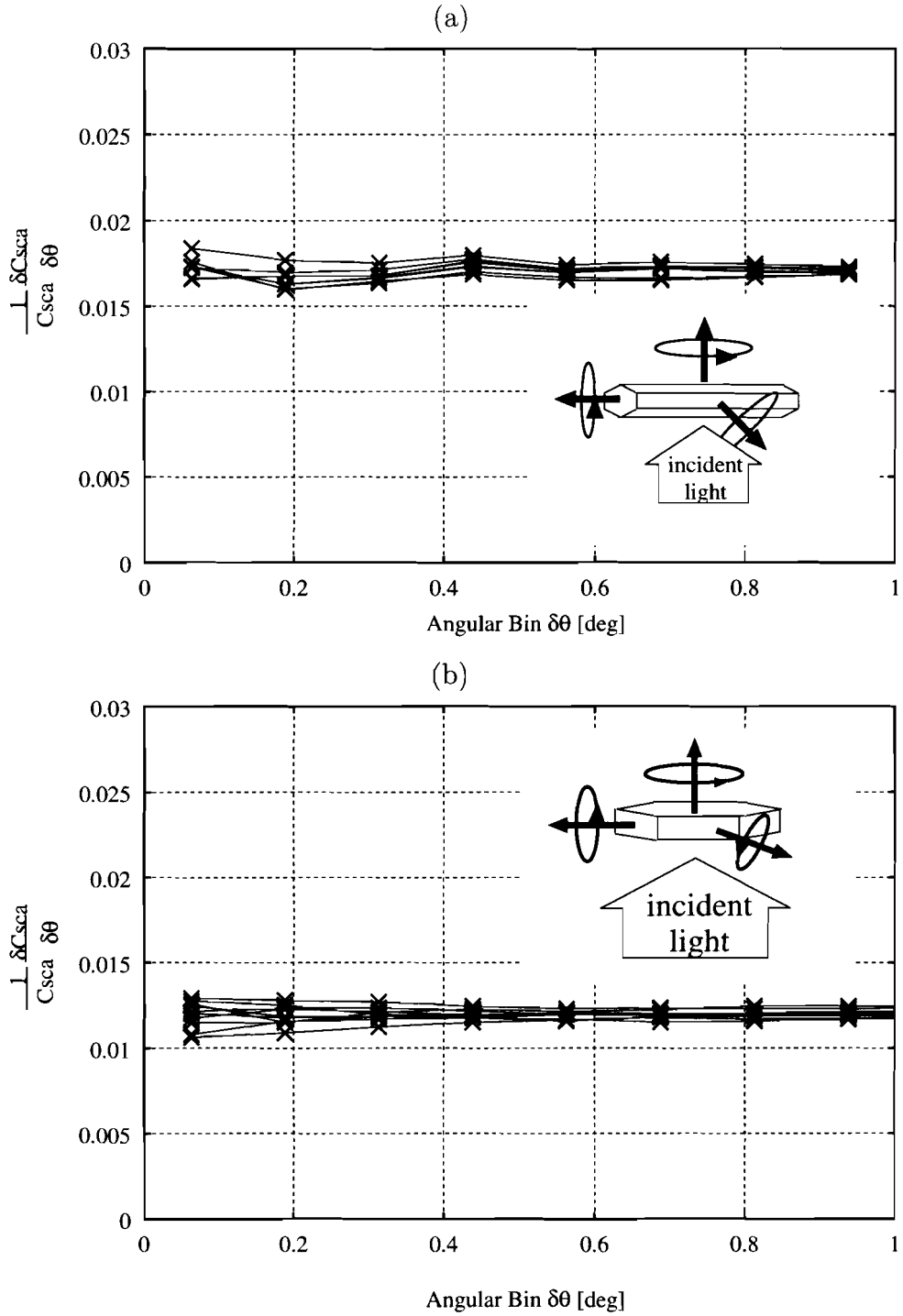
Figure 2.10: The relation between $\delta C_{sca}(180)/\delta\theta$ for (a) 3D-column ($l = 86\mu m, a = 14\mu m$) (b) 3D-plate ($l = 20\mu m, a = 30\mu m$) and $\delta\theta$ calculated by the ray-tracing method. Each line corresponds to the results for different random seeds in computations.
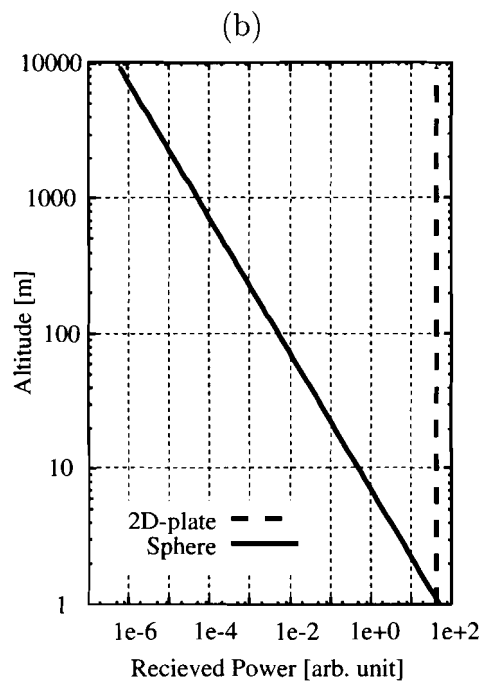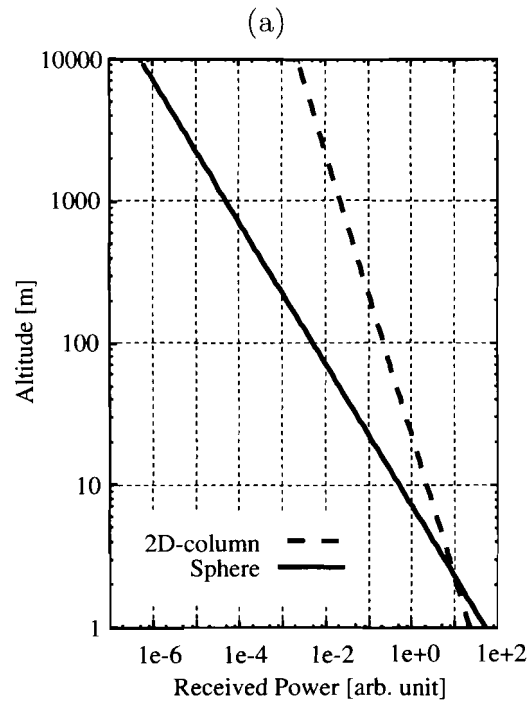
Figure 2.11: (a) Comparison between the backscattered power $P_r(Z)$ for sphere and that for the 2D-column when BEZ can be expected. (b) the same as (a) but for 2D-plate.

27
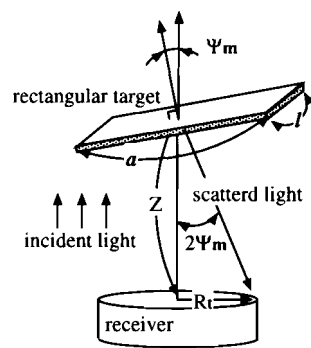
Figure 2.12: Geometrical configuration between the incident and scattered electromagnetic fields and the rotation of a scattered target.

Bibliography

[1] E. Raschke and M. Quante, "DO WE NEED A CLOUD PROFILING RADAR IN SPACE?", proceedings of the first international workshop on space borne cloud profiling radar 2000, 15-22 (2000).

[2] H. Horie, T. Iguchi, H. Hanado, H. Kuroiwa, H. Okamoto, and H. Kumagai, "Development of a 95-GHz Airborne Cloud Profiling Radar (SPIDER)", IEICE Trans. Commun., 2000, in press.

[3] H. Okamoto, S. Iwasaki and H. Horie, "Algorithm studies for radar and lidar studies", proceedings of the first international workshop on space borne cloud profiling radar 2000, 227-232 (2000).

[4] J. M. Intrieri, G. L. Stephens, W. L. Eberhard and T. Uttal, "A Method for Determining Cirrus Cloud Particle Sizes Using Lidar and Radar Backscatter Technique," J. Appl. Meteor., **32**, 1074-1082 (1993).

[5] F. G. Fernald, B. M. Herman, and J. A. Reagan, "Determination of Aerosol Height Distributions by Lidar," J. Appl. Meteor., **11**, 482-489 (1972).

[6] J. D. Klett, "Stable analytical inversion solution for processing lidar returns," Appl. Opt. **20,** 211-220 (1981).

[7] C. M. Platt, "Lidar backscatter from horizontal ice crystal plates," J. Appl. Meteorol. **17,** 482-488 (1978).

[8] C. M. Platt, N. L. Abshire, and G. T. McNice, "Some microphysical properties of an ice cloud from lidar observation of horizontally oriented crystals," J. Appl. Meteorol. **17,** 1220-1224 (1978).

[9] K. Sassen, The polarization lidar technique for cloud research: A review and current assessment. Bull. Am. Meteorol. Soc. **72,** 1848-1866 (1991).

[10] M. I. Mishchenko, D. J. Wielaard, and B. E. Calson, "T-matrix computations of zenith-enhanced lidar backscatter from horizontally oriented ice plates," Geophys. Res. Lett., **24**, 771-774, (1997).

[11] D. M. Winker, "THE PICASSO-CENA MISSION," in proceedings of the first international workshop on space borne cloud profiling radar 2000, 235-242 (2000).

[12] J. P. V. P. Baptista, A. Culoma, P. Ingmann, W. Leibrandt, C.-C. Lin and R. Meynart, "THE EARTH RADIATION MISSION: THE ROLE OF CLOUDS AND AEROSOLS," in proceedings of the first international workshop on space borne cloud profiling radar 2000, 243-249 (2000).

[13] C. C. Lin, W. Leibrandt, U. Mallow, and R. Bordi, "CPR DESIGN AND DEVELOPMENT STATUS FOR THE ESA EARTH RADIATION EXPLORE MISSION," in proceedings of the first international workshop on space borne cloud profiling radar 2000, 251-256 (2000).

[14] ATMOS-B1 Team/ESTO (Earth Science and Technology Organization), *3D-CLARE, Three Dimensional Cloud - Aerosol - Radiation Budget Experiment (proposal of ATMOS-B1 Mission)*, (Earth Science & Technology Organization, Japan, 2000).

[15] D. M. Winker, R. H. Couch, and M. P. McCormick, "An overview of LITE: NASA's Lidar In-space Technology Experiment," Proc. IEEE, **84**, 164-180 (1996).

[16] Y. Takano and K. N. Liou, "Solar Radiative Transfer in Cirrus Clouds. Part I: Single-Scattering and Optical Properties of Hexagonal Ice Crystals," J. Atmos. Sci., **46**, 3-19 (1989).

[17] A. Macke, J. Mueller, and E. Raschke, "Single Scattering Properties of Atmospheric Ice Crystals," J. Atmos. Sci., **53**, 2813-2825 (1996).

[18] M. Born and E. Wolf, *Principles of Optics*, (PERGAMON PRESS, Oxford, 1975).

[19] Jackson, J.D., *Classical Electrodynamics*, (Wiley, New York., 1983).

[20] S. G. Warren, "Optical constants of ice from the ultraviolet to the microwave," Appl. Opt. **23**, 1206-1225 (1984).

[21] C. F. Bohren and D. R. Huffman, *Absorption and Scattering of Light by Small Particles*, (Wiley, New York., 1983)

[22] F. G. Fernald, "Analysis of atmospheric lidar observations: some comments," Appl. Opt. **23**, 652-653 (1984).

[23] G. L. Stephanes, *Remote Sensing of the Lower Atmosphere*, (New York, Oxford., 1994), pp. 427-438.

[24] A. Ono, "The Shape and Riming Properties of Ice Crystals in Natural Clouds," J. Atmos. Sci.,**26**, 138-147 (1969).

[25] H. C. van de Hulst, *Light Scattering by Small Particles*, (Dover, New York., 1957).

Chapter 3

Analysis of lidar backscattering enhancement for pristine hexagonal ice crystals

Abstract

We analyze lidar backscattering enhancement for pristine hexagonal ice crystals by using Fraunhofer diffraction based on Kirchhoff's diffraction theory (KD). Our numerical computations show that received power $P_r(Z)$ at the altitude Z in lidar equation is proportional to $Z^{-\alpha}$, where α is a function of Z, size and shape of particles. $P_r(Z)$ is proportional to $Z^{-1.5}$ for hexagonal plate and column randomly oriented in horizontal plane at $Z=200$ m where its aspect ratios are 1/3 and 3 and mode radiuses are $100\mu m$. Our calculations suggest hexagonal ice crystals that have mode radiuses of 100 μm and 30 μm with perfectly oriented in horizontal plane have anomalous backscattering enhancement compared with a sphere at even high altitude. This might explain the phenomena reported by Platt *et. al.* (1978)[1, 2].

3.1   Introduction

Lidar is one of the most effective tools to investigate the cloud profiles such as vertical structure, shapes and sizes of ice crystals, which are the unknown factors to estimate the radiative properties of clouds with high accuracy. Therefore, for last twenty years, there have been intensive ground-based measurements by use of lidar and some progresses have been made in the analysis. Fernald *et. al.* (1972) [3] developed an analytical method for the inversion problem in lidar observations. Klett (1981) [4] modified their method

to avoid instabilities in the inversion problem. Besides, there are some observational evidence which shows non-sphericity plays a key role. Platt *et. al.* (1978) [1, 2] showed that some unusual lidar returns from a middle-level cloud were observed. They also showed ice clouds in the zenith gave a very high backscattering but a very small depolarization, which is called zenith-enhanced backscatter (ZEB). Mishchenko *et. al.* (1997) considered disks and spheroids with size parameter up to 50 (*e.g.* $r = 5\mu m$ at $\lambda = 0.63\mu m$) as ice crystals and calculated lidar backscattering from these particles by using T-matrix method. They showed "ZEB peak can be produced only by horizontally oriented disks but not by horizontally oriented spheroids or particles in random orientation". Despite from these efforts, there is a theoretical difficulty in interpretation of lidar signals. That is, in lidar signals, it is not possible to derive analytical solutions for non-spherical particles when the size of particles is much larger than the wavelength. Ray-tracing method is widely used in visible analysis, however, it has also a fundamental difficulty in backscattering. The applicability of this method is tested and it turns out that geometrical optics (GO) can be applicable when the altitude is very close to the ground (*e.g.* 100 m)[6]. Our final goal of this study is to explain the mechanism of unusual lidar returns showed by Platt *et. al.* (1978)[1, 2].

At first, we start with Fraunhofer diffraction based on Kirchhoff's diffraction theory (KD) [7, 8]. In section **3.2**, the theoretical produces are given. Then we analyze the backscattering pattern by a rectangular target. In section **3.3**, we calculate the scattering by hexagonal columns and plates randomly oriented in horizontal plane and discuss the differences of backscattering between spheres and hexagonal crystals.

3.2   Scattering by rectangular particles

In this section, we calculate the backscattering properties by the rectangular particles with fixed orientation and randomly oriented in horizontal plane (here after 2D-rectangle).

3.2.1   Definition of symbols and diffraction pattern

The geometry of the lidar observation is described in Fig. 3.1. We assume the shape of a receiver is rectangle.

To calculate diffraction pattern by the rectangular particles, we use Kirchhoff's diffraction theory (KD)[7, 8]. The backscattering irradiance can be written as Eq. 3.1 in Fraunhofer

Figure 3.1: The geometry of the lidar observation. I_0 is the incident light. A particle is located at the altitude Z. Length of the target is specified by a along X axis and l along Y axis ($l \geq a$), respectively. $\vec{e_i}$ and $\vec{e_s}$ denote the incident and scattered directions.

approximation [5, 7] which is derived from KD.

$$
\begin{aligned}
I_s(x, y, Z, \Psi) &= \frac{G^2}{\lambda^2} \frac{R_{sl} I_0}{Z^2} \left(\frac{\sin \Phi_X}{\Phi_X}\right)^2 \left(\frac{\sin \Phi_Y}{\Phi_Y}\right)^2 e^{-2\tau} \\
\Phi_X &= kl(x/Z - 2\sin\Psi)/2 \\
\Phi_Y &= kay/2Z
\end{aligned}
\tag{3.1}
$$

where G denotes geometrical cross section of the scatter, R_{sl} is the reflectance of the slab with some thickness and it is calculated by geometrical optics (GO) [12]. I_0 is incident intensity. τ is the optical depth. λ and k are wavelength and wave number of interest. l and a ($l \geq a$) are the side length of the rectangle (see Fig. 3.1). Ψ denotes the angle between the normal vector of the rectangle and the incident beam. The horizontal distribution of backscattered irradiance by a scatter is calculated in Fig. 3.2 (a).

3.2.2 Scattering by the rectangular particles with fixed orientation

For a rectangular particle with fixed orientation with $\Psi = 0$, backscattered power into the receiver is formulated by

$$
P_r(Z) = C' \int_{-R_t}^{R_t} dx \int_{-R_t}^{R_t} dy I_s(x, y, Z, 0),
\tag{3.2}
$$

where R_t is the half width of the receiver and C' is the constant of the lidar instrument, which is also appeared in usual lidar equation (Eq. 3.5).

34

Case for very low cloud

When the altitude of cloud is less than 80 m, the size of rectangle is 200 $\mu m \times$ 200 μm, and the receiver is much larger than 0.3 m, most of the backscattered power is received by the receiver (see Fig. 3.2 (b)) and is estimated by substitution of Eq. 3.1 into Eq. 3.2,

$$P_r(Z) = C' R_{sl} I_0 G e^{-2\tau}. \tag{3.3}$$

It turns out that $P_r(Z)$ does not depend on Z, contrary to the spherical particles where $P_r(Z)$ is proportional to Z^{-2}.

Case for high cloud

When altitude is larger than 2 km and other conditions such as sizes of rectangle and receiver are the same as those in previous subsection. Eq. 3.2 becomes

$$P_r(Z) = C' \frac{4G^2}{\lambda^2} \frac{R_{sl} I_0}{Z^2} R_t^2 e^{-2\tau}. \tag{3.4}$$

Z-dependence in Eq. 3.4 is Z^{-2}, which is the same as the usual lidar equation (Eq. 3.5).

$$P_r(Z) = C \frac{\sigma_{bk}}{Z^2} e^{-2\tau} \tag{3.5}$$

where C is the constant of the lidar instrument [3, 11]. σ_{bk} is the backscattering coefficient.

Z-dependence of this case is the same as that of sphere, however, size dependence G^2 is different from that of sphere (G^1).

Case for intermediate state

This subsection is the case when altitude is 80 $m < Z < 2$ km and rest is the same as in subsection **3.2.2**. In this case, it is easily expected that Z-dependence of $P_r(Z)$ has the value between -2 and 0, where the dependence might be changed as the altitude changes.

We estimate the relation between Z-dependence of $P_r(Z)$ and Z for a given size of particle and receiver are the same as those in subsection **3.2.2**. Fig. 3.3 (a) shows Z-dependence of the exponent of the received power, $dlog_{10}P_r(Z)/dlog_{10}Z$. When Z is about 200 m, received power becomes proportional to $Z^{-1.5}$. When altitude is less than 50 m, oscillation occurs, because of the single particle scattering. Fig. 3.3 (b) shows Z-dependence of the received power scattered by the rectangle and that by a sphere calculated by Eq. 3.6 [12] where we neglect the internally reflection of the sphere. The rectangle and the sphere have the same geometrical cross sections for the fair comparison.

$$P_{sp}(Z) = \frac{R_{sl}}{4\pi} G I_0 \frac{S_t}{Z^2} e^{-2\tau} \tag{3.6}$$

where S_t is the geometrical cross section of the receiver. At the altitude of 1000 m, received power produces about 2×10^6 times larger signals compared with that of spherical scattering.

3.2.3 Scattering by the rectangular particles randomly oriented in horizontal plane

For a rectangular target with orientational averaging where major axis of the rectangle is fixed along Y axis and is taken to be parallel to the horizontal plane and minor axis is taken to be along Z axis and rotated around Y axis randomly (2D-rectangle), scattered irradiance can be written as Eq. 3.7 by using Eq. 3.1.

$$
\begin{aligned}
I_S(x, y, Z) &= \frac{1}{\pi} \int_0^\pi I_s(x, y, Z, \Psi) d\Psi \\
&= \frac{G^2}{ka\lambda^2} \frac{R_{sl} I_0}{Z^2} (\frac{\sin \Phi_Y}{\Phi_Y})^2 e^{-2\tau}
\end{aligned}
\tag{3.7}
$$

Fig. 3.4 shows the horizontal distribution of backscattering from the target. The shape of the backscattering pattern can be understood from the superposition of that by the rectangular with a fixed orientation.

Received power becomes

$$
P_r(Z) = C' \int_{-R_t}^{R_t} dx \int_{-R_t}^{R_t} dy I_S(x, y, Z)
\tag{3.8}
$$

Case for low cloud

When the altitude of cloud is less than 80 m, and the size of rectangle is 200 $\mu m \times 100$ μm, Eq. 3.8 becomes

$$
P_r(Z) = C' \frac{1}{\pi} \frac{R_t}{Z} R_{sl} I_0 G e^{-2\tau}
\tag{3.9}
$$

This Z^{-1} dependence can be understood by the Z-dependence of cylindrical column [12] to be Z^{-1}.

Case for high cloud

When altitude is larger than 2 km and sizes of rectangle and receiver are the same as those in previous subsection, Eq. 3.7 becomes

$$
P_r(Z) = C' \frac{G^2}{ka\lambda^2} \frac{R_{sl} I_0}{Z^2} R_t^2 e^{-2\tau}
\tag{3.10}
$$

Z-dependence is the same as that in the usual lidar equation (Eq. 3.5). Contrary to the size-dependence in usual lidar equation ($\propto G$), that dependence in this case becomes G^2/a.

Case for intermediate state

Similar to the case for the fixed orientation, Z-dependence of received power should be changed by its distance like fixed orientational case. Figs. 3.5 (a) and (b) are the same as Figs. 3.3 (a) and (b) but for 2D-rectangle whose geometrical cross section is 200 $\mu m \times$ 100 μm. Fig. 3.5 (a) shows received power is proportional to $Z^{-1.5}$ when Z is about 200 m. When altitude is less than 50 m, oscillation also occurs. Fig. 3.5 (b) shows received power produces about 10^3 times larger signals compare with that of spherical scattering at the altitude 1000 m.

3.3 Scattering by hexagonal crystals

Particle's orientation might depend on its shape. Ono (1969) showed the particle is aligned as its longest axis is parallel to the horizontal plane. For example, when hexagonal column with aspect ratio $asp(\equiv l/2a) = 3$ is considered, symmetrical axis is parallel to the horizontal plane (2D-column). For hexagonal plate with $asp = 1/3$, symmetrical axis is perpendicular to the horizontal plane (2D-plate).

When the 2D-plate is considered, we assume the backscattered irradiance I_s for 2D-plate is the same as that for a rectangle with fixed orientation which has the same geometrical cross section for 2D-plate. That is, I_s is obtained by using Eq. 3.1 with $l = a = R_{sq}$, where R_{sq} is the side length of the square. The backscattered irradiance by 2D-column might be 3 times larger than that by 2D-rectangle whose geometrical cross section is the same as that of a rectangle on the hexagonal column.

Figs. 3.7 (a) and (b) are the same as Figs. 3.3 (a) and (b) but for 2D-plate and 2D-column. We assume the aspect ratios are 3 and 1/3, $I_0 = 1$ W/m^2, optical constant[9] is $1.31 + i2.54 \times 10^{-9}$, and ice water content (IWC) is 1 g/m^3. And log-normal distribution (Eq. 3.11) is assumed, where mode radius r_m is 100μm and standard deviation σ is 1.5. We neglect the attenuation for the signals ($\tau = 0$). For 2D-plate and 2D-column, $P_r(Z)$ is proportional to $Z^{-1.5}$ when Z is about 500 m. In addition, received power for 2D-plate produces about 10^7 times larger signals compared with that for a sphere with same size distribution at the altitude 1000 m. And that for 2D-column produces about 5×10^3 times larger signals compared with that for a sphere at $Z = 1000$ m.

Figs. 3.8 (a) and (b) are the same as Figs. 3.7 (a) and (b) but $r_m = 30\ \mu m$. For 2D-plate and 2D-column, $P_r(Z)$ is proportional to $Z^{-1.5}$ when Z is about 150 m. In addition, received power for 2D-plate produces about 8×10^5 times larger signals compared with that for a sphere at $Z = 1000\ m$. And that for 2D-column produces about 10^3 times larger signals compared with that for a sphere at $Z = 1000\ m$.

$$\frac{dn(r)}{dr} = \frac{1}{\sqrt{2\pi} r \ln \sigma} exp - \{\frac{\ln r - \ln r_m}{\sqrt{2} \ln \sigma}\}^2 \qquad (3.11)$$

3.4 Summary

We analyze lidar backscattering enhancement for pristine hexagonal ice crystals by using Fraunhofer diffraction based on Kirchhoff's diffraction theory (KD).

First we start with the backscattering by a rectangular target. Then we compute the scattering by hexagonal ice crystals by using the analogy of the rectangular calculations.

We calculate the scattering by hexagonal column and plate randomly oriented in horizontal plane. We assume that the aspect ratios to be 3 and 1/3 and size distribution is log-normal distribution, where mode radius r_m is 100 μm and standard deviation σ is 1.5. For 2D-plate and 2D-column, $P_r(Z)$ is proportional to $Z^{-1.5}$ when Z is about 500 m. In addition, received power for 2D-plate produces about 10^7 times larger signals compared with that for sphere at the altitude 1000 m. And that for 2D-column produces about 5×10^3 times larger signals compared with that for sphere at $Z = 1000\ m$.

For 2D-plate and 2D-column whose $r_m = 30\ \mu m$, $P_r(Z)$ is proportional to $Z^{-1.5}$ when Z is about 150 m. In addition, received power for 2D-plate produces about 8×10^5 times larger signals compared with that for sphere at $Z = 1000\ m$. And that for 2D-column produces about 10^3 times larger signals compared with that for sphere at $Z = 1000\ m$.

These results are not only important for the scattering by the pristine hexagonal ice crystals, but also applicable for the particles with flat surfaces except for the highly irregular shaped particles, such as Koch fractals [14].

In this paper, we consider the scattering by the hexagonal crystals perfectly oriented in horizontal plane. However, since it might be rare that the cloud particles stay in such orientation due to turbulence and might have tumbling. This might lead to drastically reduce

the backscattering enhancement. The effect of such tumbling is currently investigated by us.
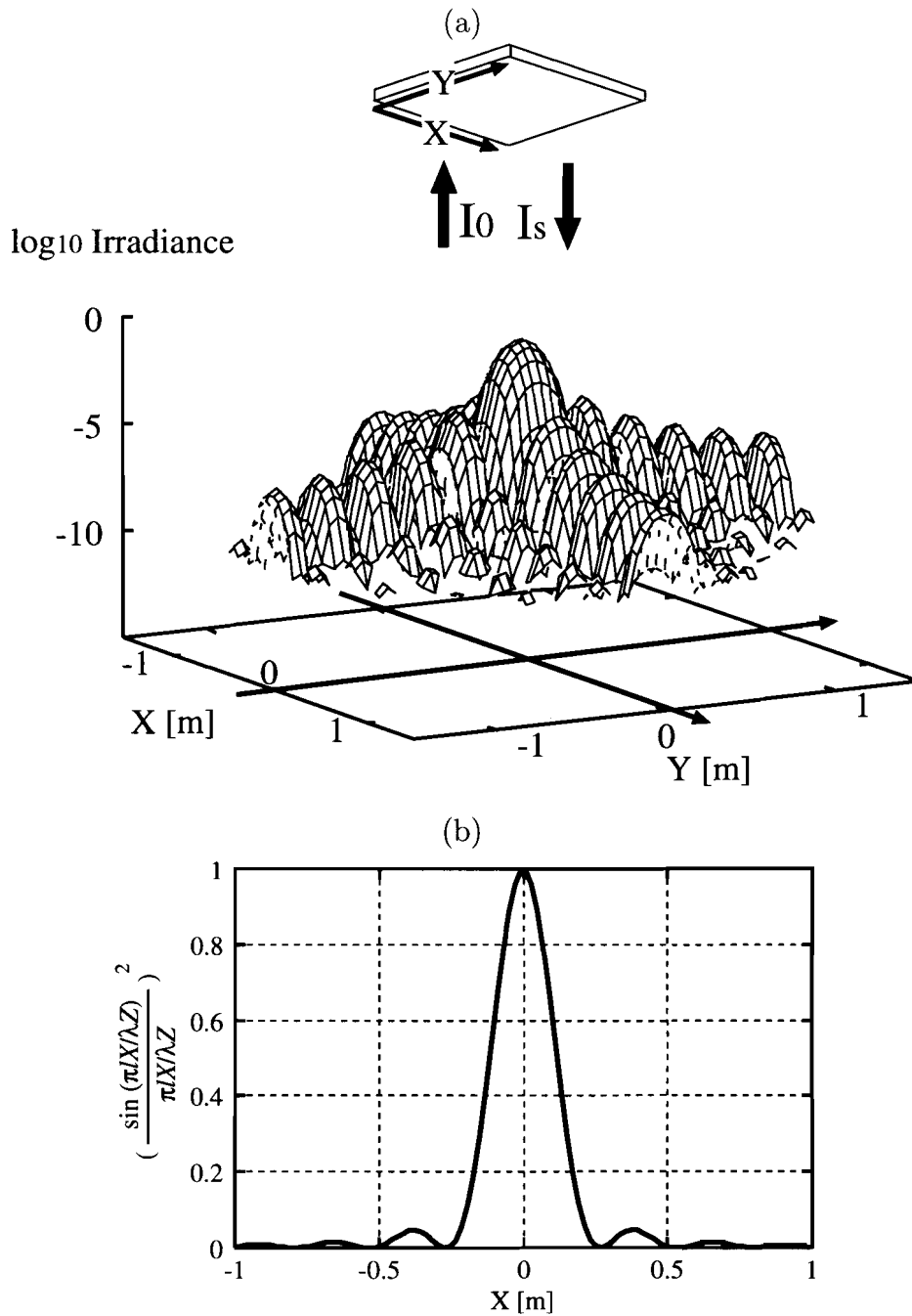
Figure 3.2: (a) The horizontal distributions of backscattering pattern by the rectangular target normalized at maximum when Ψ is 0, λ is 0.532 μm, l and a are 200 μm and Z is 100 m. (b) Slice of the backscattering profile of (a) at y=0.
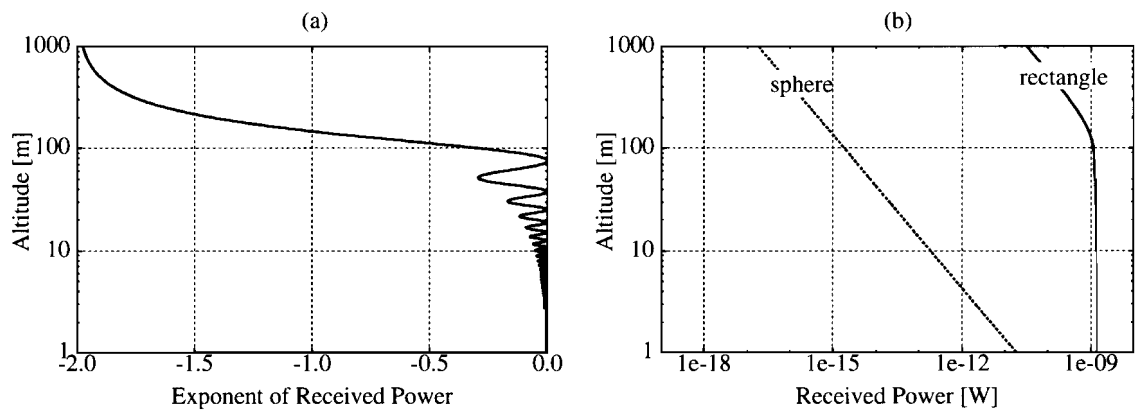
Figure 3.3: (a) Z-dependence of the exponent of the received power, $dlog_{10}P_r(Z)/dlog_{10}Z$. We assume that shape of a rectangle is 200 $\mu m \times$ 200 μm and R_t is 0.2 m. (b) Z-dependence of the received power scattered by the rectangle and a sphere. Both of them have same geometrical cross section. We neglect the internally reflection of the sphere.
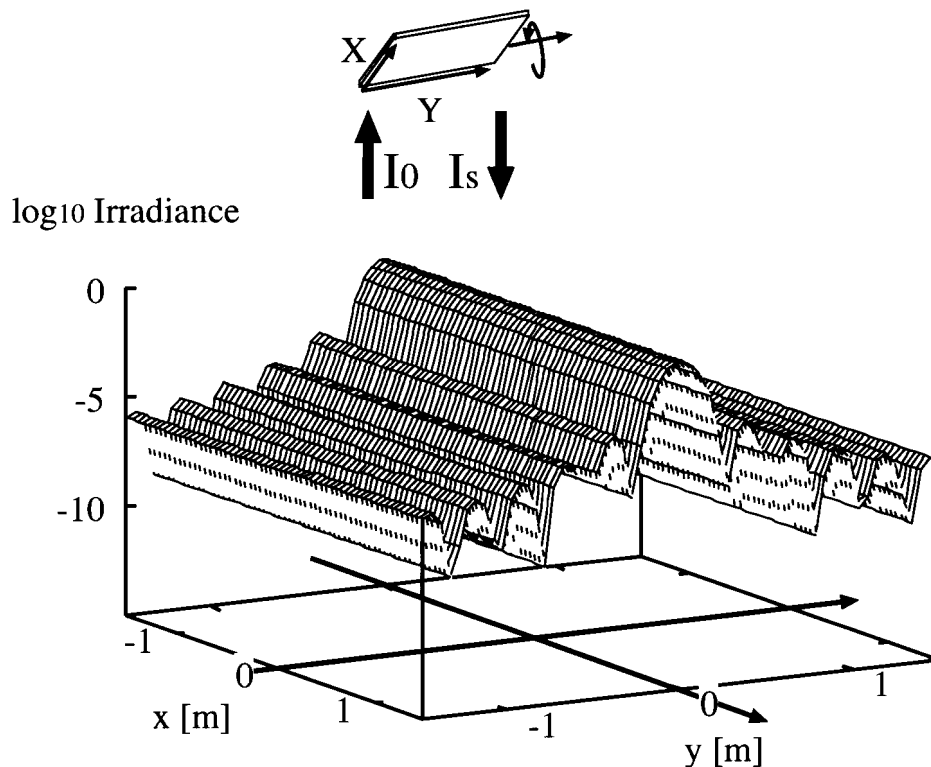

Figure 3.4: The same as Fig. 3.2 (a) but for the rectangular target with orientational averaging where major axis of the rectangle is parallel to the Y axis and minor axis is rotated randomly.
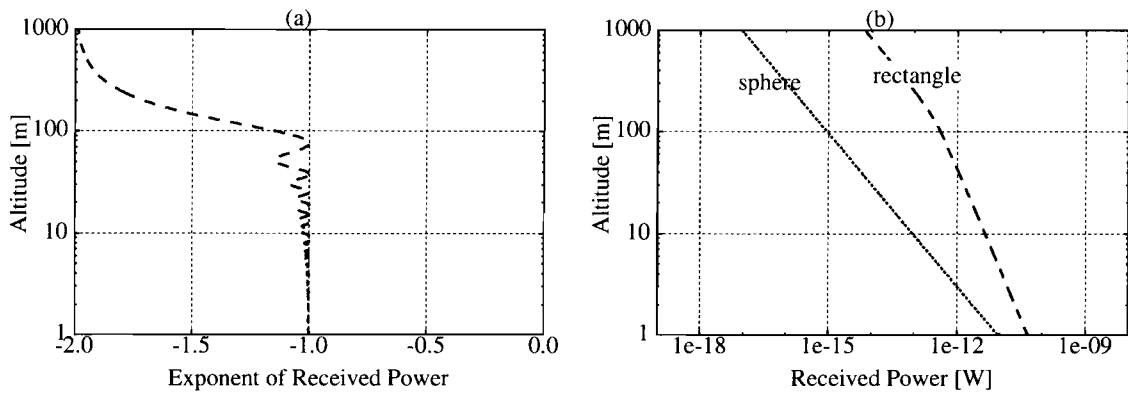
41

Figure 3.5: (a) and (b) are the same as Figs. 3.3 (a) and (b) but for 2D-rectangle whose size is 200 μm × 100 μm.
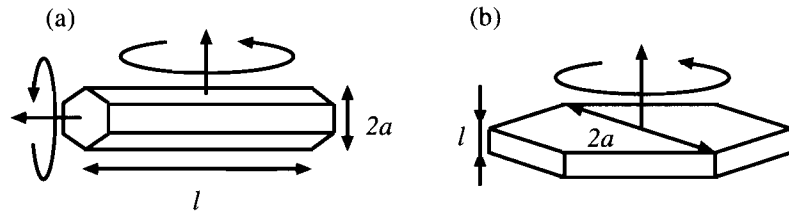

Figure 3.6: Alignment of a hexagonal crystal. (a) symmetrical axis is parallel to the horizontal plane (2D-column) and (b) symmetrical axis is perpendicular to the horizontal plane (2D-plate).
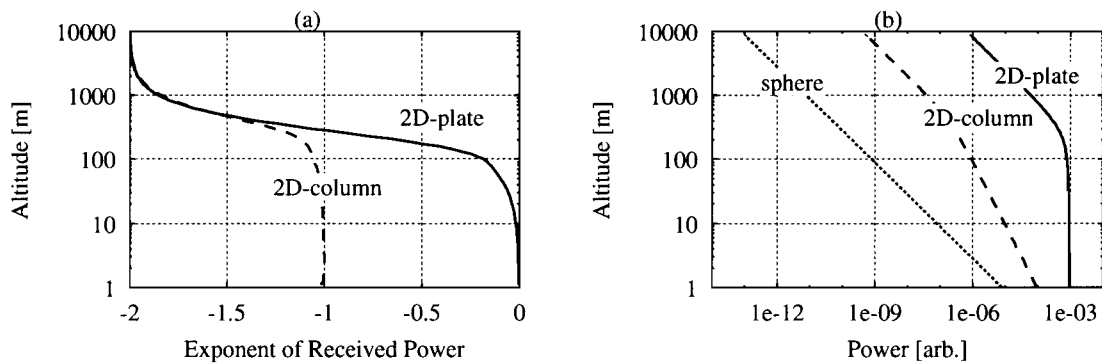

Figure 3.7: (a) and (b) are the same as Figs. 3.3 (a) and (b) but for 2D-plate and 2D-column. We assume the aspect ratios are 3 and 1/3 and size distribution is log-normal distribution where mode radius is 100μm and standard deviation is 1.5.
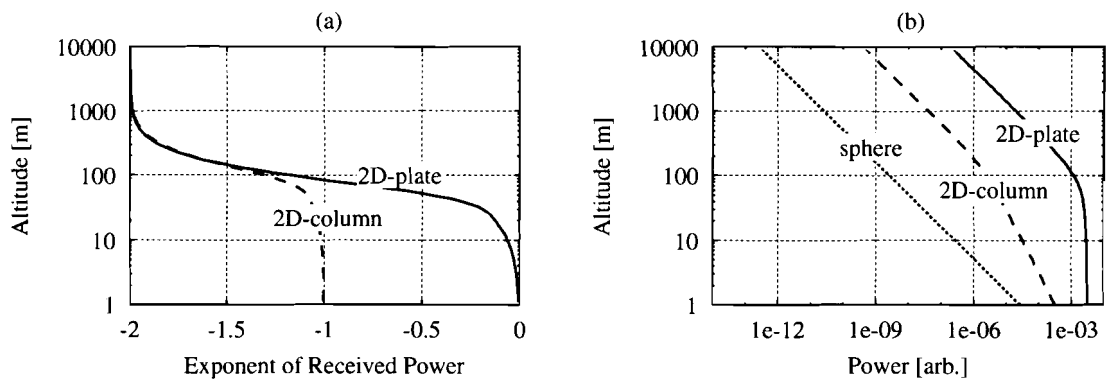
42

Figure 3.8: (a) and (b) are the same as Figs. 3.7 (a) and (b) but $r_m = 30$ μm.

43

Bibliography

[1] C. M. Platt, "Lidar backscatter from horizontal ice crystal plates," J. Appl. Meteorol. **17**, 482-488 (1978).

[2] C. M. Platt, N. L. Abshire, and G. T. McNice, "Some microphysical properties of an ice cloud from lidar observation of horizontally oriented crystals," J. Appl. Meteorol. **17**, 1220-1224 (1978).

[3] F. G. Fernald, B. M. Herman, and J. A. Reagan, "Determination of Aerosol Height Distributions by Lidar," J. Appl. Meteor., **11**, 482-489 (1972).

[4] J. D. Klett, "Stable analytical inversion solution for processing lidar returns," Appl. Opt. **20**, 211-220 (1981).

[5] M. I. Mishchenko, D. J. Wielaard, and B. E. Calson, "T-matrix computations of zenith-enhanced lidar backscatter from horizontally oriented ice plates," Geophys. Res. Lett., **24**, 771-774, (1997).

[6] S. Iwasaki, and H. Okamoto, "Anomalous backscattering enhancement by non-spherical ice crystals for lidar observation," Appl. Opt., in submission.

[7] M. Born and E. Wolf, *Principles of Optics,* (PERGAMON PRESS, Oxford, 1975).

[8] Jackson, J.D., *Classical Electrodynamics,* (Wiley, New York., 1983).

[9] S. G. Warren, "Optical constants of ice from the ultraviolet to the microwave," Appl. Opt. **23**, 1206-1225 (1984).

[10] F. G. Fernald, "Analysis of atmospheric lidar observations: some comments," Appl. Opt. **23**, 652-653 (1984).

[11] G. L. Stephanes, *Remote Sensing of the Lower Atmosphere,* (New York, Oxford., 1994), pp. 427-438.

[12] C. F. Bohren and D. R. Huffman, *Absorption and Scattering of Light by Small Particles,* (Wiley, New York., 1983)

[13] A. Ono, "The Shape and Riming Properties of Ice Crystals in Natural Clouds," J. Atmos. Sci.,**26**, 138-147 (1969).

[14] A. Macke, J. Mueller, and E. Raschke, "Single Scattering Properties of Atmospheric Ice Crystals," J. Atmos. Sci., **53**, 2813-2825 (1996).

Chapter 4

Analysis of lidar returns from rectangles and hexagonal ice crystals

Abstract

There is a theoretical problem to apply geometrical optics for the backscattering calculations of ice cloud particles. In order to know the backscattering by pristine hexagonal ice crystals, we calculate the scattering for a rectangular particle by using Fraunhofer diffraction based on Kirchhoff's diffraction theory (KD). Then we compute the backscattering by hexagonal plates and columns perfectly oriented in horizontal plane (2D-plate and 2D-column). We show that the received power for the 2D-plates produces $10^4 \sim 10^9$ times larger signals compared with that for spheres with same size distribution at the altitude 10000 m. And that for 2D-columns produces $5 \times 10^2 \sim 3 \times 10^4$ times larger signals compared with that for spheres at $Z = 10000$ m. This might explain the unusual large lidar returns reported by Platt *et. al.* (1978)[1].

4.1 Introduction

Lidar is one of the promising tools to investigate the cloud profiles such as vertical structure, shapes and sizes of ice crystals, which are the unknown factors to correctly estimate the radiative properties of clouds. In order to retrieve above information of size from the lidar observation [2], we need to know the backscattering cross section of the cloud particles. It is well known that geometrical optics (GO) is one of the most effective method to calculate the scattering properties by the ice crystals for the lidar wavelength. However, there is a theoretical problem to apply GO for the backscattering calculations of ice cloud particles. We tested GO and it turned out that GO is only applicable for the case

46

the altitude is very close to the ground (*e.g.* 100 *m*) and showed the need of modifications to the lidar equation. On the other hands, Mishchenko *et. al.* (1997) [3] considered disks and spheroids with size parameters up to 50 as ice crystals and calculated lidar backscattering from these particles by using T-matrix method. Since T-matrix method can not apply to the larger size parameters, we develop the method that uses Fraunhofer diffraction based on Kirchhoff's diffraction theory (KD).

In section **2.1** and **2.2**, we calculate the scattering by a rectangular particle for simplicity. In section **2.3** we compute the scattering by hexagonal columns and plates randomly oriented in horizontal plane by using the analogy of the rectangular calculations.
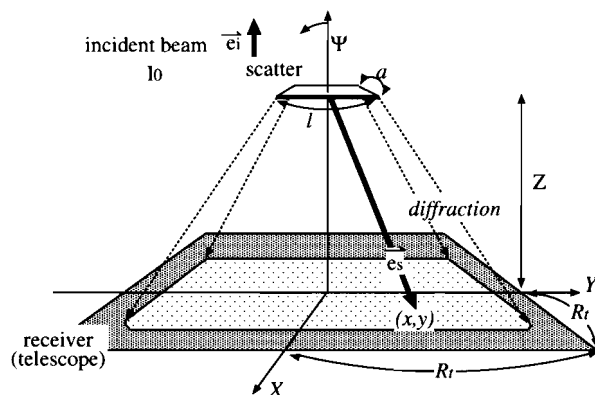
4.2 Scattering model

Figure 4.1: The geometry of the lidar observation. A particle is located at the altitude Z. Length of the rectangle is specified by l and a ($l \geq a$), respectively. $\vec{e_i}$ and $\vec{e_s}$ denote the incident and scattered directions.

For simplicity, we start with a rectangular particle as the non-spherical particle and we assume the shape of a receiver is also rectangle. To calculate a backscattered pattern, we use Fraunhofer diffraction based on Kirchhoff's diffraction theory (KD). The backscattering irradiance for a rectangle is written by Eq. 4.1 where its major axis is parallel to the Y axis and minor axis is fixed in some direction [4].

$$I_s(X, Y, Z, \Psi) = \frac{G^2}{\lambda^2} \frac{R_{sl} I_0}{Z^2} \left(\frac{\sin \Phi_X}{\Phi_X}\right)^2 \left(\frac{\sin \Phi_Y}{\Phi_Y}\right)^2 e^{-2\tau}$$

$$\Phi_X = kl(x/Z - 2\sin \Psi)/2$$

$$\Phi_Y = kay/2Z, \tag{4.1}$$

where G denotes geometrical cross section of the rectangle, R_{sl} is the reflectance of the slab with some thickness and it is calculated by geometrical optics (GO) (*e.g.* Born and Wolf 1975). I_0 is incident intensity. λ and k are wavelength and wave number of interest. Ψ denotes the angle between the normal vector of the rectangle and the incident beam and τ is the optical depth. l and a ($l \geq a$) are the side lengths of the rectangle (see Fig. 4.1).

4.2.1 Scattering by a rectangular particle with a fixed orientation

For a rectangular particle with a fixed orientation at $\Psi = 0$, backscattered power into the receiver is formulated by

$$P_r(Z) = C' \int_{-R_t}^{R_t} dx \int_{-R_t}^{R_t} dy I_s(x, y, Z, \Psi), \tag{4.2}$$

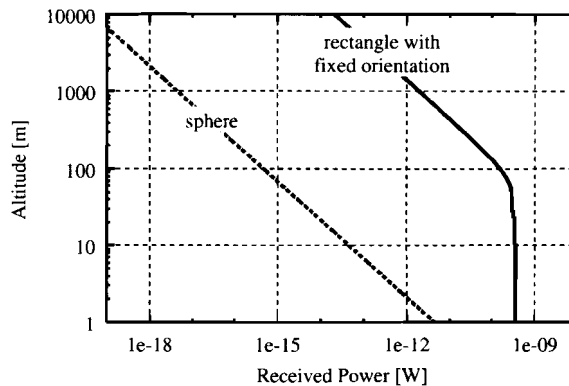where R_t is the half width of receiver and C' is the constant for the lidar instruments.

Figure 4.2: Z-dependence of the received power scattered by the rectangle and a sphere. We neglect the internally reflection of the sphere. The rectangle and the sphere have same geometrical cross sections.

Fig. 4.2 shows Z-dependence of $P_r(Z)$ for a rectangle with a fixed orientation and that for a sphere where we neglect the internally reflection of the sphere. The rectangle and the sphere have the same geometrical cross sections for the fair comparison. We assume that the shape of a rectangle is 100 μm × 100 μm, $R_t = 0.2$ m, $\lambda = 0.532$ μm, $I_0 = 1$ W/m^2, $C' = 1$ and optical constant is $1.31 + i2.54 \times 10^{-9}$. And we neglect the attenuation for the signals ($\tau = 0$). At the altitude of 1000 m, received power produces about 5×10^5 times larger signals compared with that for the sphere.
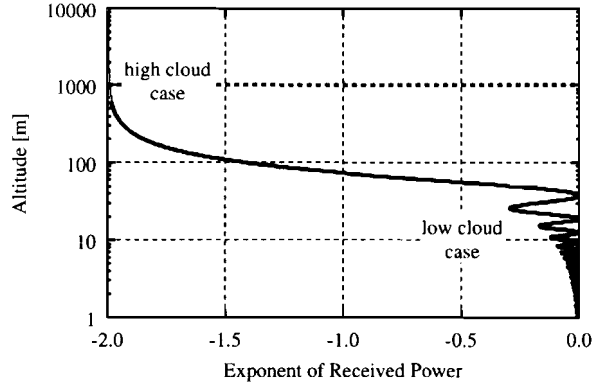
48

Figure 4.3: Z-dependence of the exponent of the received power, $dlog_{10}P_r(Z)/dlog_{10}Z$.

Fig. 4.3 shows Z-dependence of the exponent of the received power, $dlog_{10}P(Z)/dlog_{10}Z$. When Z is small, most backscattered power is received (see Fig. 4.4). Its received power is derived by substitution of Eq. 4.1 into Eq. 4.2,

$$P_r(Z) = C'R_{sl}I_0G. \tag{4.3}$$

It turns out that $P_r(Z)$ does not depend on Z, contrary to the dependence Z^{-2} in the usual lidar equation (Eq. 4.4).

$$P_r(Z) = C\frac{\sigma_{bk}}{Z^2}e^{-2\tau}, \tag{4.4}$$

where C is the constant of the lidar system [2]. σ_{bk} is the backscattering coefficient.

When Z is large, received power is derived by

$$P_r(Z) = C'\frac{G^2}{\lambda^2}\frac{S_t}{Z^2}R_{sl}I_0e^{-2\tau}, \tag{4.5}$$

where S_t is the area of the receiver, $(2R_t)^2$. It turns out that Z-dependence is as same as that in the usual lidar equation, however, size dependence G^2 appeared in Eq. 4.5 is different from G in the usual lidar equation. The exponent drastically changes from 0 at $Z = 50$ m to -2 at $Z = 500$ m.

4.2.2 Scattering by a rectangle randomly oriented in horizontal plane

For a rectangular target randomly oriented in horizontal plane (2D-rectangle), the backscattered irradiance becomes

$$I_S(x, y, Z) = \frac{1}{\pi}\int_0^\pi I_s(x, y, Z, \Psi)d\Psi$$
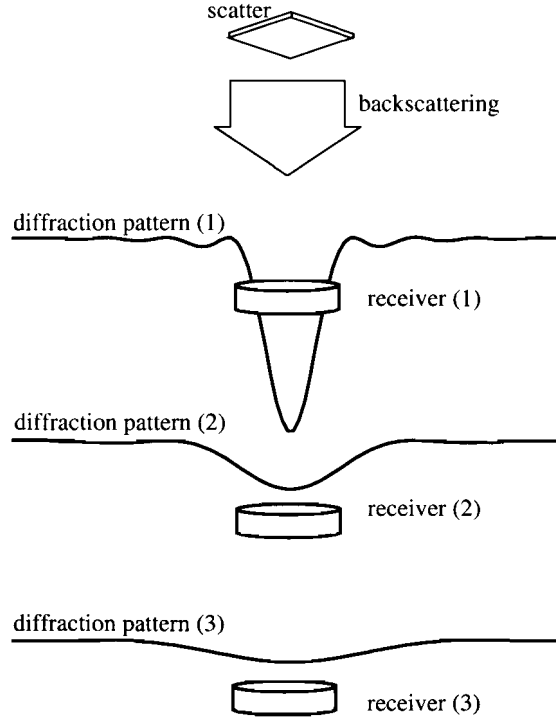
49

Figure 4.4: The sketch of the relation between backscattering irradiance, receiver and altitude.

$$= \frac{G^2}{ka\lambda^2} \frac{R_{sl}I_0}{Z^2} \left(\frac{\sin \Phi_Y}{\Phi_Y}\right)^2 e^{-2\tau}. \tag{4.6}$$

For a 2D-rectangle, received power is formulated by

$$P_r(Z) = C' \int_{-R_t}^{R_t} dx \int_{-R_t}^{R_t} dy I_S(x, y, Z). \tag{4.7}$$

Here 2D-rectangle with geometrical cross section of 100 μm × 100 μm is considered. Fig. 4.5 is the same as Fig. 4.2 but for 2D-rectangle. Fig. 4.5 shows received power produces about 2×10^2 times larger signals compare with that of spherical scattering at the altitude 1000 m.

Similar to the case for the fixed orientation, Z-dependence of received power should be changed by its distance. $P_r(Z)$ is proportional to $Z^{-1.5}$ when Z is about 80 m.

When Z is small, received power is derived by substitution of Eq. 4.6 into Eq. 4.7,

$$P_r(Z) = C' \frac{1}{\pi} \frac{R_t}{Z} R_{sl} I_0 G. \tag{4.8}$$

This can be understood that $P_r(Z)$ is proportional to Z^{-1}, contrary to the spherical particles. In these region, GO is applicable and the dependence is Z^{-1} as Eq. 4.8.
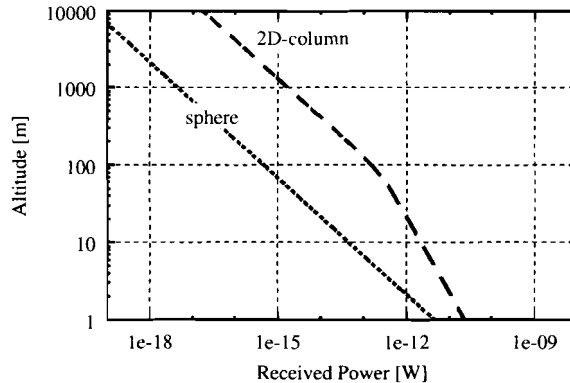
50

Figure 4.5: The same as Fig. 4.2 but for 2D-rectangle whose geometrical cross section is 100 μm × 100 μm.

When Z is large, Z-dependence for this case becomes Z^{-2}, which is the same dependence for the sphere. This can be understood by the following explanation. The distance between the particle and the receiver is large enough so that the horizontal distribution of the backscattered power is homogeneous over the receiver, which is the same as that for the scattering wave by the sphere.

4.2.3 Distance dependence of the received power by hexagonal crystals

When the hexagonal plate with an aspect ratio of 1/3 randomly oriented in horizontal plane (2D-plate) is considered, we assume its backscattered irradiance I_s is the same as that for the square with a fixed orientation which has the same geometrical cross section of 2D-plate.

When the hexagonal column with an aspect ratio of 3 randomly oriented in horizontal plane (2D-column) is considered, we assume its backscattered irradiance I_s is given by the superposition of the backscattered wave from every surface where the backscattering signals from a surface of hexagonal column is estimated by the similar procedure described in section **2.2**.

We assume that ice water content (IWC) is 1 g/m^3, and size distribution is log-normal distribution where mode radiuses r_m are 10, 100, 1000 μm and standard deviation σ is 1.5.

Fig. 4.7 (a) shows that received power for 2D-plate produces $10^4 \sim 10^9$ times larger signals compared with that for spheres with same size distribution at the altitude 10000 m. And that for 2D-column produces $5 \times 10^2 \sim 3 \times 10^4$ times larger signals compared with
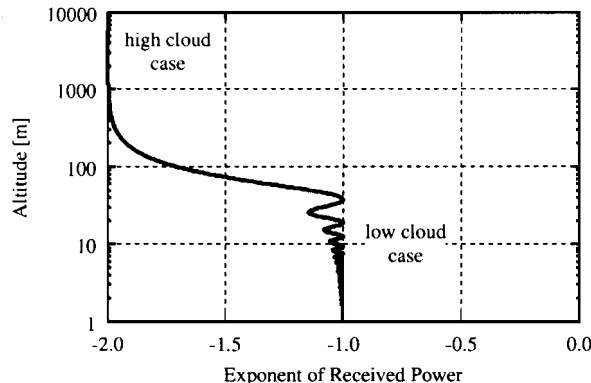
51

Figure 4.6: The same as Fig. 4.3 but for 2D-rectangle whose geometrical cross section is 100 μm × 100 μm.

that for spheres at $Z = 10000$ m. Fig. 4.7(b) is the same as Fig. 4.3 but for 2D-plate and 2D-column.

4.3 Summary

We analyze lidar backscattering enhancement for pristine hexagonal ice crystals by using Fraunhofer diffraction based on Kirchhoff's diffraction theory (KD).

At first, we calculate the scattering by a rectangular particle for simplicity. Then we compute the scattering by hexagonal columns and plates randomly oriented in horizontal plane (2D-plate and 2D-column) by using the analogy of the rectangular calculations.

It turns out that the received power for 2D-plate produces $10^4 \sim 10^9$ times larger signals compared with that for spheres with same size distribution at the altitude 10000 m. And that for 2D-column produces $5 \times 10^2 \sim 3 \times 10^4$ times larger signals compared with that for a sphere at $Z = 10000$ m.

Our theoretical calculations show the existence of the hexagonal particles randomly oriented in horizontal plane might be explained for the unusual large lidar returns reported by Platt et. al. (1978).

In this paper, we consider the scattering by the hexagonal crystals perfectly oriented in horizontal plane. However, since it might be rare that the cloud particles stay in such orientation due to turbulence and might have tumbling. This might lead to drastically reduce the backscattering enhancement. The effect of such tumbling is currently investigated by us.
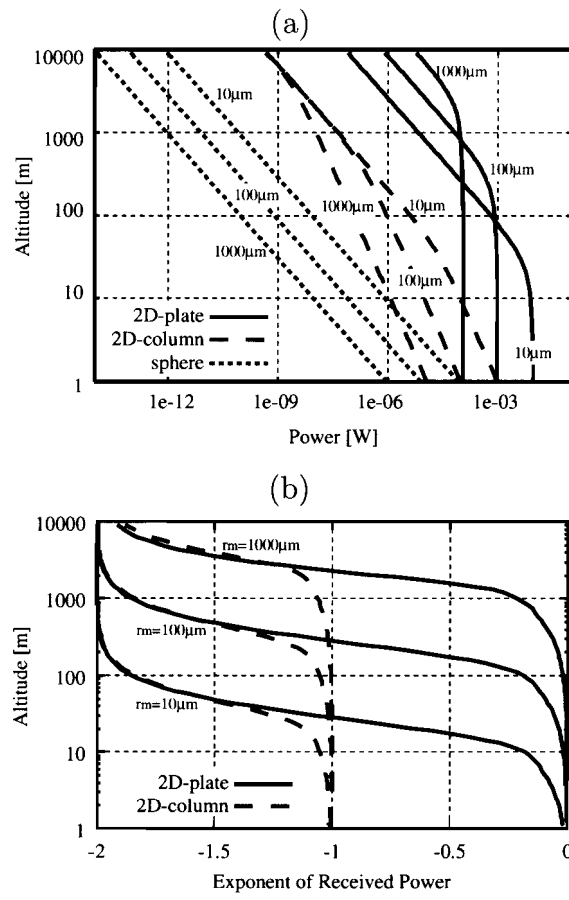
52

Figure 4.7: (a) and (b) are the same as Fig. 4.2 and Fig. 4.3 but for 2D-plate and 2D-column.

53

Bibliography

[1] Platt, C. M., N. L. Abshire, and G. T. McNice, 1978: Some microphysical properties of an ice cloud from lidar observation of horizontally oriented crystals, J. Appl. Meteorol. **17**, 1220-1224.

[2] Fernald, F. G., 1984: Analysis of atmospheric lidar observations: some comments, Appl. Opt., **23**, 652-653.

[3] Mishchenko, M. I., D. J. Wielaard, and B. E. Calson, 1997: T-matrix computations of zenith-enhanced lidar backscatter from horizontally oriented ice plates, Geophys. Res. Lett., **24**, 771-774.

[4] Born, M. and E. Wolf, 1975: *Principles of Optics*, PERGAMON PRESS, Oxford.

Chapter 5

Cloud observation by lidar, 95GHz cloud profiling radar and 13.8GHz precipitation radar

Abstract

We report synergy cloud observations by lidar, 95GHz cloud radar and 13.8GHz precipitation radar in 2000. Our experiments show these synergy observations have a great potential to retrieve micro-physical properties of cloud. For example, lidar and 95GHz cloud radar observations, Okamoto *et.al.* (2000) succeeded in retrieving effective radii of cloud particles and ice water content (IWC). The radar reflection of clouds with precipitation by 95GHz cloud radar turns to be different from that by 13.8GHz precipitation radar. This differences attribute to the different scattering signatures in both wavelengths, that is, backscattering of particles larger than $100\mu m$ is beyond Rayleigh scattering region, while, that for 13.8GHz is still within Rayleigh region. We conclude that these two radar is ideal tool for large particle sizing.

5.1 Introduction

Received power by radar and lidar depends on the several micro-physical properties of scatters, *i.e.*, size, number concentration, shape and alignment of cloud particles. However, there have been only few synergy experiments by using these instruments. In order to retrieve these micro-physics, synergy observations are effective. For example, Okamoto *et.al.* (2000) [1, 2] succeeded in development of the method to retrieve effective radii of

cloud particles and ice water content (IWC) by using the 95GHz cloud radar and lidar. Thus we had many synergy ground-based observations by lidar, 95GHz and 13.8GHz radar in February, October, November and December, 2000. In section **5.2**, we introduce our lidar, 95GHz cloud radar and 13.8GHz precipitation radar systems. In section **5.3**, we show the results of the cirrus observation by using lidar and 95GHz cloud radar called SPIDER (Special Polarimetric Ice Detection and Explication Radar) [3]. Optical depth of cirrus is thin but cirrus clouds cover about 20% of the globe on average [4]. Thus to understand cirrus is important to calculate the radiative forcing for the atmosphere. In section **5.4**, we show the results of melting layers in the clouds by SPIDER and 13.8GHz precipitation radar called CAMPR (CRL Airborne Multiparameter Precipitation Radar) [5]. Melting layers have very strong radar echo for CAMPR, that has been known as bright band, while, those are weak for SPIDER.

5.2 Description of our lidar, 95GHz cloud radar and 13.8GHz precipitation radar system
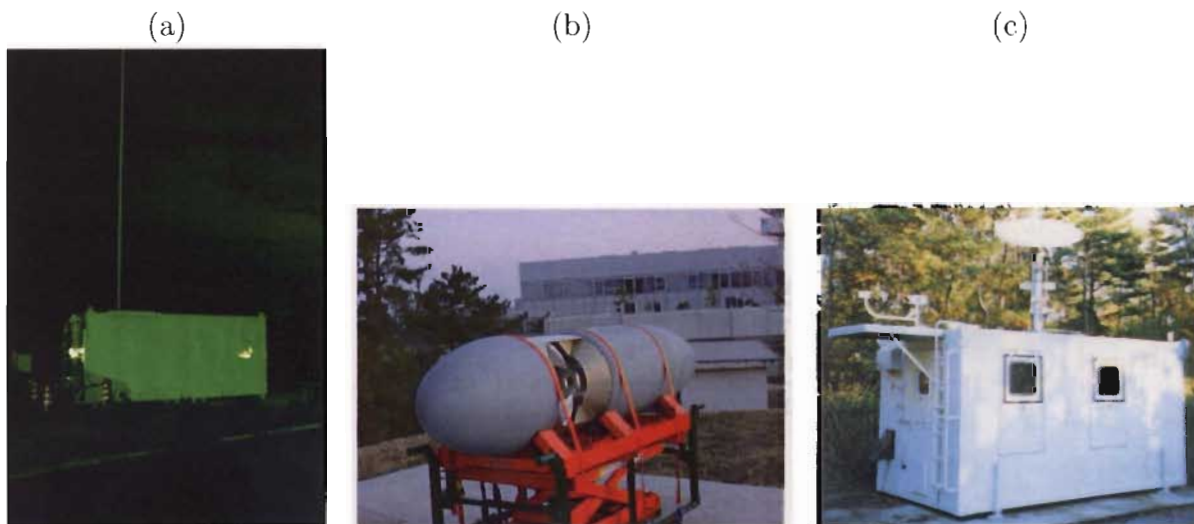
(a) (b) (c)

Figure 5.1: (a) Night view of the lidar observation. Green light is the laser pulses transmitted in every 0.05 sec. (b) The 95GHz cloud radar called SPIDER installed in the radar pod on the trestle. (c) The 13.8GHz precipitation radar called CAMPR-G. The antenna is set on the roof of white operation room.

Fig. 5.1 (a) is the night view of the lidar observation. Green light is the laser pulses transmitted in every 0.05 sec. The lidar has two wavelengths and dual polarization

56

Table 5.1: Specifications of lidar, SPIDER and CAMPR. The values with index * denote parameters and are typical values for usual observations.

	lidar	SPIDER	CAMPR
Wave length (frequency)	532nm (564THz) 1064nm (281.8THz)	3.154mm (95.04GHz)	2.17cm (13.8GHz)
Pulse Reputation Frequency	20Hz*	700Hz*	2kHz*
Transmitted power	8W	1kW	3kW
Vertical resolution	15m* (oscilloscope) 96m* (photon counter)	82.5m*	150m*
Pulse width	6-7ns	$1.1\mu s$*	$2\mu s$*
Doppler capability	×	○	○
Polarization function	dual	dual	dual

function. Fig. 5.1 (b) is the 95GHz cloud radar called SPIDER (Special Polarimetric Ice Detection and Explication Radar). SPIDER system has dual polarization function and Doppler capability. Fig. 5.1 (c) is the 13.8GHz precipitation radar for ground-based observation called CAMPR-G (CRL Airborne Multiparameter Precipitation Radar). CAMPR system also has dual polarization function and Doppler capability. SPIDER and lidar are co-located and CAMPR is set about 500m far from these two systems. Table 5.1 is the specifications of our lidar, SPIDER and CAMPR systems.

Eqs.5.1 are the definition of backscattering coefficient β and equivalent radar reflectivity factor Z_e. Those values are often used for the results of lidar and radar observation respectively.

$$\beta = \int_{size} dr \frac{dn(r)}{dr} \frac{\sigma_{cl}}{4\pi}$$

$$Z_e(mm^6/m^3) = \frac{\lambda^4}{\pi^5 K^2} \int_{size} dr \frac{dn(r)}{dr} \sigma_{cl}$$

$$K = |\frac{m_{ref}^2 - 1}{m_{ref}^2 + 2}| \qquad (5.1)$$

where σ_{cl} denotes backscattering cross section of a scatter. r is the size of scatter and $dn(r)/dr$ denotes size distribution. m_{ref} is the complex reflective index of scatter and K is 0.83 for liquid water [6] and 0.42 for water ice [7]. Z_e is often expressed in decibel units dBZ where $dBZ \equiv 10log_{10}Z(mm^6/m^3)$.

5.3 Cirrus clouds observed by lidar and 95GHz cloud radar

Figs. 5.2 (a) and (b) are the results of the synergy observation by SPIDER and lidar respectively from 12:21 to 13:30 (JST) at Kashima city on 31 October 2000. Generally, the cloud boundary detected by SPIDER agrees well with those by lidar. However, there are some differences. For example, there are two cloud layers for lidar but one for SPIDER before 13 o'clock at a height of 11km. And only lidar detects an aerosol layer at a height of 4km.
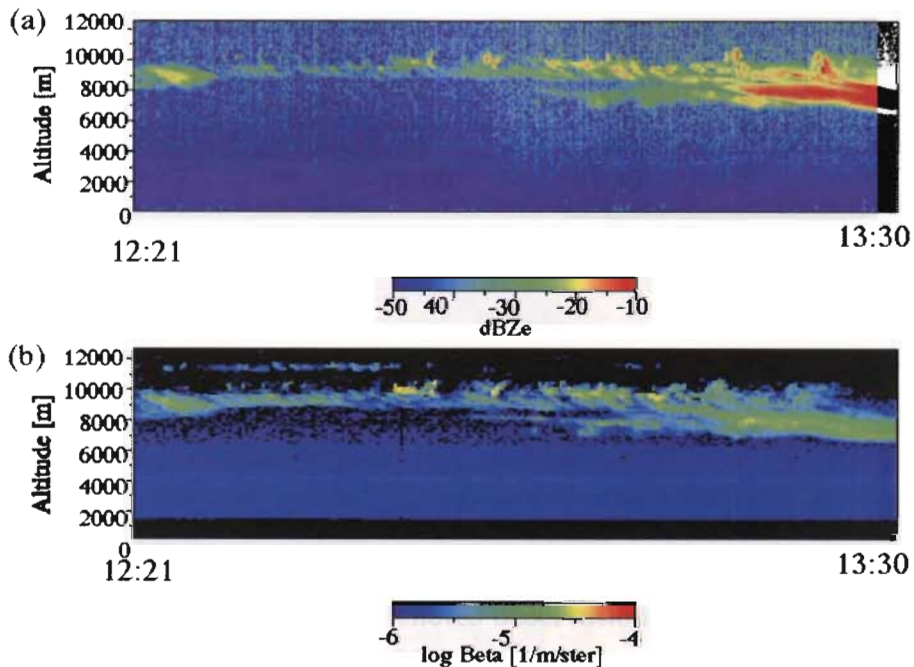

Figure 5.2: Results of the synergy observation of clouds by SPIDER and lidar from 12:21 to 13:30 (JST) at Kashima city on 31, October in 2000. Horizontal axis denotes observation time and vertical axis denotes altitude. (a) Equivalent radar reflectivity factor [dBZe] obtained by SPIDER. (b) Backscattering coefficient β detected by the lidar. Wavelength is 532nm. The lidar signal is expressed in the unit of $\log_{10}(\beta$ [1/m/str]).

Okamoto *et.al.* (2000) [1, 2] succeeded in development of the method to retrieve effective radius of cloud particles and ice water content (IWC) by using 95GHz cloud radar and lidar. The key of their method is to calculate the different size dependence of backscattering cross section between 95GHz cloud radar and lidar. Fig. 5.3 is their

retrieved results and it shows that the lower part of cloud consists of larger cloud particles. It is well known that larger particles tend to exist at lower part of cloud due to growth process. Thus their method shows the space-borne cloud radar and lidar are promising combination to retrieve the vertical distribution of cloud micro-physics.
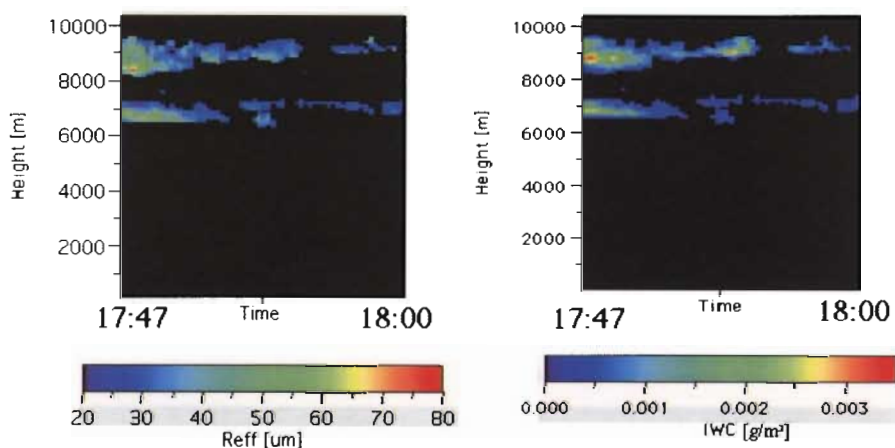

Figure 5.3: Effective radius (left panel) and ice water content (right panel) retrieved by synergy observation of lidar and SPIDER from 17:47 to 18:00 (JST) at Kashima city on February 28th, 2000. Horizontal axis denotes observation time and vertical axis denotes altitude (figures from Okamoto *et.al.* 2000).

5.4 Clouds and precipitation observed by 95GHz and 13.8GHz radars

Figs. 5.4 (a) and (b) are the results of the synergy ground-based observation by SPI-DER and CAMPER respectively from 15:53 to 17:08 (JST) at Kashima city on November 2nd, 2000. In Fig. 5.4 (b), there are very strong radar echo at a height of about 5km. This "bright band" is known to be "melting layer" that consists of melted and coalesced ice crystals [8, 9]. However, those are weak for SPIDER. This should be the reflection of complex nature of cloud micro-physics, *e.g.* the dielectric constants for mixture of ice and

water size of melting layer particles, etc. Thus the combination of these radars seems to be a powerful tool for the study of cloud with precipitation.
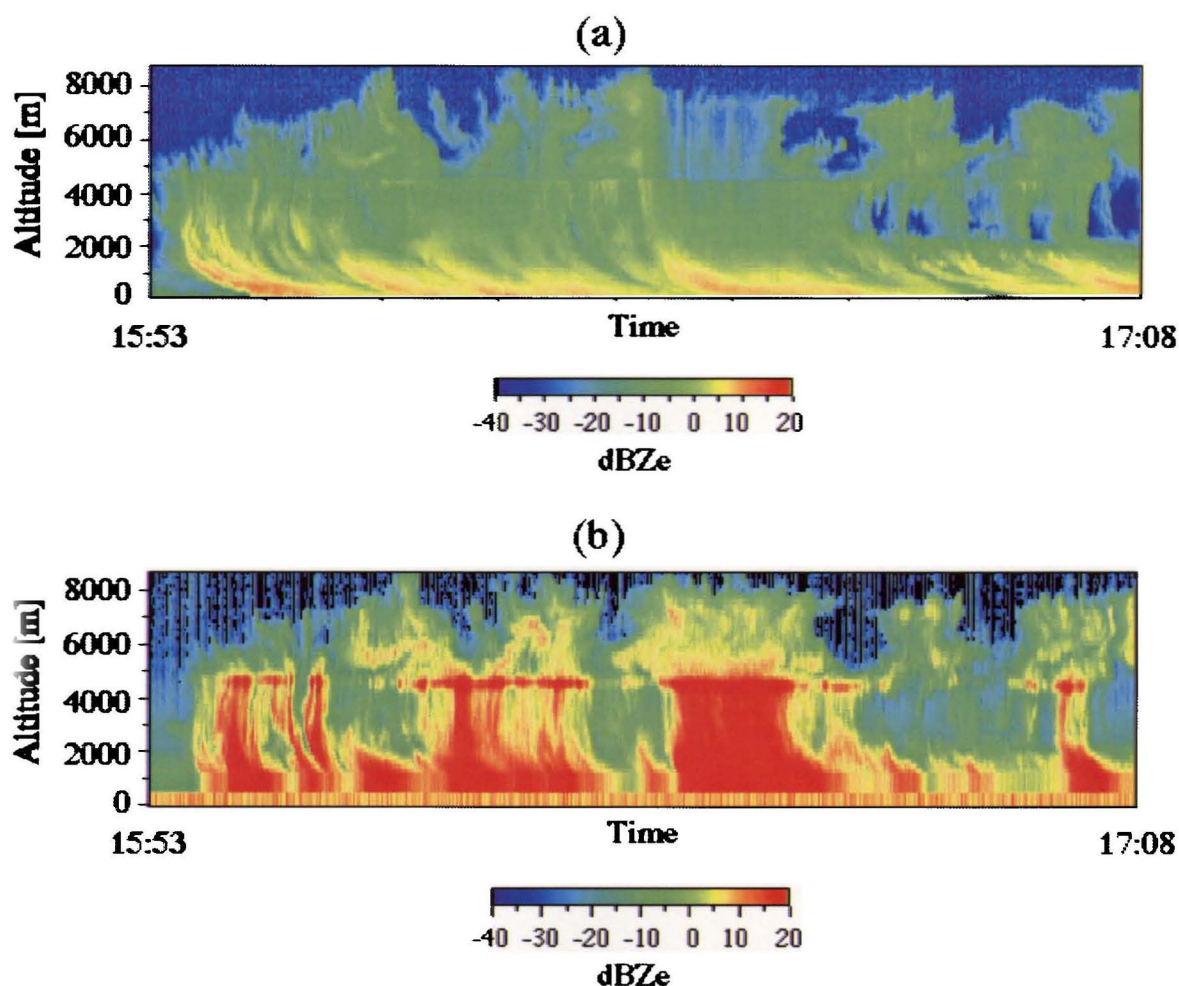
(a)

(b)

Figure 5.4: Results of the synergy ground-based observation of clouds and rainfall by SPIDER (95GHz) and CAMPER (13.8GHz) respectively from 15:53 to 17:08 (JST) at Kashima city on November 2nd, 2000. Horizontal axis denotes observation time and vertical axis denotes altitude.

5.5   Summary

We had intensive synergy ground-based observations by lidar, 95GHz cloud radar and 13.8GHz precipitation radar in February, October, November and December, 2000. Our

experiments show these synergy observations have a great potential to retrieve microphysical properties of cloud particles. Currently we are intensively analyzing those observation, and we will report retrieved results in the near future.

Bibliography

[1] Okamoto, H. , M.Yasui, H.Horie, H.Kuroiwa, H.Kumagai, and S.Iwasaki, "OB-SERVATION OF CLOUDS BY 95GHZ RADAR AND LIDAR SYSTEMS:RADIUS VERSUS FALL VELOCITY", Smith and Timofeyev (Eds.) IRS2000: Current Problems in Atmospheric Radiation, Deepak Publishing, 2000., submitted.

[2] Okamoto, H., S. Iwasaki, M. Yasui, H. Horie, H. Kuroiwa, and H. Kumagai, "95-GHz cloud radar and lidar systems:preliminary results of cloud micro-physics", In Wilheit, Masuko, and Wakabayashi (Eds) SPIE2000: Remote Sensing of the Atmosphere, Environment, and Space., 2000., submitted.

[3] H. Horie, T. Iguchi, H. Hanado, H. Kuroiwa, H. Okamoto, and H. Kumagai, "Development of a 95-GHz Airborne Cloud Profiling Radar (SPIDER)", IEICE Trans. Commun., 2000, in press.

[4] Wu, T., R. Cotton, and W. Y. Y. Cheng, "Radiative effects on the Diffusional Growth of Ice Particles in Cirrus Clouds", J. Atmos. Sci., **57**, 2892-2904 (2000).

[5] Kumagai, H., K. Nakamura, H. Hanado, K. Okamoto, N. Hosaka, N. Miyano, T. Kozu, N. Takahashi, T. Iguchi, and H. Miyauchi, "CRL Airborne Multiparameter Precipitation Radar (CAMPR): System Description and Preliminary Results", IEICE Trans. Commun., **E79-B**, 770-778 (1996).

[6] Ulaby, F. T., R. K. Moore, and A. K. Fung, *MICROWAVE REMOTE SENSING ACTIVE AND PASSIVE, volume III, From Theory to Applications*, (Artech house, Inc., 1986).

[7] S. G. Warren, "Optical constants of ice from the ultraviolet to the microwave," Appl. Opt. **23**, 1206-1225 (1984).

[8] Stephanes, G. L., *Remote Sensing of the Lower Atmosphere*, (New York, Oxford., 1994).

[9] Russchenberg, H. W. J, and L. P. Ligthart, "Backscattering by and Propagation Through the Melting Layer of Precipitation: A New Polarimetric Model", IEEE trans., **34**, 3-14 (1996).

Chapter 6

Air-borne observation by 95GHz cloud radar

Abstract

We analyze the results of air-borne observations of clouds and sea surfaces by 95GHz cloud radar. We show that the backscattering cross section per unit area of sea surface is almost constant for 95GHz and it is about -0.5dB. Therefore, our experiments show that sea surface can be used as a target to calibrate the space-borne cloud radar. Next we analyze the results of air-borne observations of Doppler velocity of cloud particles. One of the difficulties in the velocity measurements is the contamination of horizontal components of velocity. In order to overcome this problem, we introduce the correction where true velocity is obtained by subtraction of the velocity of sea surface. The retrieved terminal velocity of snow particles is larger than that of cloud particles. This can naturally be understood that the snow particles are larger than cloud particles.

6.1 Introduction

The conventional centimeter wavelengths radars (radio detecting and ranging) do not have sensitivity to detect cloud particles. Because those wavelengths are much longer than cloud particles, generally less than 100 μm, the radar echo from these particles are less than the detection limit. This is the main reason why we need millimeter wavelengths radars. From the technical point of view, since their frequency is very high, $i.e.$, 95GHz, W-band, it is very difficult to develop 95GHz cloud radars. Therefore only few countries, such as U.S., U.K., Germany and Japan have 95GHz cloud radars. In Japan, only Communications Research Laboratory (CRL) succeeded in development of the 95GHz cloud

64

radar called SPIDER (Special Polarimetric Ice Detection and Explication Radar) in 1998 [1]. SPIDER can measure co- and cross-polarized backscattered radiance by log detector and Doppler velocity by IQ detector. Moreover, it is designed to be able to perform an air-borne observation. Consequently, it becomes possible to instantly observe clouds at large area ($\sim$ 100 km).

CRL had the air-borne cloud observations by SPIDER above the Japan sea on 28 February 2000. The main aim of this study is to perform verification experiments of 95 GHz cloud radar from the air in order to design future space borne cloud experiments, *e.g.* EarthCare Mission in Europe and Japan. That is, air-borne system makes observations above clouds and sea surfaces prior to the launch of the satellite. The difficulty in the Doppler velocity in the air-borne measurements is somewhat similar to that for satellite ones.

To calibrate the space-borne cloud radar, sea surface or polar ice layer on Greenland is expected to be used. There are many measurements of backscattering cross section of the ocean surface by using air-borne radar (*e.g.* Masuko *et.al.*, 1986 [2]). However, there is no measurements of sea surface or ice layer by air-borne 95GHz cloud radar. Therefore, to establish such measurements is highly recommended.

6.2 Theory for clouds observed by 95GHz cloud radar onboard air craft

Fig. 6.1 (a) is SPIDER installed in the left side of the aircraft, Gulfstream II. Fig. 6.1 (b) is the magnification of Fig. 6.1 (a). An silver circle in a radar pod is an antenna with its aperture of 0.4 m.

Eq. 6.1 is the radar equation that connects the observed value (received power) and micro-physical informations (equivalent radar reflectivity factor) [3, 4].

$$
\begin{aligned}
P_r(mW) &= C_1 |K|^2 \frac{Z_e(mm^6/m^3)}{R^2} P_t(mW) \\
K &= |\frac{m_{ref}^2 - 1}{m_{ref}^2 + 2}|
\end{aligned}
\tag{6.1}
$$

where $P_r(mW)$ and $P_t(mW)$ are the received power and the transmitted power in unit of mW, R is the distance between targets and a radar in unit of m, m_{ref} is the complex reflective index of scatter and K is 0.83 for liquid water [5] and 0.42 for water ice [6] . In this study, we set K to be 0.83. C_1 is the calibration constant in unit of 1/m. For SPIDER, C_1 is 1.09×10^{-6} when the pulse width is $1\mu s$. Z_e denotes equivalent radar

Figure 6.1: (a) SPIDER installed in an aircraft, Gulfstream II. (b) magnification of radar in (a).

reflectivity factor. For the Rayleigh scattering, Z_e becomes

$$Z_e = \int_{size} dD \frac{dn(D)}{dD} D^6 \tag{6.2}$$

where D is the diameter of a scatter and $dn(D)/dD$ is a size distribution and it is independent on the wavelength of interest. Therefore, when the sizes of targets are larger or a number density is higher, Z_e becomes larger value. P_r and Z_e are often expressed in decibel units dBm and dBZ where $dBm \equiv 10log_{10}P_r(mW)$ and $dBZ \equiv 10log_{10}Z(mm^6/m^3)$, respectively.

In order to calculate the reflection by the sea surface, we use Eq. 6.3 as the radar equation (see Appendix).

$$P_r(mW) = C_2 \frac{\sigma_0}{R^2} P_t(mW) \tag{6.3}$$

where σ_0 is the cross section per unit area and C_2 is a calibration constant, and given by Eq. 6.4.

$$C_2 = 10^{18}C_1 \frac{2^2 ln2}{c\tau} \frac{\lambda^4}{\pi^5}. \tag{6.4}$$

Then σ_0 is derived by Eq. 6.5.

$$\sigma_0(dB) = P_r(dBm) - P_t(dBm) - 20log_{10}R - 10log_{10}C_2 \tag{6.5}$$

where $10log_{10}C_2$ is -24.85 for SPIDER.

Doppler velocity of cloud particles are derived by Eq.6.6 [3].

$$V = \begin{cases} c\delta\Theta/4\pi\delta Tf & \text{(air-borne observation)} \\ -c\delta\Theta/4\pi\delta Tf & \text{(ground-based observation)} \end{cases} \tag{6.6}$$

where c is the light speed, δT is the pulse reputation time and set to be $110\mu s$, f is the frequency and $\delta\Theta$ is Doppler phase shift recorded by radar. We define the upward direction to be "plus".

6.3 Results

Figs. 6.2 (a) and (b) are the results of the air-borne observations of clouds and sea surfaces above the Japan sea on 28 February 2000. Fig. 6.2 (a) is the received power that SPIDER observe clouds in nadir direction. The plane flew from left to right with a constant height of 6km and its velocity is about 200m/s. The strongest echo is about -44dBm and corresponds to the sea surface. The signals under 0 m are induced by the time delay due to the multiple scattering between the sea surface and clouds. Fig. 6.2 (b) is the same as Fig. 6.2 (a) but for Z_e. Strong echo of about 0 dBZ corresponds to snowfall.

Fig. 6.3 shows that the cross section per unit area of sea surface in Fig. 6.2 (a). It is almost constant and it is about -0.5dB. Therefore, our experiments show that sea surface can be used as a target to calibrate the space-borne cloud radar.

Fig. 6.4 (a) is the same as Fig. 6.2 (a) but the observation of Doppler velocity V calculated by Eq. 6.6. Fig. 6.4 (a) shows that the velocity of the sea surface is not 0 m/s. This is because the observation direction and sea surface are not perpendicular under the condition of constant flight altitude. For example, when the velocity of the air-plane is 200 m/s and the angle between flight and observation direction is 89 deg in flight direction, pseudo velocity of scatter is induced and 3.5 m/s. This is comparable to that of cloud particles. Thus the correction to eliminate pseudo velocity is necessary to derive the terminal velocity of cloud particles in the case of air-borne experiments. Fig. 6.4 (b) shows the Doppler velocity subtracted from that of sea surface. The velocity of snow particles is about -4m/s, and that of cloud particles is about -1m/s.

6.4 Summary

We analyze the results of air-borne observations by SPIDER. We show that the cross section per unit area of sea surface is almost constant and to be -0.5dB. Thus we show

that sea surface can be used as a target to calibrate the space-borne cloud radar. Next we analyze Doppler velocity by air-borne observations.

Masuko *et.al.* (1986) shows that radar reflectance of sea surface depends on the incident angle and wind velocity for 10GHz and 34GHz. In order to investigate such knowledges for 95GHz, we need air-borne experiments. The air-borne observation in 2001 is currently planning and should be contribute to this subject.

Appendix A

Eq. 6.7 is the received power $P_r(mW)$ by the scattering of sea surface when the altitude of air-plane is R [5].

$$P_r(mW) = \frac{P_t(mW)G}{4\pi R^2}\sigma_0 A \frac{S}{4\pi R^2} \qquad (6.7)$$

where $P_t(mW)$ is the transmitted power in unit of mW, G is an antenna gain, σ_0 is a cross section per unit area and A is the area of sea surface illuminated by radar and is calculated by Eq. 6.8. S denotes the area of antenna and it is the function of G (see Eq. 6.8).

$$A = \pi(R\frac{\delta\theta}{2})^2$$
$$S = \frac{\lambda^2}{4\pi}G \qquad (6.8)$$

where $\delta\theta$ denotes antenna beam width and λ is the wavelength of interest. By substituting Eq. 6.8 into Eq. 6.7, we derive the radar equation for sea surface (see Eq. 6.9).

$$P_r(mW) = C_2\frac{\sigma_0}{R^2}P_t(mW)$$
$$C_2 = \frac{\lambda^2}{2^8\pi^2}G^2\delta\theta^2 \qquad (6.9)$$

Eq. 6.1 is the weather radar equation [3, 4].

$$P_r(mW) = C_1|K|^2\frac{Z_e(mm^6/m^3)}{R^2}P_t(mW)$$
$$C_1 = 10^{-18}\frac{\pi^3 c\tau}{2^{10}\ln 2\lambda^2}G^2\delta\theta^2|K|^2$$
$$K = |\frac{m_{ref}^2 - 1}{m_{ref}^2 + 2}| \qquad (6.10)$$

where τ is pulse width.
Thus relation between C_1 and C_2 becomes

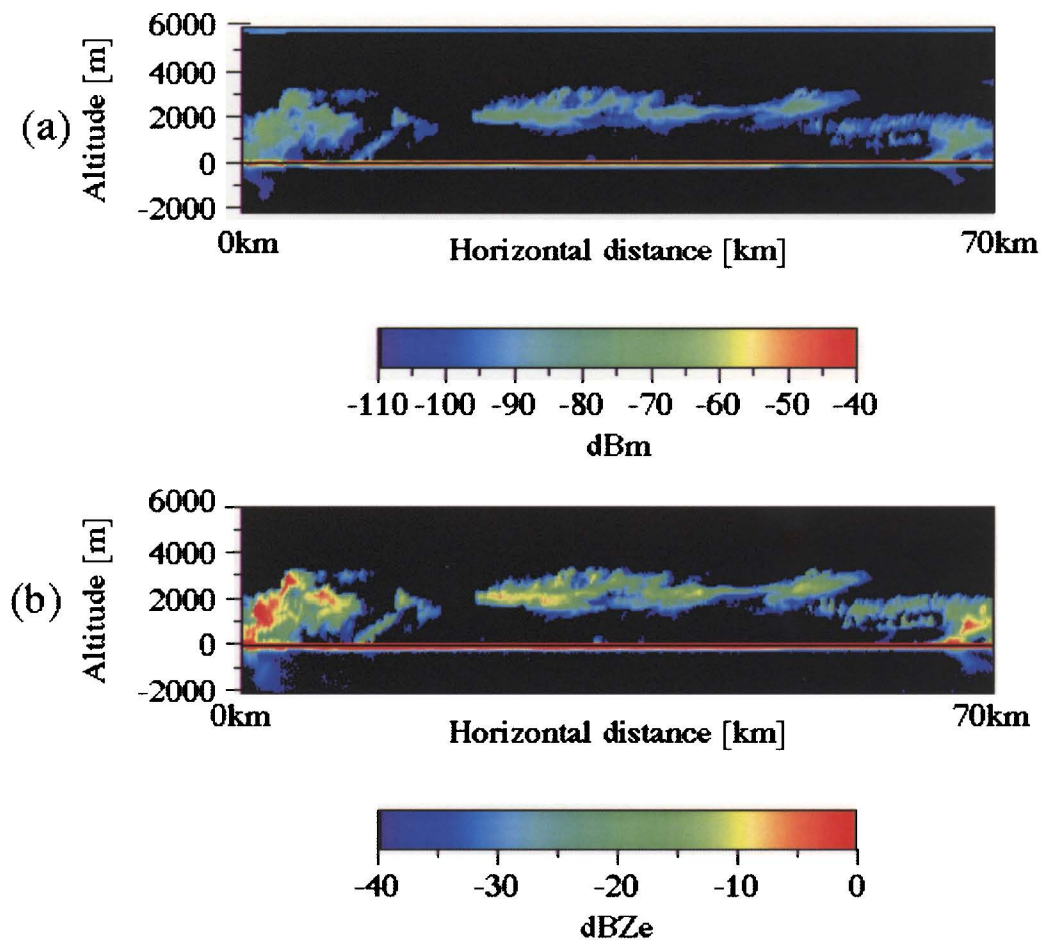$$C_2 = 10^{18}C_1\frac{2^2 ln2}{c\tau}\frac{\lambda^4}{\pi^5}. \qquad (6.11)$$

Figure 6.2: Airborne observation by SPIDER above the Japan sea on 28 February 2000. Air craft flew from left to right at a velocity of 200m/s and a height of 6km. Horizontal axis denotes horizontal distance and vertical axis denotes altitude. (a) Received power [dBm]. (b) Radar reflectivity factor [dBZ].
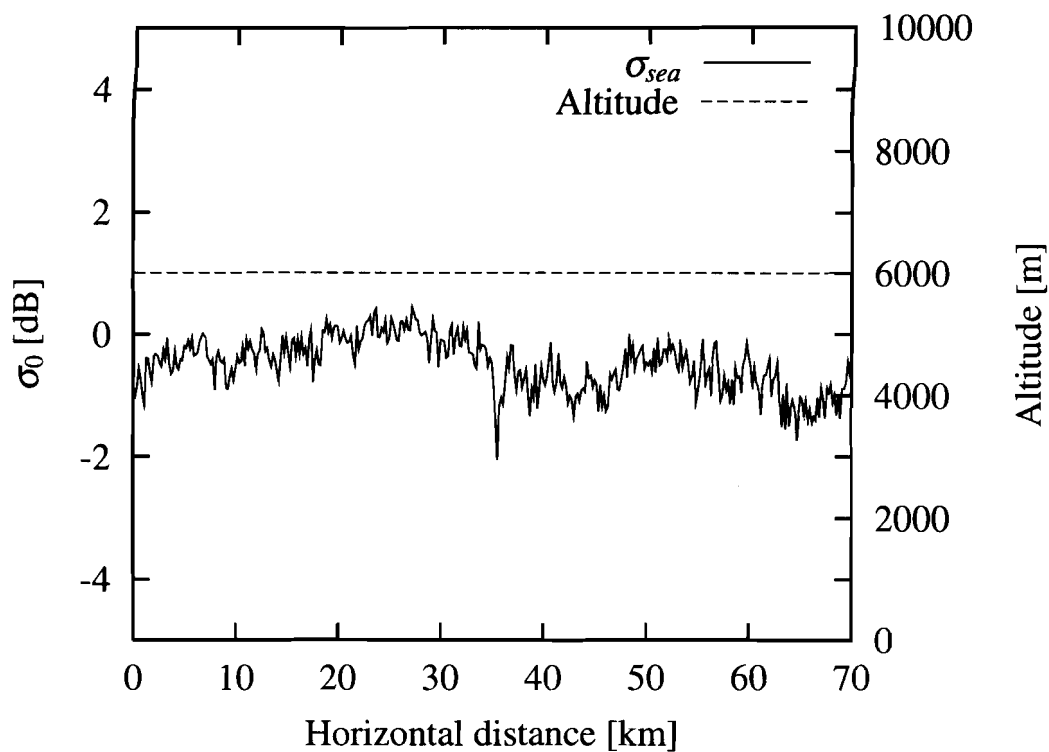
Figure 6.3: Result of the reflection by sea surface for 95GHz. Observed area is the same as that of Fig.6.2. Left side of vertical axis denotes cross section per unit area of the sea surface (solid curve). Horizontal axis denotes horizontal distance. Right side of vertical axis denotes altitude of the airplane (dashed curve) and is about 6km during this observation.
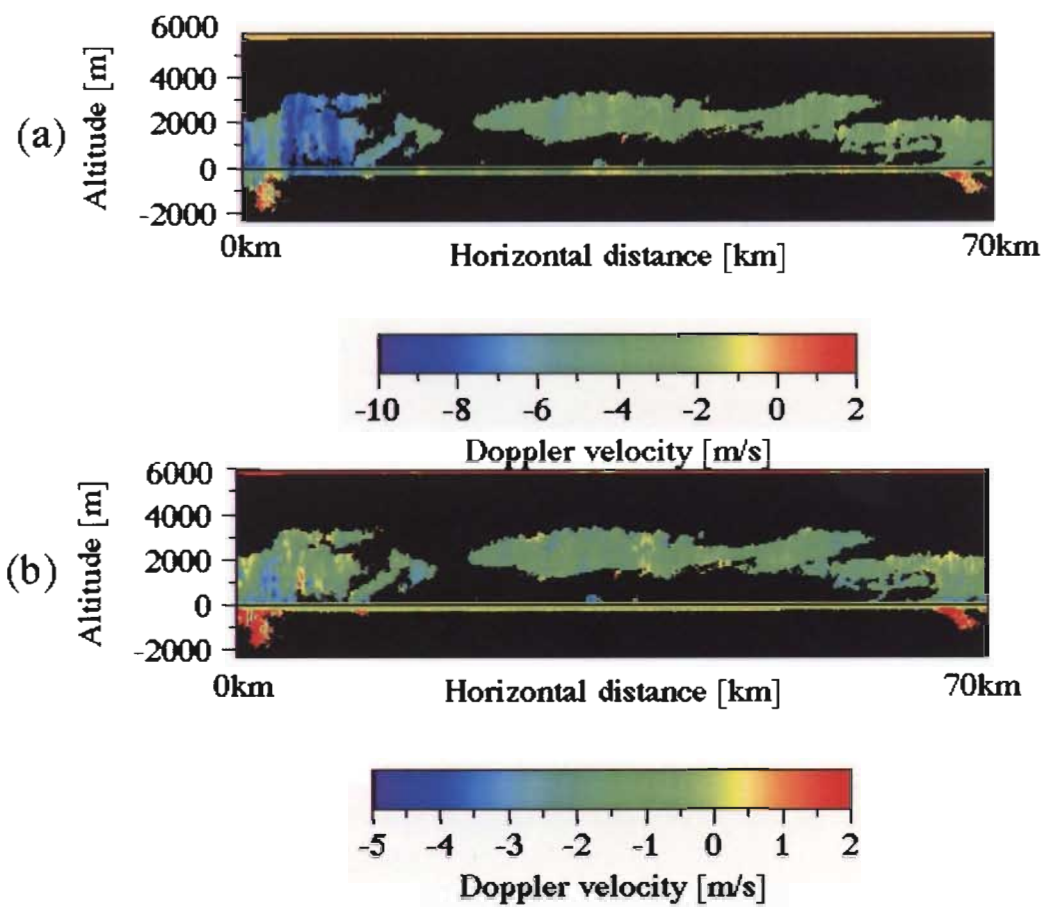
Figure 6.4: Same as Fig. 6.2 but the observation of Doppler velocity. (a) Raw data of Doppler velocity. (b) Same as (a) but calibrated by subtracting from Doppler velocity of sea surface.

Bibliography

[1] H. Horie, T. Iguchi, H. Hanado, H. Kuroiwa, H. Okamoto, and H. Kumagai, "Development of a 95-GHz Airborne Cloud Profiling Radar (SPIDER)", IEICE Trans. Commun., 2000, in press.

[2] Masuko H., K. Okamoto, M. Shimada, and S. Niwa, "Measurement of Microwave Backscattering Signatures of the Ocean Surface Using X Band and K_a Band Airborne Scatterometers," J. Geophys. Res., **15**, 13065-13083 (1986).

[3] Doviak R. J., and D. S. Zrnuc, *DOPPLER RADAR AND WEATHER OBSERVATIONS*, (Academic Press, Inc., 1993).

[4] Stephanes, G. L., *Remote Sensing of the Lower Atmosphere*, (New York, Oxford., 1994).

[5] Ulaby, F. T., R. K. Moore, and A. K. Fung, *MICROWAVE REMOTE SENSING ACTIVE AND PASSIVE, volume III, From Theory to Applications*, (Artech house, Inc., 1986).

[6] S. G. Warren, "Optical constants of ice from the ultraviolet to the microwave," Appl. Opt. **23**, 1206-1225 (1984).

Chapter 7

List of Publications

- *S. Iwasaki and T. Mukai, "ANALYSIS OF THE LIGHT SCATTERING BY ROUGH SURFACES", in preprints of Conference on Light Scattering by Nonspherical Particles: Theory, Measurements, and Applications, GISS, New York, pp. 229-232, 1998.

- S. Iwasaki and T. Mukai, Simulation for Light Scattering by Rough Surface Based on Kirchhoff's Diffraction Theory., Adv. Space. Res., **23**, 1213-1217, 1999.

- 岩崎杉紀、岡本 創, 氷雲の LIDAR 観測：LIDAR 方程式の再考, 第 7 回リモートセンシングフォーラム, カタログ番号 00 PG 0003, 23-26, 2000.

- S. Iwasaki, and H. Okamoto, Analysis of lidar returns from rectangles and hexagonal ice crystals., In Smith and Timofeyev (Eds.) IRS2000: Current Problems in Atmospheric Radiation, Deepak Publishing, 2000., in press.

- *H. Okamoto, S. Iwasaki, M. Yasui, H. Horie, H. Kuroiwa, and H. Kumagai, "95-GHz cloud radar and lidar systems: preliminary results of cloud micro-physics", In Wilheit, Masuko, and Wakabayashi (Eds) SPIE2000: Remote Sensing of the Atmosphere, Environment, and Space., 2000., in press.

- *H. Okamoto, M.Yasui, H.Horie, H.Kuroiwa, H.Kumagai, and S.Iwasaki, "OBSERVATION OF CLOUDS BY 95GHZ RADAR AND LIDAR SYSTEMS:RADIUS VERSUS FALL VELOCITY", Smith and Timofeyev (Eds.) IRS2000: Current Problems in Atmospheric Radiation, Deepak Publishing, 2000., in press.

- S. Iwasaki, and H. Okamoto, Analysis of lidar backscattering enhancement for pristine hexagonal ice crystals., In Singh, Itabe, Sugimoto (Eds) SPIE2000: Remote Sensing of the Atmosphere, Environment, and Space., 2000., in press.

* reprints are not included here.

SIMULATION FOR LIGHT SCATTERING BY ROUGH SURFACE BASED ON KIRCHHOFF'S DIFFRACTION THEORY

S. Iwasaki and T. Mukai

The Graduate School of Sci. and Tech., Kobe Univ., Nada 657-8501 Kobe, Japan

ABSTRACT

We examine the light scattering by rough surface based on the Kirchhoff theory of diffraction equation. The electric field on the arbitrary smooth surface surrounding the rough surface of interest is derived by the ray optics simulation for the scattering by such rough surface. After that, the intensity of the scattered light far from the smooth surface is deduced from an usual analytical way. It is found from a comparison of our results with those obtained by other methods, such as T-matrix method, that our method is applicable, at least, for spheroids. We also test our method to apply to the scattering by a two dimensional comb shaped surface, which is a special case of the rough analogue for the regolith layer on the surface of the airless small body in the solar system.

INTRODUCTION

It is well known that the following methods are available tools to calculate the light scattering by irregularly shaped dust particles, i.e. the discrete-dipole approximation (DDA) (Draine, 1988), the finite-difference time domain method (FDTD) (Yang and Liou, 1996), and the geometrical optics method (Jackson, 1975; Macke, 1993). However, these methods have an applicable limitation for the size parameter x, where x is defined as $x=2\pi a/\lambda$ (λ is a wavelength and a is a particle's radius). When we treat the scattering by an irregularly shaped particle, we usually choose a as its mean radius. In the case of DDA, x should be less than about 10. For FDTD, $20 \leq x \leq 40$. In $x \geq 50$, the geometrical optics is available. Although DDA and FDTD have great accuracy, it is hard to predict the scattering properties of the particles with $x \geq 50$.

The regolith layer existing on the surface of the airless bodies in the solar system contains such larger particles with $x \geq 50$. Therefore, in the analysis of the scattered light from such a regolith layer obtained by in situ measurements, we have to develop another convenient method. Integral equation method based on the Kirchhoff theory of diffraction equation (Jackson, 1975; Muinonen 1989; Yang and Liou, 1996) is a powerful scheme to calculate the light scattering by such larger aggregates, and its limit of applicability depends on the way to solve the scattering equation. Although the Kirchhoff theory of diffraction is used in for the scattering by a single particle, it is also applicable for the scattering by the grating. In this paper, we apply this method for a rough surface under the assumption that the rough surface is a part of the surface of a huge single particle.

SCATTERING MODEL

If the particle has no true charges and currents, the equation of the Kirchhoff theory of diffraction gives the solution of the light scattering problem at the observation point when the distance r between the particle and the observer is far enough. Namely,

$$\mathbf{E}_\infty(\mathbf{r}) = \frac{e^{ikr}}{ikr}\frac{k^2}{4\pi}\hat{\mathbf{r}} \times \oint dS' e^{-i\mathbf{k}\cdot\mathbf{r}'}\{\hat{\mathbf{r}} \times (\hat{\mathbf{n}}' \times c\mathbf{B}_s) - \hat{\mathbf{n}}' \times \mathbf{E}_s\}, \tag{1}$$

where $i = \sqrt{-1}$, k=$2\pi/\lambda$. The integration should be done over an arbitrary surface, which contains the particle of interest itself. $\hat{\mathbf{r}}$ is a unit position vector at the infinity observer, r' and $\hat{\mathbf{n}}'$ are, respectively, a
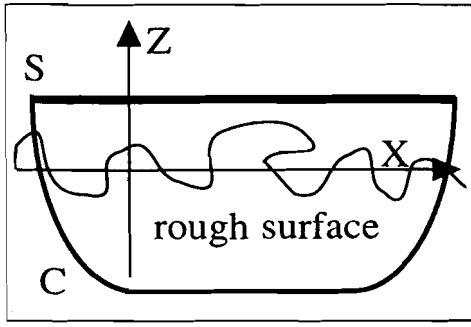
Figure 1.   The geometry of coordinate and the sample layer.   Scattering plane with roughness is defined on Z-X plane and the arbitrary closed surface S-C denotes the closed surface for integration of Eq.(1).
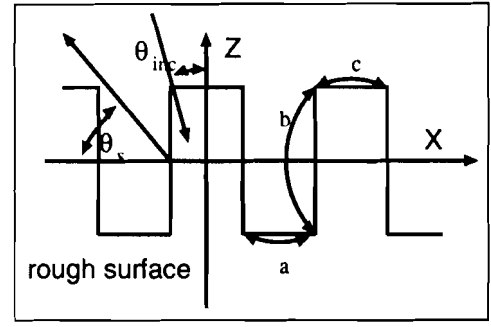

Figure 2.   The geometry of coordinate and the sample layer.   Scattering plane with comb-shaped roughness is defined on Z-X plane. The shape of comb is defined by three scales shown above as a, b, c.

position and a unit normal vectors on the surface of the integral contour. Subindices s and ∞ of $\mathbf{E}$ and $\mathbf{B}$ indicate the electro-magnetic field on the integral surface and the observed point, respectively (e.g. Jackson, 1975).

To solve Eq.1, we must know the electro-magnetic field, $\mathbf{E}_s$ and $\mathbf{B}_s$, on the integral surface. However, it is hard to decide them exactly, since Maxwell equations have no exact solution in the case of an irregularly shaped particle.

Kok (1993) showed the scattered light using Fourier series expansion for the electric field in the case of a two dimensional metallic surface. However, because they used a perfectly conducting surface, it seems hard to improve this solution for the scattering by the arbitrary material. Maradudin et al.(1990) calculated the light scattering by a two dimensional rough surface by using Hankel function of the first kind for integral equation method. However it is also difficult to apply this method for the surface defined by the many-valued function as the surface shown in Fig.1. On the other hand, to apply for the scattering by the arbitrary two dimensional shaped surface, Mendoza-Suarez and Mendez (1996) developed their theory. They calculated the scattering by the triadic Koch curve and they have shown that their method is valid even if a wavelength is shorter than the Rayleigh smoothness criterion. It is known, however, that it is valid only for the case of a two dimensional surface and it also seems hard to extend it to calculate the scattering properties for the three dimensional problems.   Yang and Liou (1996) calculated the light scattering properties of an irregularly shaped particle based on the Kirchhoff theory of diffraction equation using the geometrical optics approximation.   It is possible for the geometrical optics approximation to apply for the arbitrary three dimensional case. Thus, we use this method to solve Eq. 1.

First, we divide an incident light into thin light bundles that have the same phase in each bundle ray. To be same phase on the area enlighten by the bundle, we set a width of the diffused light bundle less than about $\lambda/10$ everywhere (Yang and Liou, 1996).

We assume that each light bundle ray is described by Fresnel formula (Jackson 1975).

Since the light bundle is not a parallel light after incidence, we assume that the electric field changes its magnitude as

$$\mathbf{E}^{p+1} = \mathbf{E}^p \exp(i\frac{2\pi m}{\lambda}l)\sqrt{\frac{ds_p}{ds_{p+1}}}, \qquad (2)$$

where $\mathbf{E}^p$ and ds_p are the electric field and the cross section of the light bundle at the p-th reflection and transmission point, and m is an optical constant. l is the length between p+1-th and p-th reflection and transmission points. This relation comes from the energy ($\propto| \mathbf{E}(\mathbf{r}')|^2$) conservation law.

In the Kirchhoff theory of diffraction, we must choose the integrated contour as the surface that covers up all the particle of interest. This implies that we can obtain the same result of Eq.1 after the integration over an arbitrary contour contained the particle as that over the real surface of the particle. When we take the contour near the scattered sample, there is no need to make much light bundle in simulations to earn the number density of the ray to increase the statistical significance. In the case of rough surface, we take the integral area of the surface S-C as shown in Fig.1. That is, we consider a contour S plane, which is a smooth plane above the surface layer. In addition, a contour C, which makes a closed surface with the contour S,
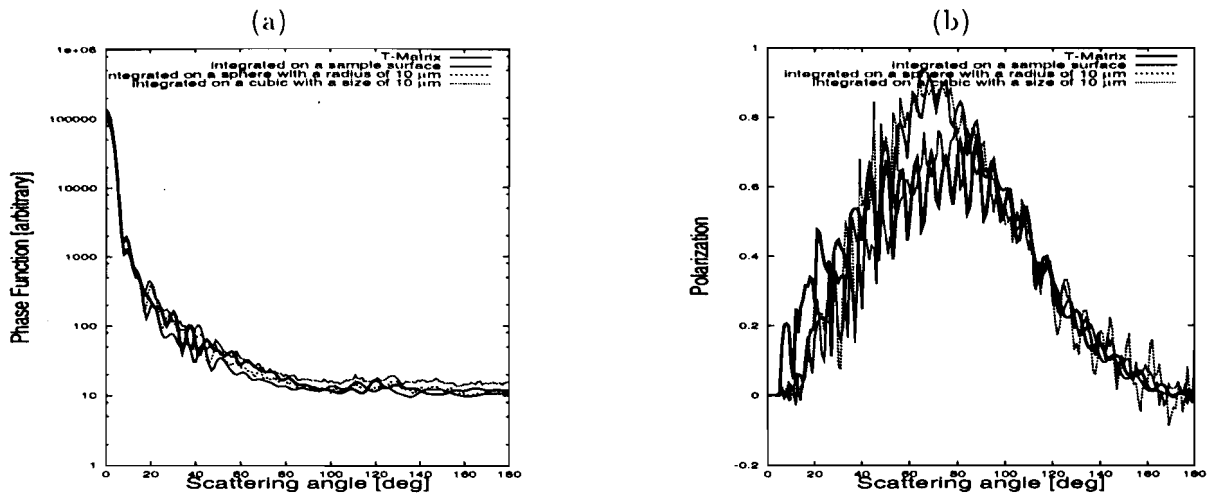
Figure 3.   (a) Phase function vs scattering angle, obtained for the astronomical silicate prolate at a wavelength of 0.55 μm, and its complex refractive index is $1.719+0.02936i$. The prolate has the length of horizontal and rotational axes of 2 μm and 3 μm, respectively, *i.e.* its effective size parameter=26.2. The size of cubic and the radius of sphere are 10 μm. The result compared by T-matrix method (thick solid curve) is compared with those by the Kirchhoff theory of diffraction (our method) for different surfaces of integration. The thin solid curve denotes the result by the integration over the real prolate surface. The dashed curve denotes the case for a sphere as an arbitrary surface, and the dotted curve gives a cubic case. (b) Same as (a) but polarization vs scattering angle and the oblate has the length of horizontal and rotational axes of 3 μm and 2 μm, respectively, *i.e.* its effective size parameter=29.5.

is assumed under the real rough surface. Since the scattered light penetrated into the surface decreases its intensity as an exponential function, we neglect the electro-magnetic field of the scattered light on a contour C. Therefore we just integrate over the plane contour S, not on the each targets' surface.

RESULTS

In order to make sure that the result is independent of the integral contour, we calculated the light scattering for the two types of contours, *i.e.* a large sphere and a cubic. We estimated, based on T-matrix method (Ishimaru and Yeh, 1984), the scattering properties of the spheroids, respectively, consisting of the astronomical silicate (Draine, 1985), where the scattered intensity is averaged over the directions for the spheroids. We compared these results with those deduced from our method for a sphere and a cubic as an arbitrary contour surrounding the spheroids of interest. It is found that the Kirchhoff theory of diffraction in the geometrical optics approximation is an available tool to simulate the light scattering by a particle with a size parameter x $\geq$ 30 (see Figs.3(a) and 3(b)). Consequently, it is shown that the integration over an arbitrary surface (large sphere and cubic) gives the similar result to that obtained by the integration over the real sample surface (spheroid). Next, we calculated the light scattering by a two dimensional comb shaped surface layer (see Fig.2), which is one of the simplest case of the rough surface.

In Fig.4(a), the result of scattering properties deduced from our method is shown, where the diffraction pattern of comb shaped layer occurs at about θ_s=40 and 80[deg], and a specular scattering appears at about θ_s=120[deg]. Solid curve is the result of the integration over the sample surface and dotted one is those of the surface S. In the case of Fig.4(a), the effective size parameter kb=2.5 is small and it may be out of the applicable size parameter region of the geometrical optics approximation. Fig.4(b), however, shows a significant agreement between two results.

SUMMARY

We applied the Kirchhoff theory of diffraction equation for the light scattering by rough surface. It is found that a replacement of the integration contour from real rough surface to an arbitrary smooth surface provides a simple way to solve the scattering problem. Moreover, it is possible for this scheme to estimate the scattering pattern for the rough surface with the minimum structure size larger than a few wavelengths
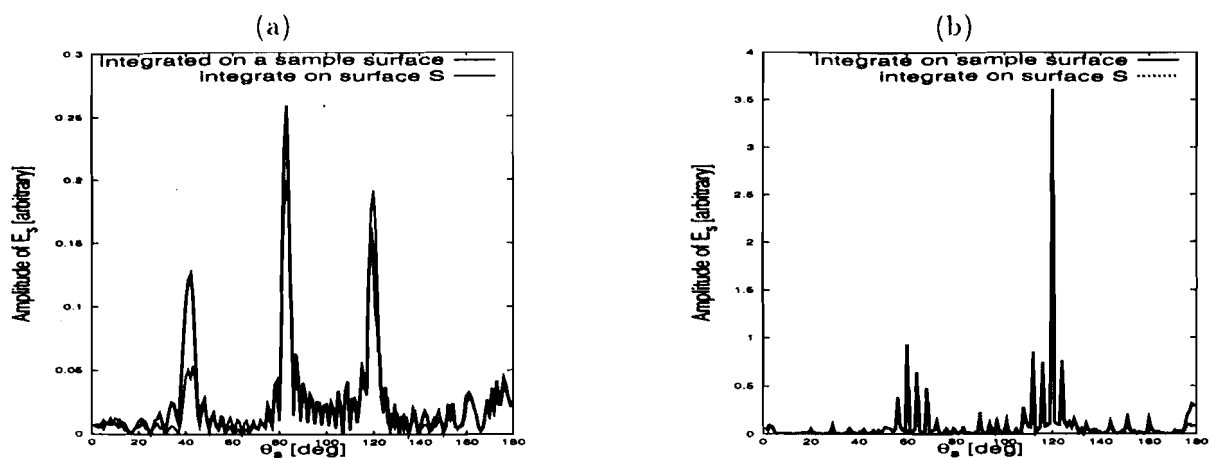
Figure 4. Amplitude of the electric field $\mathbf{E}_s$ defined in Eq.1 vs θ_s (see the definition of θ_s in Fig.2). The simulation has been done for the two dimensional comb shaped surface, consisting of astronomical silicate, shown in Fig.2. Solid curve is the result of the integration over the sample surface and dotted one is those of the surface S. Incident angle θ_{inc} is 30[deg], λ is 0.55μm, and its complex refractive index is 1.719+0.02936i. The number of grooves on rough surface is 12. (a) a=c=0.44μm, b=0.22μm (kb=2.5) in Fig.2, and (b) a=c=4.4μm, b=2.2μm (kb=25).

of interest. We will continue to improve this method to apply for more realistic rough surface analogue to the surface of asteroid. Furthermore, a comparison of the simulation results with the data of the laboratory scattering measurements will be done in our future work.

ACKNOWLEDGMENTS

References

Bohren, C. F. and D.R.Huffman, Absorption and Scattering of Light by Small Particles. *Wiley, New York*, (1983).

Draine, B. T., Tabulated optical properties of graphite and silicate grains. *ApJ*, **57**, 587-594 (1985).

Draine, B. T., The discrete-dipole approximation and its application to interstellar graphite grains. *ApJ*, **333**, 848-872 (1988).

Ishimaru, A. and C.W. Yeh, Matrix representations of the vector radiative-transfer theory for randomly distributed nonspherical particles. *J.Opt.Soc.Am.A.*, **1**, 359-364 (1984).

Jackson, J.D., Classical Electrodynamics. *Wiley, New York*, (1975).

Kok, Y. -L., General solution to the multiple-metallic-grooves scattering problem: the fast-polarization case. *Appl.Opt.*, **32**, 2573-2581 (1993).

Macke, A., Scattering of light by polyhedral ice crystals. *Appl.Opt.*, **32**, 2780-2786 (1993).

Maradudin, A.A., T.Michel, A.R.Mcgurn, E.R.Mendez, Enhanced Backscattering of Light from a Random Grating. *Ann.Phys.*, **203**, 255-307 (1990).

Mendoza-Suarez, A., E.R.Mendez, Light scattering by a reentrant fractal surface. *Appl.Opt.*, **36**, 3521-3531 (1997).

Muinonen, K., Scattering of light by crystal: a modified Kirchhoff approximation. *Appl.Opt.*, **28**, 3044-3050 (1989).

Yang, P., and K.N.Liou, Geometric-optics-integral-equation method for light scattering by nonspherical ice crystals. *Appl.Opt.*, **35**, 6568-6584 (1996).

Yang, P., and K.N.Liou, Finite-difference time domain method for light scattering by small ice crystals in three-dimensional space. *J.Opt.Soc.Am.A.*, **13**, 2072-2085 (1996).

氷雲の LIDAR 観測：LIDAR 方程式の再考

神戸大学大学院 自然科学研究科 ○岩崎 杉紀
通信総合研究所 岡本 創

Lidar Observation for the Remote Sensing of the Ice Clouds: Reconsideration of the Lidar Equation

○ Suginori IWASAKI, Graduate School of Science and Technology, Kobe University
Hajime OKAMOTO, Communications Research Laboratory

Abstract

本研究では、氷雲粒子のような非球形粒子に適応できる一般的な lidar 方程式を導出した。この結果、球形粒子に対して通常用いられる lidar 方程式が距離の二乗に反比例することのに対し、非球形粒子に対しては lidar 方程式の距離依存性が粒子形状やオリエンテーションにより変化することが示された。すなわち、水平ランダムオリエンテーションをしている針状六角柱では距離の一乗に反比例し、板状六角柱では距離に依存しないことが示された。また、三次元ランダムオリエンテーションをしている針状と板状六角柱の場合は、共に距離の一乗に反比例することが示された。

1 導入

　lidar 観測では、地球の放射収支の大きな不確定性要因である雲の雲底や雲頂、雲粒子の粒径や形状といった情報を得られることが期待されている。近年、lidar による雲の観測は地上のみならずスペースシャトルを用いた観測も行われている [1]。
　この観測結果の定量的な解釈のために、lidar 方程式 [2],[3],[4] を用いた解析法 [5],[6] が用いられている。lidar 観測の結果の解釈には、lidar 方程式中に含まれる後方散乱断面積を理論的に求めなければならないが、従来からの ray-tracing 法を用いた研究では、後方散乱断面積の計算は困難であることが示されている [7],[8]。本研究では、第 2 章で実際に氷粒子の後方散乱断面積が発散することを数値的に示した。第 3 章では、そのような場合にも適用できる一般的な lidar 方程式を ray-tracing 法を用いて後方散乱における散乱断面積の展開係数を導いた後、それを利用して lidar 方程式の一般形を導出した。第 4 章では水平ランダムオリエンテーションやランダムオリエンテーションをしている六角柱の氷粒子の lidar 方程式を導いた。

2 従来の lidar 方程式とその問題

　lidar 方程式は、

$$P_r(Z) = ECZ^{-2}\{C_{bk,mol} + C_{bk,aero}\}T_{mol}^2 T_{aero}^2 \tag{1}$$

で与えられる [2],[3],[4]。ここで、E, C は lidar の機器の定数、$C_{bk,mol}$, $C_{bk,aero}$ は大気分子とエアロゾルや雲粒子の後方散乱断面積、Z は高度、T_{mol}, T_{aero} は大気分子とエアロゾルや雲粒子の透過係数である。したがって、式 1 を取り扱うためには、後方散乱断面積を知らねばならない。しかし、以下で見るように $C_{bk,aero}$ は発散してしまい、lidar 方程式を使うことができない。
　まず、δC_{sca} は散乱角とその角度刻の関数であるべきなので、$\delta C_{sca}(\theta)$ を $\delta\theta$ で展開すると、

$$\delta C_{sca}(\theta) = C_{sca}\{f_0(\theta)\delta_{\theta\theta_i} + f_1(\theta)d\theta + \frac{1}{2}f_2(\theta)d\theta^2 + \cdots\} \tag{2}$$

$\delta_{\theta\theta_i}$ はクロネッカーのデルタで θ_i は鏡面反射する時の散乱角ある。第一項は、平らな鏡面に垂直入射したときに効く項である。$\delta\theta$ に依らないのは、鏡面散乱の場合は入射光が平行であれば反射光は角度分散を起こさないからである。第二項は、第 4.2 節で示すように無限に長い円柱のように散乱する場合 [10] に効く項である。第三項は Mie 散乱 [10] のように球面波で散乱する場合に効く項である。また、立体角は

$$\delta\Omega = \int_{\theta-\delta\theta}^{\theta}\int_0^{2\pi}\sin\theta d\theta d\phi \propto \begin{cases} \delta\theta & (\theta \neq 0, 180\ deg) \\ (\delta\theta)^2 & (\theta = 180\ deg) \end{cases} \tag{3}$$

で定義されている。ここで、$C_{bk,aero}$ が $4\pi dC_{sca}/\delta\Omega$ と定義されているので、式 2 と式 3 により f_0 か f_1 が値を持った場合 $C_{bk,aero}$ は発散する。Mie 散乱の場合は f_0 と f_1 は 0 である。
　図 1 は、針状六角柱の軸を水平面に平行にさせながらランダムオリエンテーションをさせた時の 位相関数 $P_{11}(\theta)$ と散乱角の関係である。$P_{11}(\theta)$ は、$\frac{\delta C_{sca}}{\delta\Omega}/C_{sca}$ で定義される散乱確率を現す関数である。図より角度刻が小さくなればなるほど $P_{11}(180)$ が大きくなる。これより $\delta\theta$ を無限小にすると $P_{11}(\theta)$ が発散することが解る。$C_{bk,aero}$ は、$4\pi P_{11}(180)C_{sca}$ とも書けるので $C_{bk,aero}$ も発散することが解る。したがって、この場合は従来の lidar 方程式を用いることができない。このような発散は球形粒子では起こらない。したがって、この発散は散乱体が非球形であるために起こる。氷雲は雲粒子が不規則形状をしているので、lidar 観測の結果を解析するためには式 1 を見直さなければならない。
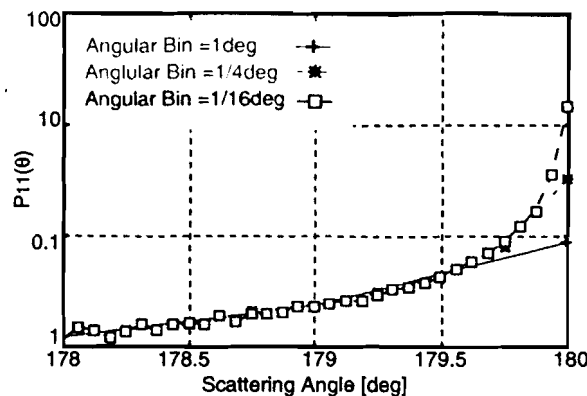
Figure 1: 散乱角 θ と $P_{11}(\theta)$。角度刻 $\delta\theta$ が小さくなればなるほど $P_{11}(180)$ が大きくなる。したがって、$\delta\theta$ を無限小にすると $P_{11}(\theta)$ が発散することが解る。後方散乱断面積 σ_{bk} は $4\pi P_{11}(180)C_{sca}$ なので、σ_{bk} も同様に発散する。

3 一般的な lidar 方程式

まず最初に、単純化した lidar システムと lidar 観測の幾何と記号を図 2 のように定義する。また、雲粒子は表面がレーザー光の波長に比べ十分滑らかで、針状六角柱か板状六角柱が水平ランダムオリエンテーションをしていると仮定し θ_i が 180 とした。また、レーザー入射光は十分平行になっているため望遠鏡の視野角に常に入っているものとする。簡単のため、散乱体は入射レーザー光の幅に比べ十分高い高度にあるので雲中の体積 V から望遠鏡を見る立体角 $\delta\Omega$ は一定とした。

Z'	散乱体の存在する高度
δz	高度分解能
V	高度分解能と入射レーザー光の断面がなす体積
I0	短時間単位面積当たりのレーザー光のエネルギー
Pr	雲中の体積Vからの散乱を望遠鏡が受信する電力
dn(r)/dr	散乱体のサイズ分布
G(r)	散乱体の幾何断面積
s0	望遠鏡の半径
a	入射レーザー光の半径
Tmol	分子の透過率
Tcloud	雲粒子の透過率
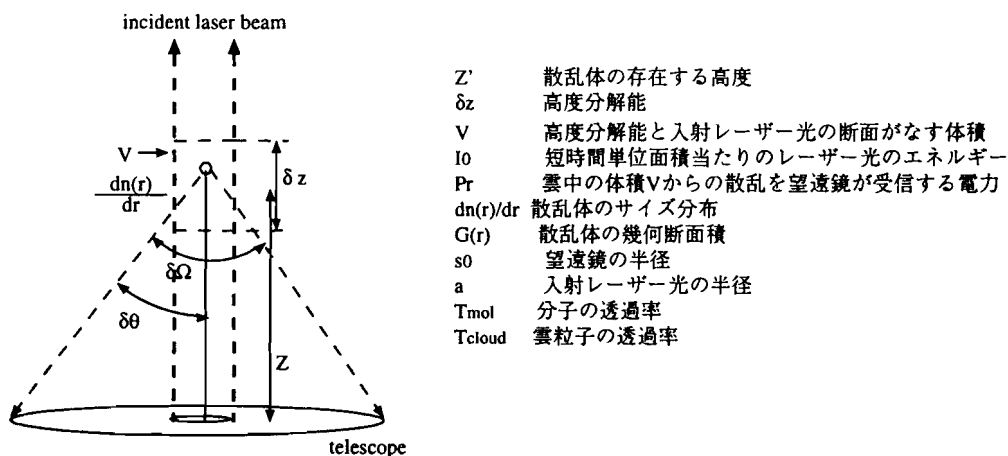
Figure 2: lidar システムと lidar 観測の幾何と記号の定義。

このとき、望遠鏡の受信電力 P_r は、

$$P_r = I_0 \int_{\delta\Omega(\theta=180-\delta\theta)}^{\delta\Omega(\theta=180)} \int_V dv \int_{size} dr \frac{dn(r)}{dr} \frac{dC_{sca}(180)}{d\Omega} d\Omega T_{mol}^2 T_{cloud}^2. \tag{4}$$

と書ける。式 4 に式 2 を代入し整理すると、

$$P_r = I_0 V \int_{size} dr \frac{dn(r)}{dr} C_{sca}(r) \{f_0(180) + f_1(180)\frac{s_0}{Z} + \frac{f_2(180)}{2}(\frac{s_0}{Z})^2 + \cdots\} T_{mol}^2 T_{cloud}^2. \tag{5}$$

となる。これが一般的な場合の lidar 方程式である。

4 数値解析

4.1 球形粒子の場合

球形粒子の場合、後方散乱断面積は有限の一定値を持つ[10]。この場合、$d\Omega$ は $d\theta^2$ に比例するので、C_{bk} も $d\theta^2$ に比例する。したがって、式 2 と式 3 を比較すると f_0 と f_1 が 0 であるので、式 5 より lidar 方程式は

$$P_r = I_0 V \int_{size} dr \frac{dn(r)}{dr} C_{sca}(r) \frac{f_2(180)}{2}(\frac{s_0}{Z})^2 T_{mol}^2 T_{cloud}^2. \tag{6}$$

となる。これは従来の lidar 方程式に一致する。

4.2　水平ランダムオリエンテーションをした針状六角柱の場合

　図 3 は、長軸を水平面に平行にしながらランダムオリエンテーションをしている針状六角柱の場合の $\delta\theta$ と $\frac{\delta C_{sca}}{\delta\theta}/C_{sca}$ の関係を示したものである。この計算は ray-tracing 法を用いて計算をした。また、後方散乱では回折が無いので [9],[10]、回折を含めない計算をした。それぞれの曲線は、10 個の異なる種を元にして乱数を振って計算した結果である。また、ここでの光学定数の実部は 1.31、虚部は 2.54×10^{-9} で波長 $0.53\mu m$ [8]、六角柱の長軸の長さを $86\mu m$、六角形に外接する円の半径を $14\mu m$(軸比 3) とした。この図と式 2 より $f_1(180)$ が支配的な散乱であることが解る。このときの $\frac{1}{C_{sca}}\frac{\delta C_{sca}}{\delta\theta}$ は 2.5×10^{-2}
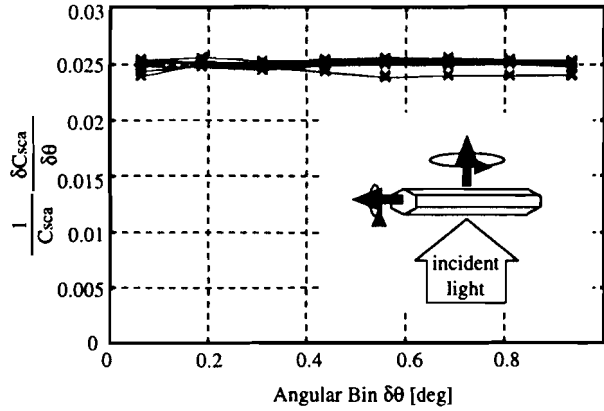
Figure 3: 水平ランダムオリエンテーションをした針状六角柱の場合の角度刻み $\delta\theta$ と $\frac{\delta C_{sca}}{\delta\theta}$ の関係。乱数は 10 個の異なる種を元にし計算した。この図より $f_1(180)$ の項が支配的な散乱であることが解る。

となった。

　可視で氷を見た場合、吸収がほとんどないため C_{sca} は $2G(r)$ にほぼ等しく、$f_1(180)$ は吸収と回折がないため氷粒子のサイズに依らない関数と考えられる。したがって、lidar 方程式は

$$P_r \cong 2I_0 V f_1(180)\frac{s_0}{Z}\int_{size} dr\frac{dn(r)}{dr}G(r)T_{mol}^2 T_{cloud}^2. \tag{7}$$

となり、雲粒子と望遠鏡の間の距離 Z の一乗に反比例する。このことは、次のような類推から考えると解りやすい。

　今、水平ランダムオリエンテーションをしている金属製の六角柱の散乱を考える。このとき、光散乱は六角柱の側面の長方形で一回だけ散乱する。水平ランダムオリエンテーションは六角柱を長軸の周りに無限に回転させ、その各々の散乱を計算し、散乱角ごとに散乱エネルギーの総和を求める。すなわち、全ての散乱事象をまとめて考えると、いろいろな方向に側面を向けた無数の六角柱の散乱角ごとの散乱エネルギーの総和を計算していることと同じになる。ここで、円柱は側面の数が無限にある正多角柱であるため、これら無限の回転をしている六角柱の散乱は円柱一つの散乱と同じ性質を示すと考えられる。

　以上のことは、ここでの理論計算では六角柱が氷ではなく金属であり、有限回転数ではなく無限に回転させるという違いがあるが、その類推から針状六角柱の光散乱が円柱の光散乱と同じ距離依存性を示すことが分かる。

4.3　水平ランダムオリエンテーションをした板状六角柱の場合

　六角形を水平面に平行にしながらランダムオリエンテーションをしている板状六角柱の光散乱は、ray-tracing 法を使わなくとも幾何光学近似で解ける。これは、後方散乱には回折がないため、無限の幅、有限の厚さを持った氷の板に光が垂直入射した場合の散乱と同等のものになるからである。この板の反射係数は

$$R_{plate,geo,bk} = \frac{dC_{sca}(180)}{C_{sca}} = \frac{2R_{plate,fresnel}}{1 + R_{plate,fresnel}} \tag{8}$$

と書ける。ここで、$R_{plate,fresnel}$ は垂直入射したときの Fresnel の反射係数である。これより、この場合の散乱は式 2 の $f_i,(i \neq 0)$ が 0 のときに対応する。$R_{plate,fresnel}$ はサイズに依らないため、lidar 方程式は

$$P_r = 2I_0 V R_{plate,geo,bk}\int_{size} dr\frac{dn(r)}{dr}G(r)T_{mol}^2 T_{cloud}^2. \tag{9}$$

となり、lidar 方程式の距離の依存性がなくなる。つまり散乱光は拡散しない。このことは、散乱光が見える位置から少し離れると散乱光が観測されないことを意味する。

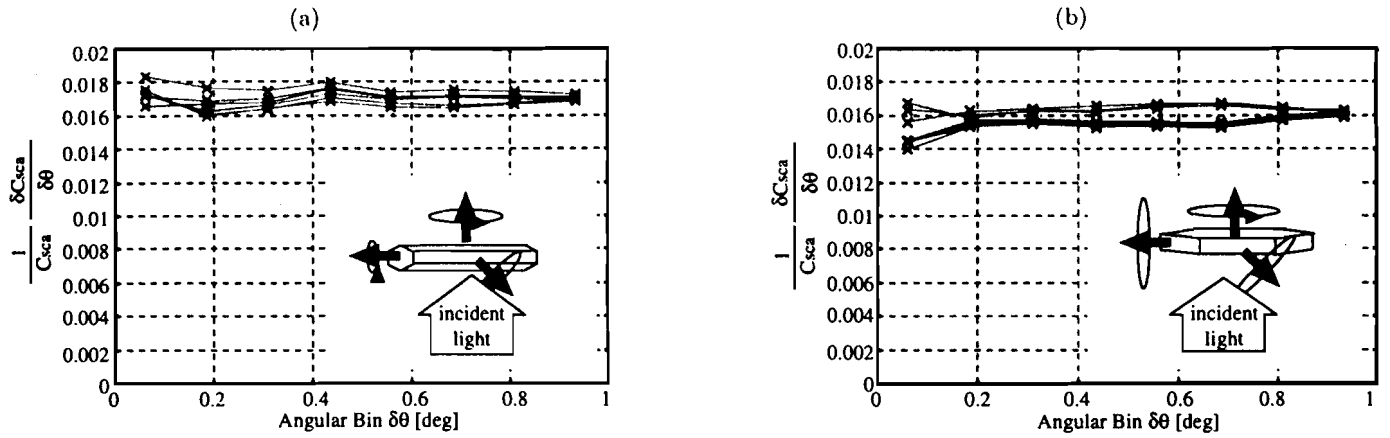**Figure 4:** 針状六角柱 (a) と板状六角柱 (b) の三次元ランダムオリエンテーションをした針状六角柱の場合の角度刻み $\delta\theta$ と $\frac{\delta C_{sca}}{\delta\theta}$ の関係。針状六角柱は第 4.2 節と同じものを使用した。板状六角柱はこの針状六角柱と同体積で軸比が 1/3 のものを使用した。この図よりどちらの場合でも $f_1(180)$ の項が支配的な散乱であることが解る。

4.4 三次元ランダムオリエンテーションの場合

この節では針状と板状六角柱の三次元ランダムオリエンテーションの計算を行った。図 4 は、三次元ランダムオリエンテーションをした針状六角柱と板状六角柱の場合の角度刻み $\delta\theta$ と $\frac{\delta C_{sca}}{\delta\theta}$ の関係を示したものである。この図よりどちらの六角柱とも $f_1(180)$ が支配的な散乱であることが解る。この距離 Z 依存性は水平ランダムオリエンテーションをした針状六角柱の場合と同じである。つまりこの場合の lidar 方程式は式 7 となる。このときの $\frac{1}{C_{sca}}\frac{\delta C_{sca}}{\delta\theta}$ は、針状の場合が 1.7×10^{-2}、板状の場合が 1.6×10^{-2} である。

本章より、氷雲の lidar 観測を解析するための lidar 方程式は、今までの lidar 方程式に変更を加えなければならないことが解る。

5 まとめ

本研究では、氷雲粒子のような非球形粒子に適応できる一般的な lidar 方程式を導出した。この結果、lidar 方程式の距離依存性が粒子形状やオリエンテーションにより変化することが示された。すなわち、従来の lidar 方程式では距離の二乗に反比例すると仮定しているが、水平ランダムオリエンテーションをしている針状六角柱では距離の一乗に反比例し、板状六角柱のでは距離に依存しないことが示された。また、三次元ランダムオリエンテーションをしている針状と板状六角柱の場合は、それぞれ距離の一乗に反比例することが解った。この方程式は、六角柱の氷粒子の光散乱に限ったことではない。後方散乱断面積が発散するものであればどんな形状の粒子に対しても成り立つ。

通信総合研究所では 95GHz のレーダと lidar の同時観測が計画されている。このときここで示した lidar 方程式を実際の解析に用いる予定である。また、距離依存性が違うため、bi-static lidar を用いればこの方程式の検証ができると考えられる。この観測結果および検証は今後御報告する予定である。

References

[1] Miller S.D., G.L.Stephens, and A.C.Beljaars., *Geophys.Res.Lett.*, **26**, 1417, 1999.

[2] Fernald. F.G., B.M.Herman, and J.A.Reagan., *J.Appl.Meteor.*, **11**, 482, 1972.

[3] Fernald. F.G., *Appl.Opt.*, **23**, 652, 1984.

[4] Stephanes.G.L., *Remote Sensing of the Lower Atmosphere*, New York, Oxford., 1994.

[5] Klett J.D., *Appl.Opt.*, **20**, 211, 1981.

[6] Sassen K., H.Zhao, and G.C.Dodd., *Appl.Opt.*, **31**, 2914, 1992.

[7] Takano.Y and K.N.Liou., *J.Atmos.Sci.*, **46**, 3, 1989.

[8] Macke.A., J.Mueller, and E.Raschke., *J.Atmos.Sci.*, **53**, 2813, 1996.

[9] Hapke B., *Theory of Reflectance and Emittance Spectroscopy*, Cambridge Univ. Press. 1993.

[10] Bohren.C.F. and D.R.Huffman., *Absorption and Scattering of Light by Small Particles*, Wiley, New York., 1983.

Analysis of lidar backscattering enhancement for pristine hexagonal ice crystals

Suginori Iwasaki [a] and Hajime Okamoto[b]

[a]The Graduate School of Science and Technology, Kobe University.
1-1 Rokko-dai, Nada, Kobe 657-8501, Japan.
[b]Communications Research Laboratory.,
893-1 Hirai, Kashima, Ibaraki 314-0012, Japan.

ABSTRACT

We analyze lidar backscattering enhancement for pristine hexagonal ice crystals by using Fraunhofer diffraction based on Kirchhoff's diffraction theory (KD). Our numerical computations show that received power $P_r(Z)$ at the altitude Z in lidar equation is proportional to $Z^{-\alpha}$, where α is a function of Z, size and shape of particles. $P_r(Z)$ is proportional to $Z^{-1.5}$ for hexagonal plate and column randomly oriented in horizontal plane at $Z=200$ m where its aspect ratios are 1/3 and 3 and mode radiuses are $100\mu m$. Our calculations suggest hexagonal ice crystals that have mode radiuses of 100 μm and 30 μm with perfectly oriented in horizontal plane have anomalous backscattering enhancement compared with a sphere at even high altitude. This might explain the phenomena reported by Platt et. al. (1978).[1,2]

Keywords: lidar, backscattering enhancement, diffraction

1. INTRODUCTION

Lidar is one of the most effective tools to investigate the cloud profiles such as vertical structure, shapes and sizes of ice crystals, which are the unknown factors to estimate the radiative properties of clouds with high accuracy. Therefore, for last twenty years, there have been intensive ground-based measurements by use of lidar and some progresses have been made in the analysis. Fernald et. al. (1972)[3] developed an analytical method for the inversion problem in lidar observations. Klett (1981)[4] modified their method to avoid instabilities in the inversion problem. Besides, there are some observational evidence which shows non-sphericity plays a key role. Platt et. al. (1978)[1,2] showed that some unusual lidar returns from a middle-level cloud were observed. They also showed ice clouds in the zenith gave a very high backscattering but a very small depolarization, which is called zenith-enhanced backscatter (ZEB). Mishchenko et. al. (1997) considered disks and spheroids with size parameter up to 50 (e.g. $r = 5\mu m$ at $\lambda = 0.63\mu m$) as ice crystals and calculated lidar backscattering from these particles by using T-matrix method. They showed "ZEB peak can be produced only by horizontally oriented disks but not by horizontally oriented spheroids or particles in random orientation". Despite from these efforts, there is a theoretical difficulty in interpretation of lidar signals. That is, in lidar signals, it is not possible to derive analytical solutions for non-spherical particles when the size of particles is much larger than the wavelength. Ray-tracing method is widely used in visible analysis, however, it has also a fundamental difficulty in backscattering. The applicability of this method is tested and it turns out that geometrical optics (GO) can be applicable when the altitude is very close to the ground (e.g. 100 m).[6] Our final goal of this study is to explain the mechanism of unusual lidar returns showed by Platt et. al. (1978).[1,2]

At first, we start with Fraunhofer diffraction based on Kirchhoff's diffraction theory (KD).[8,9] In section 2, the theoretical produces are given. Then we analyze the backscattering pattern by a rectangular target. In section 3, we calculate the scattering by hexagonal columns and plates randomly oriented in horizontal plane and discuss the differences of backscattering between spheres and hexagonal crystals.

2. SCATTERING BY RECTANGULAR PARTICLES

In this section, we calculate the backscattering properties by the rectangular particles with fixed orientation and randomly oriented in horizontal plane (here after 2D-rectangle).

S. Iwasaki.: E-mail: iwasaki@komadori.planet.sci.kobe-u.ac.jp

2.1. Definition of symbols and diffraction pattern

The geometry of the lidar observation is described in Fig. 1. We assume the shape of a receiver is rectangle.
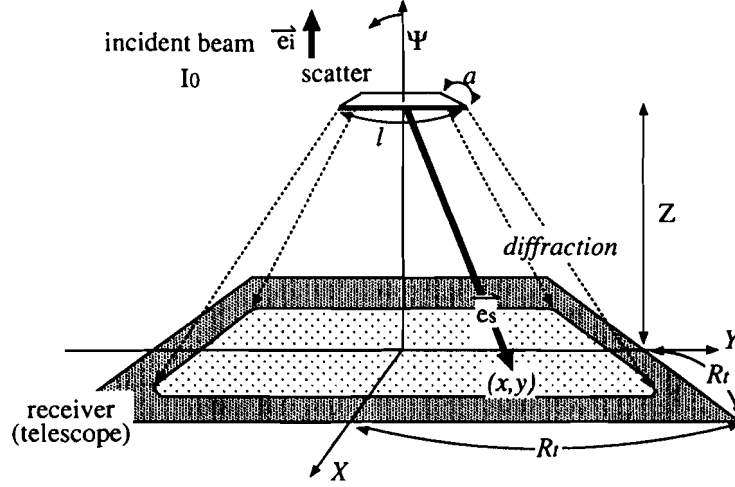
Figure 1. The geometry of the lidar observation. I_0 is the incident light. A particle is located at the altitude Z. Length of the target is specified by a along X axis and l along Y axis ($l \geq a$), respectively. $\vec{e_i}$ and $\vec{e_s}$ denote the incident and scattered directions.

To calculate diffraction pattern by the rectangular particles, we use Kirchhoff's diffraction theory (KD).[8,9] The backscattering irradiance can be written as Eq. 1 in Fraunhofer approximation[5,8] which is derived from KD.

$$I_s(x, y, Z, \Psi) = \frac{G^2}{\lambda^2} \frac{R_{sl} I_0}{Z^2} \left(\frac{\sin \Phi_X}{\Phi_X}\right)^2 \left(\frac{\sin \Phi_Y}{\Phi_Y}\right)^2 e^{-2\tau}$$

$$\Phi_X = kl(x/Z - 2\sin\Psi)/2$$

$$\Phi_Y = kay/2Z \tag{1}$$

where G denotes geometrical cross section of the scatter, R_{sl} is the reflectance of the slab with some thickness and it is calculated by geometrical optics (GO).[13] I_0 is incident intensity. τ is the optical depth. λ and k are wavelength and wave number of interest. l and a ($l \geq a$) are the side length of the rectangle (see Fig. 1). Ψ denotes the angle between the normal vector of the rectangle and the incident beam. The horizontal distribution of backscattered irradiance by a scatter is calculated in Fig. 2 (a).

2.2. Scattering by the rectangular particles with fixed orientation

For a rectangular particle with fixed orientation with $\Psi = 0$, backscattered power into the receiver is formulated by

$$P_r(Z) = C' \int_{-R_t}^{R_t} dx \int_{-R_t}^{R_t} dy I_s(x, y, Z, 0), \tag{2}$$

where R_t is the half width of the receiver and C' is the constant of the lidar instrument, which is also appeared in usual lidar equation (Eq. 5).

2.2.1. Case for very low cloud

When the altitude of cloud is less than 80 m, the size of rectangle is 200 μm × 200 μm, and the receiver is much larger than 0.3 m, most of the backscattered power is received by the receiver (see Fig. 2 (b)) and is estimated by substitution of Eq. 1 into Eq. 2,

$$P_r(Z) = C' R_{sl} I_0 G e^{-2\tau}. \tag{3}$$

It turns out that $P_r(Z)$ does not depend on Z, contrary to the spherical particles where $P_r(Z)$ is proportional to Z^{-2}.
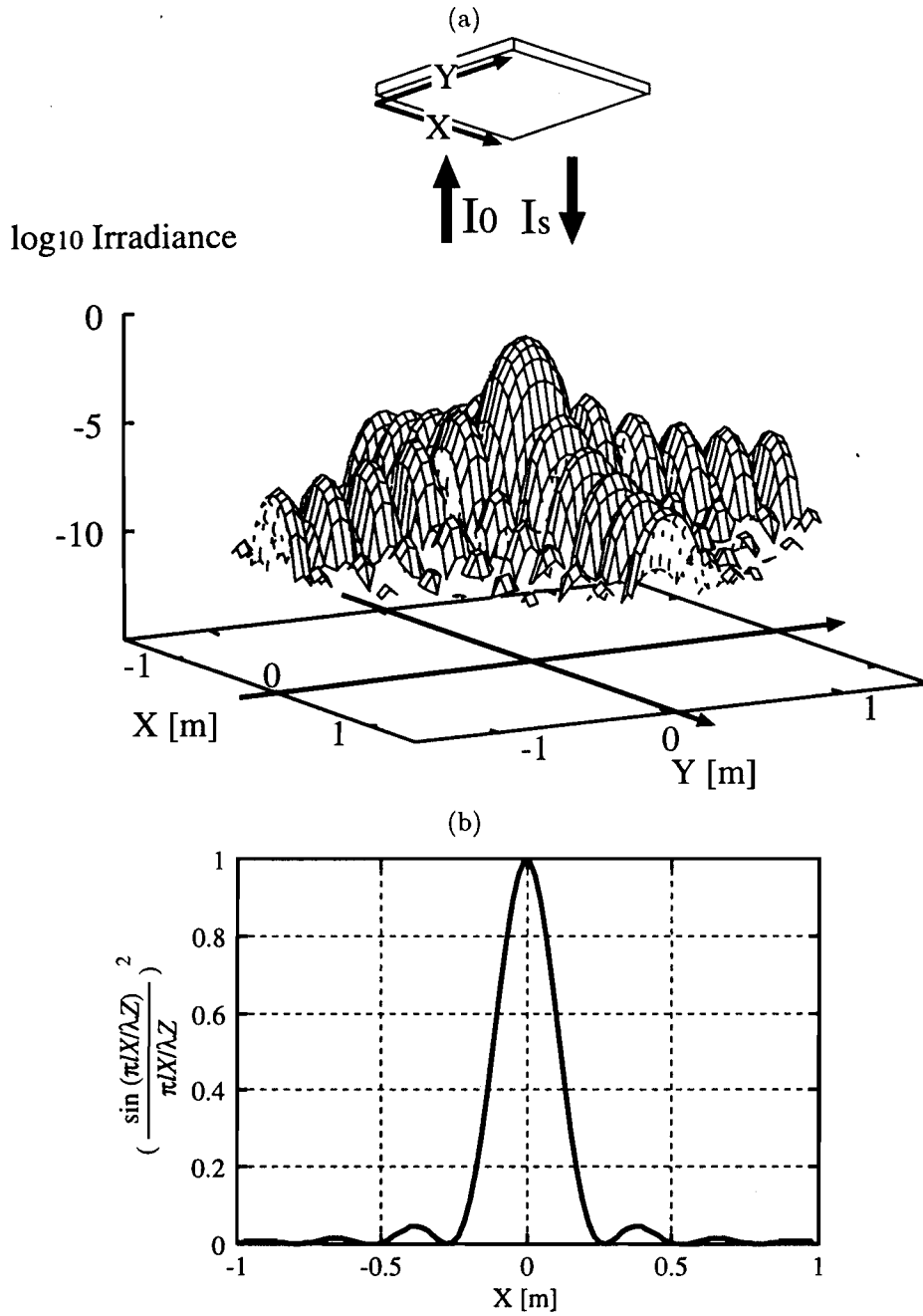
Figure 2. (a) The horizontal distributions of backscattering pattern by the rectangular target normalized at maximum when Ψ is 0, λ is 0.532 μm, l and a are 200 μm and Z is 100 m. (b) Slice of the backscattering profile of (a) at y=0.

2.2.2. Case for high cloud

When altitude is larger than 2 km and other conditions such as sizes of rectangle and receiver are the same as those in previous subsection. Eq. 2 becomes

$$P_r(Z) = C' \frac{4G^2}{\lambda^2} \frac{R_{sl}I_0}{Z^2} R_t^2 e^{-2\tau}. \tag{4}$$

Z-dependence in Eq. 4 is Z^{-2}, which is the same as the usual lidar equation (Eq. 5).

$$P_r(Z) = C\frac{\sigma_{bk}}{Z^2}e^{-2\tau} \tag{5}$$

where C is the constant of the lidar instrument.[3,12] σ_{bk} is the backscattering coefficient.

Z-dependence of this case is the same as that of sphere, however, size dependence G^2 is different from that of sphere (G^1).

2.2.3. Case for intermediate state

This subsection is the case when altitude is $80\ m < Z < 2\ km$ and rest is the same as in subsection **2.2.1**. In this case, it is easily expected that Z-dependence of $P_r(Z)$ has the value between -2 and 0, where the dependence might be changed as the altitude changes.
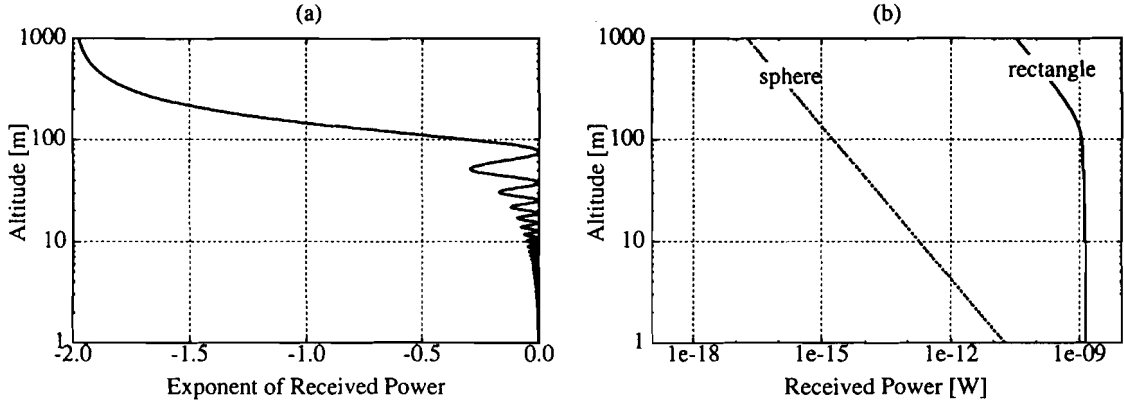
Figure 3. (a) Z-dependence of the exponent of the received power, $dlog_{10}P_r(Z)/dlog_{10}Z$. We assume that shape of a rectangle is 200 $\mu m \times$ 200 μm and R_t is 0.2 m. (b) Z-dependence of the received power scattered by the rectangle and a sphere. Both of them have same geometrical cross section. We neglect the internally reflection of the sphere.

We estimate the relation between Z-dependence of $P_r(Z)$ and Z for a given size of particle and receiver are the same as those in subsection **2.2.1**. Fig. 3 (a) shows Z-dependence of the exponent of the received power, $dlog_{10}P_r(Z)/dlog_{10}Z$. When Z is about 200 m, received power becomes proportional to $Z^{-1.5}$. When altitude is less than 50 m, oscillation occurs, because of the single particle scattering. Fig. 3 (b) shows Z-dependence of the received power scattered by the rectangle and that by a sphere calculated by Eq. 6^{13} where we neglect the internally reflection of the sphere. The rectangle and the sphere have the same geometrical cross sections for the fair comparison.

$$P_{sp}(Z) = \frac{R_{sl}}{4\pi}GI_0\frac{S_t}{Z^2}e^{-2\tau} \tag{6}$$

where S_t is the geometrical cross section of the receiver. At the altitude of 1000 m, received power produces about 2×10^6 times larger signals compared with that of spherical scattering.

2.3. Scattering by the rectangular particles randomly oriented in horizontal plane

For a rectangular target with orientational averagings where major axis of the rectangle is fixed along Y axis and is taken to be parallel to the horizontal plane and minor axis is taken to be along Z axis and rotated around Y axis randomly (2D-rectangle), scattered irradiance can be written as Eq. 7 by using Eq. 1.

$$
\begin{aligned}
I_S(x,y,Z) &= \frac{1}{\pi}\int_0^\pi I_s(x,y,Z,\Psi)d\Psi \\
&= \frac{G^2}{ka\lambda^2}\frac{R_{sl}I_0}{Z^2}(\frac{\sin\Phi_Y}{\Phi_Y})^2e^{-2\tau}
\end{aligned} \tag{7}
$$

Fig. 4 shows the horizontal distribution of backscattering from the target. The shape of the backscattering pattern can be understood from the superposition of that by the rectangular with a fixed orientation.
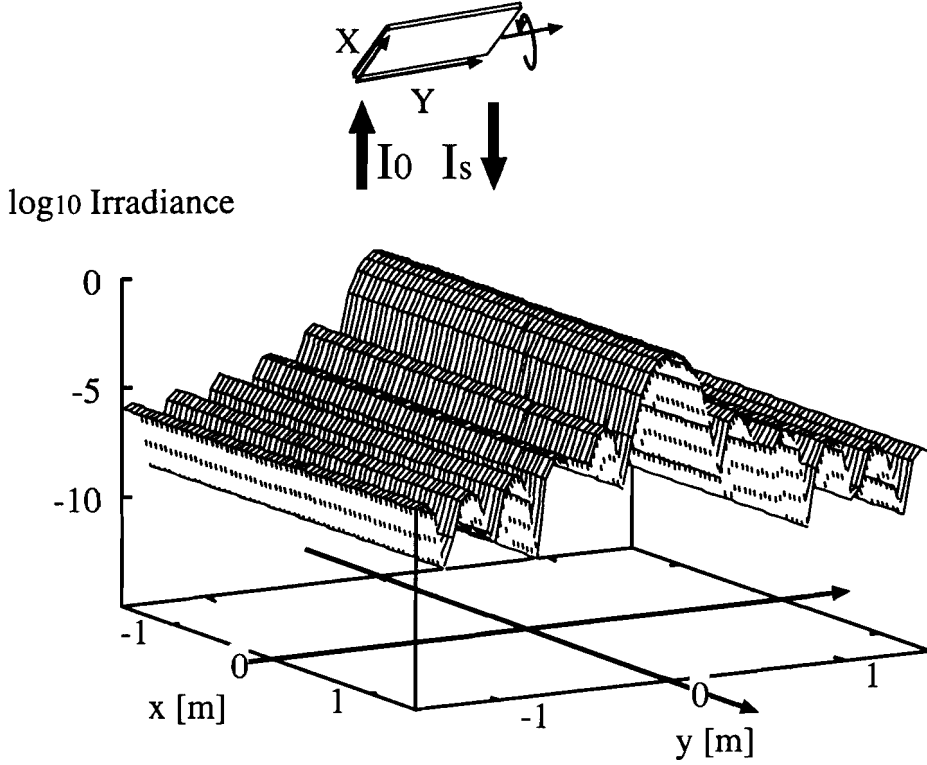
Figure 4. The same as Fig. 2 (a) but for the rectangular target with orientational averaging where major axis of the rectangle is parallel to the Y axis and minor axis is rotated randomly.

Received power becomes

$$P_r(Z) = C' \int_{-R_t}^{R_t} dx \int_{-R_t}^{R_t} dy I_S(x, y, Z)$$ (8)

2.3.1. Case for low cloud

When the altitude of cloud is less than 80 m, and the size of rectangle is 200 $\mu m \times 100$ μm, Eq. 8 becomes

$$P_r(Z) = C' \frac{1}{\pi} \frac{R_t}{Z} R_{sl} I_0 G e^{-2\tau}$$ (9)

This Z^{-1} dependence can be understood by the Z-dependence of cylindrical column[13] to be Z^{-1}.

2.3.2. Case for high cloud

When altitude is larger than 2 km and sizes of rectangle and receiver are the same as those in previous subsection, Eq. 7 becomes

$$P_r(Z) \quad = \quad C' \frac{G^2}{ka\lambda^2} \frac{R_{sl} I_0}{Z^2} R_t^2 e^{-2\tau}$$ (10)

Z-dependence is the same as that in the usual lidar equation (Eq. 5). Contrary to the size-dependence in usual lidar equation ($\propto G$), that dependence in this case becomes G^2/a.

2.3.3. Case for intermediate state

Similar to the case for the fixed orientation, Z-dependence of received power should be changed by its distance like fixed orientational case. Figs. 5 (a) and (b) are the same as Figs. 3 (a) and (b) but for 2D-rectangle whose geometrical cross section is 200 μm × 100 μm. Fig. 5 (a) shows received power is proportional to $Z^{-1.5}$ when Z is about 200 m. When altitude is less than 50 m, oscillation also occurs. Fig. 5 (b) shows received power produces about 10^3 times larger signals compare with that of spherical scattering at the altitude 1000 m.
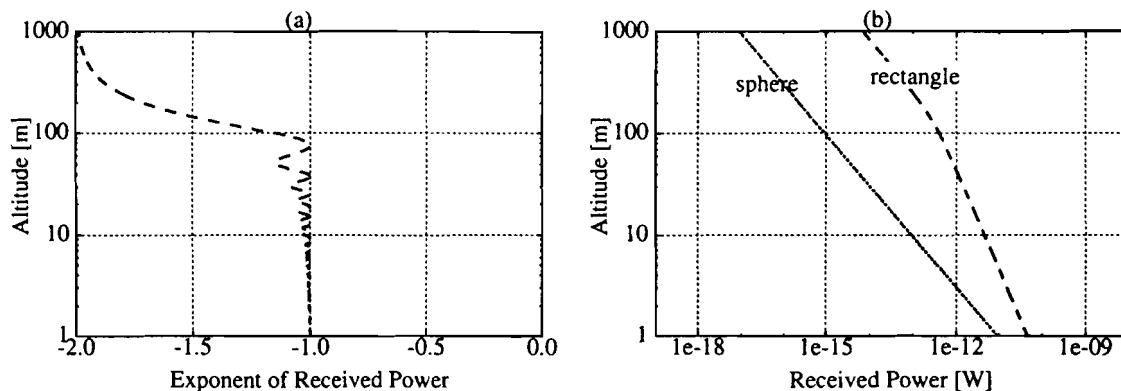

Figure 5. (a) and (b) are the same as Figs. 3 (a) and (b) but for 2D-rectangle whose size is 200 μm × 100 μm.

3. SCATTERING BY HEXAGONAL CRYSTALS

Particle's orientation might depend on its shape. Ono (1969) showed the particle is aligned as its longest axis is parallel to the horizontal plane. For example, when hexagonal column with aspect ratio $asp(\equiv l/2a) = 3$ is considered, symmetrical axis is parallel to the horizontal plane (2D-column). For hexagonal plate with $asp = 1/3$, symmetrical axis is perpendicular to the horizontal plane (2D-plate).
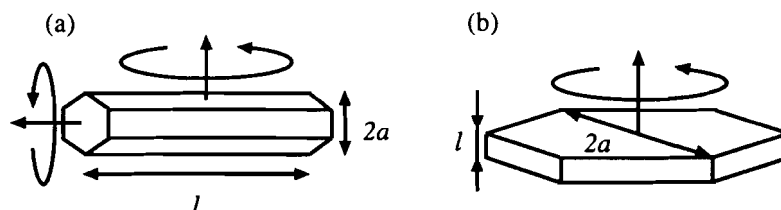

Figure 6. Alignment of a hexagonal crystal. (a) symmetrical axis is parallel to the horizontal plane (2D-column) and (b) symmetrical axis is perpendicular to the horizontal plane (2D-plate).

When the 2D-plate is considered, we assume the backscattered irradiance I_s for 2D-plate is the same as that for a rectangle with fixed orientation which has the same geometrical cross section for 2D-plate. That is, I_s is obtained by using Eq. 1 with $l = a = R_{sq}$, where R_{sq} is the side length of the square. The backscattered irradiance by 2D-column might be 3 times larger than that by 2D-rectangle whose geometrical cross section is the same as that of a rectangle on the hexagonal column.

Figs. 7 (a) and (b) are the same as Figs. 3 (a) and (b) but for 2D-plate and 2D-column. We assume the aspect ratios are 3 and 1/3, $I_0 = 1$ W/m^2, optical constant[10] is $1.31 + i2.54 \times 10^{-9}$, and ice water content (IWC) is 1 g/m^3. And

log-normal distribution (Eq. 11) is assumed, where mode radius r_m is $100\mu m$ and standard deviation σ is 1.5. We neglect the attenuation for the signals ($\tau = 0$). For 2D-plate and 2D-column, $P_r(Z)$ is proportional to $Z^{-1.5}$ when Z is about 500 m. In addition, received power for 2D-plate produces about 10^7 times larger signals compared with that for a sphere with same size distribution at the altitude 1000 m. And that for 2D-column produces about 5×10^3 times larger signals compared with that for a sphere at $Z = 1000$ m.

Figs. 8 (a) and (b) are the same as Figs. 7 (a) and (b) but $r_m = 30$ μm. For 2D-plate and 2D-column, $P_r(Z)$ is proportional to $Z^{-1.5}$ when Z is about 150 m. In addition, received power for 2D-plate produces about 8×10^5 times larger signals compared with that for a sphere at $Z = 1000$ m. And that for 2D-column produces about 10^3 times larger signals compared with that for a sphere at $Z = 1000$ m.

$$\frac{dn(r)}{dr} = \frac{1}{\sqrt{2\pi}r\ln\sigma}exp - \{\frac{\ln r - \ln r_m}{\sqrt{2}\ln\sigma}\}^2 \qquad (11)$$
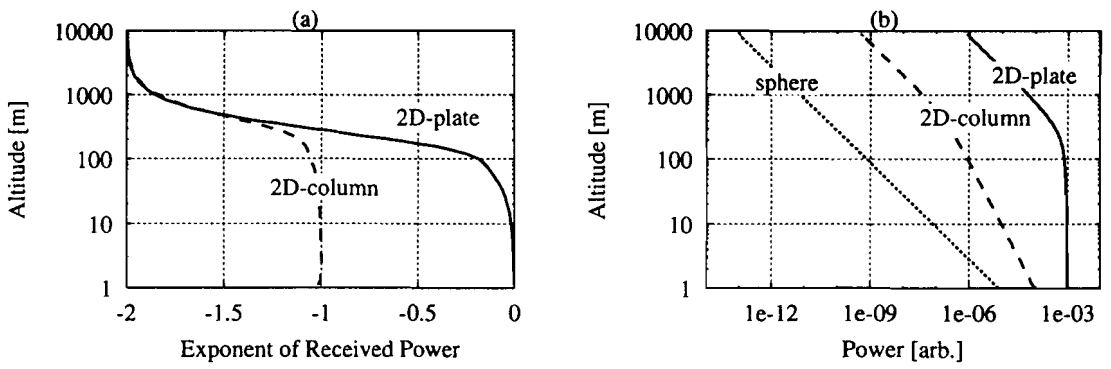
Figure 7. (a) and (b) are the same as Figs. 3 (a) and (b) but for 2D-plate and 2D-column. We assume the aspect ratios are 3 and 1/3 and size distribution is log-normal distribution where mode radius is $100\mu m$ and standard deviation is 1.5.
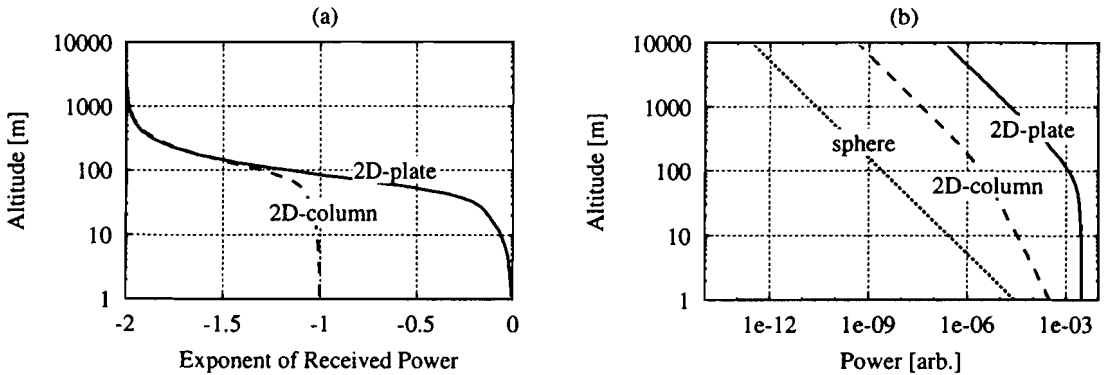
Figure 8. (a) and (b) are the same as Figs. 7 (a) and (b) but $r_m = 30$ μm.

4. SUMMARY

We analyze lidar backscattering enhancement for pristine hexagonal ice crystals by using Fraunhofer diffraction based on Kirchhoff's diffraction theory (KD).

First we start with the backscattering by a rectangular target. Then we compute the scattering by hexagonal ice crystals by using the analogy of the rectangular calculations.

We calculate the scattering by hexagonal column and plate randomly oriented in horizontal plane. We assume that the aspect ratios to be 3 and 1/3 and size distribution is log-normal distribution, where mode radius r_m is 100 μm and standard deviation σ is 1.5. For 2D-plate and 2D-column, $P_r(Z)$ is proportional to $Z^{-1.5}$ when Z is about 500 m. In addition, received power for 2D-plate produces about 10^7 times larger signals compared with that for sphere at the altitude 1000 m. And that for 2D-column produces about 5×10^3 times larger signals compared with that for sphere at $Z = 1000$ m.

For 2D-plate and 2D-column whose $r_m = 30$ μm, $P_r(Z)$ is proportional to $Z^{-1.5}$ when Z is about 150 m. In addition, received power for 2D-plate produces about 8×10^5 times larger signals compared with that for sphere at $Z = 1000$ m. And that for 2D-column produces about 10^3 times larger signals compared with that for sphere at $Z = 1000$ m.

These results are not only important for the scattering by the pristine hexagonal ice crystals, but also applicable for the particles with flat surfaces except for the highly irregular shaped particles, such as Koch fractals.[15]

In this paper, we consider the scattering by the hexagonal crystals perfectly oriented in horizontal plane. However, since it might be rare that the cloud particles stay in such orientation due to turbulence and might have tumbling. This might lead to drastically reduce the backscattering enhancement. The effect of such tumbling is currently investigated by us.

REFERENCES

1. C. M. Platt, "Lidar backscatter from horizontal ice crystal plates," J. Appl. Meteorol. **17**, 482-488 (1978).
2. C. M. Platt, N. L. Abshire, and G. T. McNice, "Some microphysical properties of an ice cloud from lidar observation of horizontally oriented crystals," J. Appl. Meteorol. **17**, 1220-1224 (1978).
3. F. G. Fernald, B. M. Herman, and J. A. Reagan, "Determination of Aerosol Height Distributions by Lidar," J. Appl. Meteor., **11**, 482-489 (1972).
4. J. D. Klett, "Stable analytical inversion solution for processing lidar returns," Appl. Opt. **20**, 211-220 (1981).
5. M. I. Mishchenko, D. J. Wielaard, and B. E. Calson, "T-matrix computations of zenith-enhanced lidar backscatter from horizontally oriented ice plates," Geophys. Res. Lett., **24**, 771-774, (1997).
6. S. Iwasaki, and H. Okamoto, "Anomalous backscattering enhancement by non-spherical ice crystals for lidar observation," Appl. Opt., in submission.
7. K. Sassen, The polarization lidar technique for cloud research: A review and current assessment. Bull. Am. Meteorol. Soc. **72**, 1848-1866 (1991).
8. M. Born and E. Wolf, *Principles of Optics*, (PERGAMON PRESS, Oxford, 1975).
9. Jackson, J.D., *Classical Electrodynamics,* (Wiley, New York., 1983).
10. S. G. Warren, "Optical constants of ice from the ultraviolet to the microwave," Appl. Opt. **23**, 1206-1225 (1984).
11. F. G. Fernald, "Analysis of atmospheric lidar observations: some comments," Appl. Opt. **23**, 652-653 (1984).
12. G. L. Stephanes, *Remote Sensing of the Lower Atmosphere*, (New York, Oxford., 1994), pp. 427-438.
13. C. F. Bohren and D. R. Huffman, *Absorption and Scattering of Light by Small Particles*, (Wiley, New York., 1983)
14. A. Ono, "The Shape and Riming Properties of Ice Crystals in Natural Clouds," J. Atmos. Sci.,**26**, 138-147 (1969).
15. A. Macke, J. Mueller, and E. Raschke, "Single Scattering Properties of Atmospheric Ice Crystals," J. Atmos. Sci., **53**, 2813-2825 (1996).

Analysis of lidar returns from rectangles and hexagonal ice crystals

S. Iwasaki

The Graduate School of Science and Technology, Kobe University
1-1 Rokko-dai, Nada, Kobe, Hyogo 657-8501, Japan

H. Okamoto

Communications Research Laboratory
893-1 Hirai, Kashima, Ibaraki 314-0012, Japan

ABSTRACT

There is a theoretical problem to apply geometrical optics for the backscattering calculations of ice cloud particles. In order to know the backscattering by pristine hexagonal ice crystals, we calculate the scattering for a rectangular particle by using Fraunhofer diffraction based on Kirchhoff's diffraction theory (KD). Then we compute the backscattering by hexagonal plates and columns perfectly oriented in horizontal plane (2D-plate and 2D-column). We show that the received power for the 2D-plates produces $10^4 \sim 10^9$ times larger signals compared with that for spheres with same size distribution at the altitude 10000 m. And that for 2D-columns produces $5 \times 10^2 \sim 3 \times 10^4$ times larger signals compared with that for spheres at $Z = 10000$ m. This might explain the unusual large lidar returns reported by Platt et. al. (1978).

1. INTRODUCTION

Lidar is one of the promising tools to investigate the cloud profiles such as vertical structure, shapes and sizes of ice crystals, which are the unknown factors to correctly estimate the radiative properties of clouds. In order to retrieve above information of size from the lidar observation (e.g. Fernald. 1984), we need to know the backscattering cross section of the cloud particles. It is well known that geometrical optics (GO) is one of the most effective method to calculate the scattering properties by the ice crystals for the lidar wavelength. However, there is a theoretical problem to apply GO for the backscattering calculations of ice cloud particles. We tested GO and it turned out that GO is only applicable for the case the altitude is very close to the ground (e.g. 100 m) and showed the need of modifications to the lidar equation. On the other hands, Mishchenko et. al. (1997) considered disks and spheroids with size parameters up to 50 as ice crystals and calculated lidar backscattering from these particles by using T-matrix method. Since T-matrix method can not apply to the larger size parameters, we develop the method that uses Fraunhofer diffraction based on Kirchhoff's diffraction theory (KD).
In section **2.1** and **2.2**, we calculate the scattering by a rectangular particle for simplicity. In section **2.3** we compute the scattering by hexagonal columns and plates randomly oriented in horizontal plane by using the analogy of the rectangular calculations.
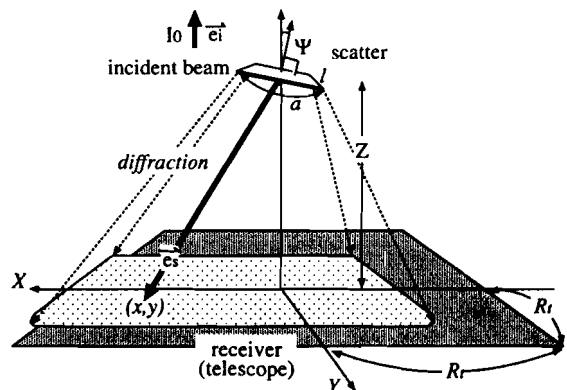
2. SCATTERING MODEL

Figure 1: The geometry of the lidar observation. A particle is located at the altitude Z. Length of the rectangle is specified by l and a ($l \geq a$), respectively. $\vec{e_i}$ and $\vec{e_s}$ denote the incident and scattered directions.

For simplicity, we start with a rectangular particle as the non-spherical particle and we assume the shape of a receiver is also rectangle. To calculate a backscattered pattern, we use Fraunhofer diffraction based on

Kirchhoff's diffraction theory (KD). The backscattering irradiance for a rectangle is written by Eq. 1 where its major axis is parallel to the Y axis and minor axis is fixed in some direction (*e.g.* Born and Wolf 1975).

$$I_s(X, Y, Z, \Psi) = \frac{G^2}{\lambda^2} \frac{R_{sl} I_0}{Z^2} (\frac{\sin \Phi_X}{\Phi_X})^2 (\frac{\sin \Phi_Y}{\Phi_Y})^2 e^{-2\tau}$$

$$\Phi_X = kl(x/Z - 2 \sin \Psi)/2$$

$$\Phi_Y = kay/2Z, \tag{1}$$

where G denotes geometrical cross section of the rectangle, R_{sl} is the reflectance of the slab with some thickness and it is calculated by geometrical optics (GO) (*e.g.* Born and Wolf 1975). I_0 is incident intensity. λ and k are wavelength and wave number of interest. Ψ denotes the angle between the normal vector of the rectangle and the incident beam and τ is the optical depth. l and a ($l \geq a$) are the side lengths of the rectangle (see Fig. 1).

2.1. SCATTERING BY A RECTANGULAR PARTICLE WITH A FIXED ORIENTATION

For a rectangular particle with a fixed orientation at $\Psi = 0$, backscattered power into the receiver is formulated by

$$P_r(Z) = C' \int_{-R_t}^{R_t} dx \int_{-R_t}^{R_t} dy I_s(x, y, Z, \Psi), \tag{2}$$

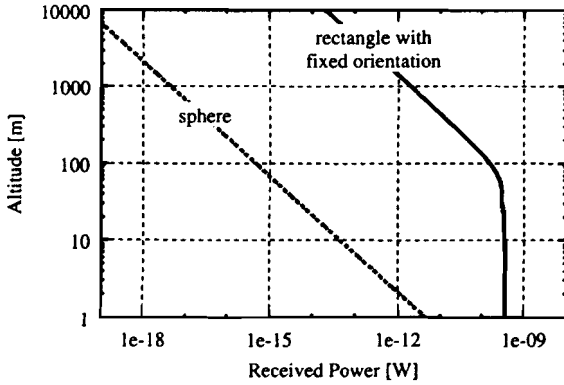where R_t is the half width of receiver and C' is the constant for the lidar instruments.

Figure 2: Z-dependence of the received power scattered by the rectangle and a sphere. We neglect the internally reflection of the sphere. The rectangle and the sphere have same geometrical cross sections.

Fig. 2 shows Z-dependence of $P_r(Z)$ for a rectangle with a fixed orientation and that for a sphere where

we neglect the internally reflection of the sphere. The rectangle and the sphere have the same geometrical cross sections for the fair comparison. We assume that the shape of a rectangle is 100 μm × 100 μm, $R_t = 0.2\ m$, $\lambda = 0.532\ \mu m$, $I_0 = 1\ W/m^2$, $C' = 1$ and optical constant is $1.31 + i2.54 \times 10^{-9}$. And we neglect the attenuation for the signals ($\tau = 0$). At the altitude of $1000\ m$, received power produces about 5×10^5 times larger signals compared with that for the sphere.
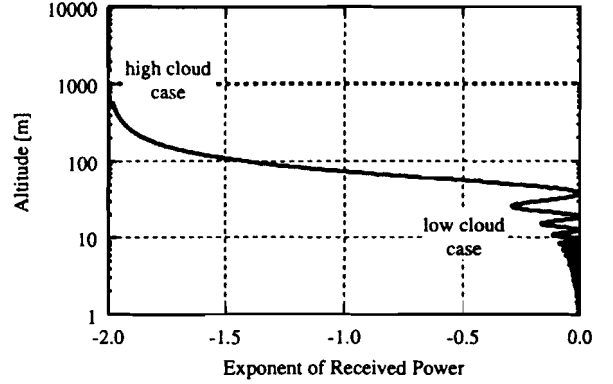

Figure 3: Z-dependence of the exponent of the received power, $d log_{10} P_r(Z)/d log_{10} Z$.

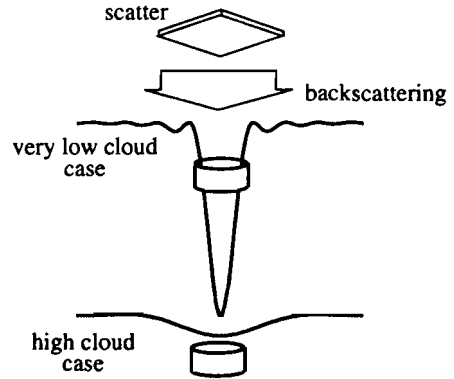Fig. 3 shows Z-dependence of the exponent of the received power, $d log_{10} P(Z)/d log_{10} Z$.

Figure 4: The sketch of the relation between backscattering irradiance, receiver and altitude.

When Z is small, most backscattered power is received (see Fig. 4). Its received power is derived by substitution of Eq. 1 into Eq. 2,

$$P_r(Z) = C' R_{sl} I_0 G. \tag{3}$$

It turns out that $P_r(Z)$ does not depend on Z, contrary to the dependence Z^{-2} in the usual lidar equa-

tion (Eq. 4).

$$P_r(Z) = C \frac{\sigma_{bk}}{Z^2} e^{-2\tau}, \qquad (4)$$

where C is the constant of the lidar system (Fernald. 1984). σ_{bk} is the backscattering coefficient.
When Z is large, received power is derived by

$$P_r(Z) = C' \frac{G^2}{\lambda^2} \frac{S_t}{Z^2} R_{sl} I_0 e^{-2\tau}, \qquad (5)$$

where S_t is the area of the receiver, $(2R_t)^2$. It turns out that Z-dependence is as same as that in the usual lidar equation, however, size dependence G^2 appeared in Eq. 5 is different from G in the usual lidar equation. The exponent drastically changes from 0 at $Z = 50\ m$ to -2 at $Z = 500\ m$.

2.2. SCATTERING BY A RECTANGLE RANDOMLY ORIENTED IN HORIZONTAL PLANE

For a rectangular target randomly oriented in horizontal plane (2D-rectangle), the backscattered irradiance becomes

$$
\begin{aligned}
I_S(x, y, Z) &= \frac{1}{\pi} \int_0^\pi I_s(x, y, Z, \Psi) d\Psi \\
&= \frac{G^2}{ka\lambda^2} \frac{R_{sl} I_0}{Z^2} \left(\frac{\sin \Phi_Y}{\Phi_Y}\right)^2 e^{-2\tau}. \quad (6)
\end{aligned}
$$

For a 2D-rectangle, received power is formulated by

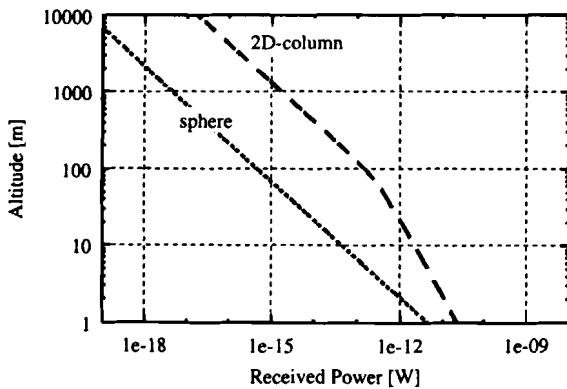$$P_r(Z) = C' \int_{-R_t}^{R_t} dx \int_{-R_t}^{R_t} dy I_S(x, y, Z). \qquad (7)$$

Figure 5: The same as Fig. 2 but for 2D-rectangle whose geometrical cross section is 100 μm × 100 μm.

Here 2D-rectangle with geometrical cross section of 100 μm × 100 μm is considered. Fig. 5 is the same as Fig. 2 but for 2D-rectangle. Fig. 5 shows received power produces about 2×10^2 times larger signals compare with that of spherical scattering at the altitude 1000 m.
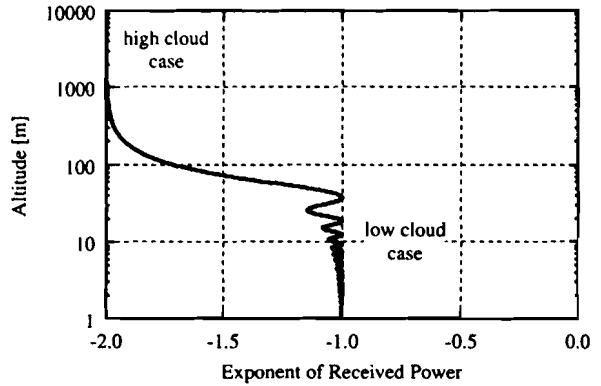

Figure 6: The same as Fig. 3 but for 2D-rectangle whose geometrical cross section is 100 μm × 100 μm.

Similar to the case for the fixed orientation, Z-dependence of received power should be changed by its distance. $P_r(Z)$ is proportional to $Z^{-1.5}$ when Z is about 80 m.
When Z is small, received power is derived by substitution of Eq. 6 into Eq. 7,

$$P_r(Z) = C' \frac{1}{\pi} \frac{R_t}{Z} R_{sl} I_0 G. \qquad (8)$$

This can be understood that $P_r(Z)$ is proportional to Z^{-1}, contrary to the spherical particles. In these region, GO is applicable and the dependence is Z^{-1} as Eq. 8.
When Z is large, Z-dependence for this case becomes Z^{-2}, which is the same dependence for the sphere. This can be understood by the following explanation. The distance between the particle and the receiver is large enough so that the horizontal distribution of the backscattered power is homogeneous over the receiver, which is the same as that for the scattering wave by the sphere.

2.3. DISTANCE DEPENDENCE OF THE RECEIVED POWER BY HEXAGONAL CRYSTALS

When the hexagonal plate with an aspect ratio of 1/3 randomly oriented in horizontal plane (2D-plate) is considered, we assume its backscattered irradiance

I_s is the same as that for the square with a fixed orientation which has the same geometrical cross section of 2D-plate.

When the hexagonal column with an aspect ratio of 3 randomly oriented in horizontal plane (2D-column) is considered, we assume its backscattered irradiance I_s is given by the superposition of the backscattered wave from every surface where the backscattering signals from a surface of hexagonal column is estimated by the similar procedure described in section **2.2**.

We assume that ice water content (IWC) is 1 g/m^3, and size distribution is log-normal distribution where mode radiuses r_m are 10, 100, 1000 μm and standard deviation σ is 1.5.

Fig. 7 (a) shows that received power for 2D-plate produces $10^4 \sim 10^9$ times larger signals compared with that for spheres with same size distribution at the altitude 10000 m. And that for 2D-column produces $5 \times 10^2 \sim 3 \times 10^4$ times larger signals compared with that for spheres at $Z = 10000\ m$. Fig. 7(b) is the same as Fig. 3 but for 2D-plate and 2D-column.
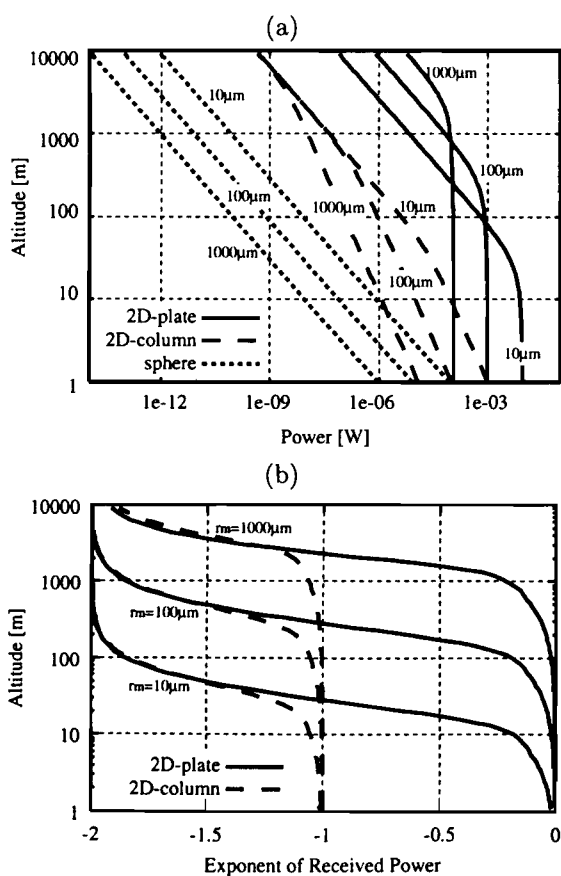
4. SUMMARY

We analyze lidar backscattering enhancement for pristine hexagonal ice crystals by using Fraunhofer diffraction based on Kirchhoff's diffraction theory (KD).
At first, we calculate the scattering by a rectangular particle for simplicity. Then we compute the scattering by hexagonal columns and plates randomly oriented in horizontal plane (2D-plate and 2D-column) by using the analogy of the rectangular calculations.
It turns out that the received power for 2D-plate produces $10^4 \sim 10^9$ times larger signals compared with that for spheres with same size distribution at the altitude 10000 m. And that for 2D-column produces $5 \times 10^2 \sim 3 \times 10^4$ times larger signals compared with that for a sphere at $Z = 10000\ m$.
Our theoretical calculations show the existence of the hexagonal particles randomly oriented in horizontal plane might be explained for the unusual large lidar returns reported by Platt et. al. (1978).
In this paper, we consider the scattering by the hexagonal crystals perfectly oriented in horizontal plane. However, since it might be rare that the cloud particles stay in such orientation due to turbulence and might have tumbling. This might lead to drastically reduce the backscattering enhancement. The effect of such tumbling is currently investigated by us.

ACKNOWLEDGMENTS

Figure 7: (a) and (b) are the same as Fig. 2 and Fig. 3 but for 2D-plate and 2D-column.

References

Platt, C. M., N. L. Abshire, and G. T. McNice, 1978: Some microphysical properties of an ice cloud from lidar observation of horizontally oriented crystals, J. Appl. Meteorol. **17**, 1220-1224.

Fernald, F. G., 1984: Analysis of atmospheric lidar observations: some comments, Appl. Opt., **23**, 652-653.

Iwasaki, S., and H. Okamoto, submitted: Anomalous backscattering enhancement by non-spherical ice crystals for lidar observation, Appl. Opt.

Mishchenko, M. I., D. J. Wielaard, and B. E. Calson, 1997: T-matrix computations of zenith-enhanced lidar backscatter from horizontally oriented ice plates, Geophys. Res. Lett., **24**, 771-774.

Born, M. and E. Wolf, 1975: *Principles of Optics*, PERGAMON PRESS, Oxford.